Modelling and Validation of Agricultural Tire-Terrain Interaction

By

Mirwais Sharifi

A Thesis Submitted to the

School of Graduate and Postdoctoral Studies Partial Fulfillment of the

Requirements for the Degree of

Master of Applied Science

In

Mechanical Engineering

Faculty of Engineering and Applied Science

University of Ontario Institute of Technology (Ontario Tech University)

Oshawa, Ontario, Canada

December 2020

THESIS EXAMINATION INFORMATION

Submitted by: **Mirwais Sharifi**

Master of Applied Science in **Mechanical Engineering**

Thesis title: Modelling and Validation of Agricultural Tire-Terrain Interaction

An oral defense of this thesis took place on <December 02, 2020> in front of the following examining committee:

Examining Committee:

Chair of Examining Committee	Dr. Haoxiang Lang
Research Supervisor	Dr. Moustafa El-Gindy
Examining Committee Member	Dr. Xianke Lin
Thesis Examiner	Dr. Walid Morsi Ibrahim, Ontario Tech University

The above committee determined that the thesis is acceptable in form and content and that a satisfactory knowledge of the field covered by the thesis was demonstrated by the candidate during an oral examination. A signed copy of the Certificate of Approval is available from the School of Graduate and Postdoctoral Studies.

ABSTRACT

The use of Finite Element Analysis (FEA) and simulation software has been extensively used for many engineering applications. More precisely, computerized methods have paved way for accurately simulating tire-terrain interaction. By predicting forces, vibrations, and numerous physical effects, any industry with pneumatic tires can greatly reduce time, cost and effectively design and improve their machinery. The modelling and validation of a High Lug Farm Service (HLFS) agricultural tire is carried out in order to accurately predict tire-terrain interaction. In conjunction with the tire, two agricultural soils are modelled using Smoothed-Particle Hydrodynamics (SPH) method and calibrated to experimental results. An analytical off-road rigid ring model is used to model the HLFS tire's interaction with a surface. The soil dynamics of the HLFS tire running on soil is researched and compared to experimental results. Steering characteristics including self-aligning moment, rolling resistance coefficients, relaxation lengths were obtained under various operating conditions.

Keywords: Tire-terrain interaction; Finite Element Analysis; Smoothed-particle Hydrodynamics; RRC; rigid ring parameters

AUTHOR'S DECLARATION

I hereby declare that this thesis consists of original work of which I have authored. This is a true copy of the thesis, including any required final revisions, as accepted by my examiners.

I authorize the University of Ontario Institute of Technology (Ontario Tech University) to lend this thesis to other institutions or individuals for the purpose of scholarly research. I further authorize University of Ontario Institute of Technology (Ontario Tech University) to reproduce this thesis by photocopying or by other means, in total or in part, at the request of other institutions or individuals for the purpose of scholarly research. I understand that my thesis will be made electronically available to the public.

Mirwais Sharifi

Mirwais Sharifi

STATEMENT OF CONTRIBUTIONS

Part of the work described in Chapter 2 has been published as:

Sharifi, M., El-Sayegh, Z., and El-Gindy, M., "Sensitivity Analysis of Tire-Soil Interaction Using Finite Element Analysis and Smoothed-Particle Hydrodynamics Techniques," SAE Technical Paper 2019-01-0174, 2019

Part of the work described in Chapter 3 has been published as:

El-Sayegh, Z., Sharifi, M., Gheshlaghi, F. *et al.* Development of an HLFS agricultural tire model using FEA technique. *SN Appl. Sci.* **1,** 1454 (2019)

Part of the work described in Chapter 4 has been published as:

Sharifi, M., El-Sayegh, Z., and El-Gindy, M., "Sensitivity Analysis of Tire-Soil Interaction Using Finite Element Analysis and Smoothed-Particle Hydrodynamics Techniques," SAE Technical Paper 2019-01-0174, 2019

Part of the work described in Chapter 6 has been published as:

Sharifi, M., El-Sayegh, Z., and El-Gindy, M., "Sensitivity Analysis of Tire-Soil Interaction Using Finite Element Analysis and Smoothed-Particle Hydrodynamics Techniques," SAE Technical Paper 2019-01-0174, 2019

El-Sayegh, Z., Sharifi, M., Gheshlaghi, F. *et al.* Development of an HLFS agricultural tire model using FEA technique. *SN Appl. Sci.* **1,** 1454 (2019)

ACKNOWLEDGEMENTS

First of all, I would like to show my utmost gratitude to my supervisor, Professor Moustafa El-Gindy and Zeinab El-Sayegh for their support and motivation throughout my research and MASc. studies at Ontario Tech University. Their continuous advice, support and motivation have been invaluable throughout the two years I have been at Ontario Tech University.

I would also like to express my appreciation to NSERC Discovery Grant for their funding of this research work and allowing me to contribute to the state of the art research for tire terrain interaction. I would also like to thank Fatemeh Gheshlagi for providing the experimental data that were used to validate some of the research results.

I would like to acknowledge my friends and family. Especially my wife, Lema, for her extensive support and motivation throughout not only in my academic journey but in life we share together. I want to express my sincere appreciation to my family; especially my mother and brother for their continuous and unlimited support in my academic endeavours.

Table of Contents

LIST OF FIGURES

LIST OF TABLES

NOMENCLATURE

In-Plane Rigid-Ring Parameters

a_{soil}	Effective Contact Patch for Clayey Loam	m
c_{bz}	Vertical Damping Constant	kN-s/m
c_{tot}	Tire Damping Constant	kN-s/m
c_{vr}	Residual Damping Constant	kN-s/m
$c_{b\theta}$	Rotational Damping Constant	kN-m-s/rad
k_{bz}	Sidewall Stiffness	kN/m
$k_{b\theta}$	Rotational Stiffness	kN-m/rad
$k_{cx,soil}$	Longitudinal Tread Stiffness for Clayey Loam	kN/m
$k_{k,soil}$	Longitudinal Tire Stiffness for Clayey Loam	kN/unit slip
$k_{k,soil/v_{tr}}$	Longitudinal Tread Damping for Clayey Loam	kNs/m
k_{soil}	Soil Stiffness	kN/m
k_{tot}	Total Vertical Stiffness	kN/m
$k_{tot,soil}$	Total Vertical Stiffness of soil	kN/m
k_{vr}	Residual Vertical Stiffness	kN/m
$R_{r,soil}$	Effective rolling radius with soil	m

Out-of-Plane Rigid-Ring Parameters

c_{bz}	Translational Damping Constant	kN-s/m
c_{l}	Lateral Damping Constant	kN-s/m
$c_{l,soil}$	Lateral Damping Constant, Clayey Loam	kN-s/m
$c_{b\gamma}$	Rotational Damping Constant	kN-s/rad
k_{by}	Translational Stiffness	kN/m
$k_{b\gamma}$	Translational Stiffness	kN-m/rad
$k_{f,soil}$	Cornering Stiffness for Clayey Loam	kN/rad
k_{l}	Lateral Tire Stiffness	kN/m
$k_{l,tot,soil}$	Total Lateral Slip Stiffness of Clayey Loam	kN/m
$k_{l,soil}$	Lateral Slip Stiffness of soil	kN/m
$k_{M,soil}$	Self-Aligning Torque Stiffness of soil	kN-m/rad
RRC_{soil}	Rolling Resistance Coefficient in Clayey Loam	-
σ_{soil}	Relaxation Length	m

Additional Parameters

b	Loading plate radius	m
C_1	Bulk Modulus (of soil)	-
C_{10}	First Mooney-Rivlin Coefficient	-
C_{01}	Second Mooney-Rivlin Coefficient	-
c	Cohesion of soil	kPa
c_c	Critical damping constant	kN-m-s/rad
f	First nodal frequency	Hz
F_x	Longitudinal Force	kN
F_y	Lateral Force	kN
F_z	Vertical Force	kN
j	Shear displacement	mm
I_{bx}	Tire belt moment of inertia	kg-m^2
I_{by}	Tire belt moment of inertia	kg-m^2
k_c	Cohesive modulus of terrain deformation	kN/m
k_θ	Frictional modulus of terrain deformation	kN/m
m_a	Mass of rim	kg
m_b	Mass of tire belt	kg
m_{tot}	Total mass of tire model	kg
m_{wheel}	Mass of tire and rim	kg
M_x	Overturning moment	Nm
M_y	Rolling resistance moment	Nm
M_z	Self-Aligning moment	Nm
n	Exponent of terrain deformation	-
p	Pressure	MPa
p	Applied loading on plate	kPa
t_1	Time of first peak of logarithmic decay	s
t_2	Time of second peak logarithmic decay	s
v_{tr}	Tire velocity	m/s
V_x	Velocity	km/h
y_1	First peak of translational displacement	m
y_2	Second peak of translational displacement	m
$y_{l,1}$	First peak of translational displacement	m
$y_{l,2}$	Second peak of translational displacement	m
$y_{l,ss}$	Steady state translational displacement	m
y_{ss}	Steady state translational displacement	m
z	Sinkage of soil	m
α	Proportional sidewall nodal damping factor	rad/s
δ	Logarithmic decrement	-
θ	Angle of internal shearing resistance	deg
θ_{ss}	Steady state angular displacement	rad
θ_1	First peak angular displacement	rad
θ_2	Second peak angular displacement	rad
μ	$\mu = \left(\frac{\rho}{\rho_0}\right) - 1$	-
ξ	Critical damping ratio	-

Additional Parameters

ξ_{tot}	Total damping ratio	-
τ_{max}	Max shear strength	kPa
τ_d	Damped period of vibration	s
ρ_o	Internal material density	kg/m^3
ρ	Material density	kg/m^3
τ_{max}	Maximum shear strength of soil	MPa
γ	Camber angle	deg
Φ	Angle of internal shearing resistance	deg
ω	Natural frequency of vibration	rad/s
ω_n	Undamped natural frequency	rad/s
ω_d	Damped natural frequency	rad/s
W	Work	J
z	Plate sinkage	m

CHAPTER 1 – INTRODUCTION

This chapter includes the motivation, problem statement and objectives of the research done on tire-terrain interaction.

1.1 Motivation

The use of simulation software for tire-ground interaction is beneficial for the agricultural industry as industries can predict the forces and dynamics of a vehicle. The agricultural tire's interaction with the ground significantly impact the energy savings, soil conservation and vehicle performance. It is important to study agricultural tires in terms of supporting the vehicle it maneuvers, absorbing shock loads and dampen the surface irregularities, provide traction and braking, providing steering and directional stability. The vehicle's performance heavily relies on the forces at the tire-terrain interface. Modelling and validating the tire in terms of its in-plane and out-of-plane parameters allows for the study of the interaction of the tire with the soil and can be used as research for the full vehicle performance. The tire's rolling resistance defines the vehicle's traction, energy consumption, tread wear, soil stress and stability during operation. The agricultural industry makes extensive use of tires in their vehicles and the tire's physical properties will enable further research to be done on tire-terrain interaction.

1.2 Problem Statement

In order to understand the tire characteristics of a pneumatic tire, an FEA tire model may be used to see its response using several operating conditions. The modelling and validation of the tire ensures that its static and dynamic simulations are in good agreement to physical experimental results. These tire models may be used in full vehicle models to fully understand the dynamics of agricultural vehicles. There are many tire models which may be used for these FEA simulations, each holding their advantages. The rigid ring model is one way of simplifying a pneumatic tire in terms of springs and dampers in order to get the tire's characteristics. Similarly, the modelling of the terrain is crucial in order to facilitate the simulations using the same terrain and conditions as physical experiments. Using both the tire and soil models in conjunction will validate the tire's static and dynamic behaviour. Once validated, the tire's dynamics on rigid surfaces and varying terrain under different operating conditions may be accurately predicted. The use of Finite Element Method is used to predict these rigid ring parameters in varying terrain. The simulations will be conducted in ESI's Visual Environment PAM-Crash application.

1.3 Objectives and Scope

This thesis' scope is to initially model and validate the High Lug Farm Service (HLFS) tire used for agricultural tractors in a static and dynamic analysis. The tire properties are adjusted for which the results are to be as close as possible to physical measurements conducted in Urmia University in Iran [1]. The simulation of standards tests such as the vertical, lateral and longitudinal stiffness are conducted. These simulations are compared to experimental data from Urmia University [1]. A Clayey Loam and LETE sand terrain will also be modelled using the Smoothed-Particle Hydrodynamics technique within PAM-Crash. The prediction of the off-road rigid ring parameters and tire characteristics are to be conducted in both in-plane and out-of-plane analysis on a clayey loam soil at different operating conditions. These conditions include: three vertical loads of 13.34 kN (3000 lbs), 26.62 kN (5985 lbs) and 40 kN (9000 lbs); at three inflation pressures of 103 kPa (15 psi), 193 kPa (28 psi) and 275 kPa (40 psi). These loads are chosen by basis of under-loaded, optimal load and overloaded; and under-inflated, operating inflation pressure, and overinflated. The trend of the rigid ring parameters and tire characteristics as a function of the varying operating conditions will be studied. These operating conditions have been used in several studies including tire-terrain interaction [2]. In addition, the soil dynamics for a tire running over soil at different vertical loads and inflation pressures are conducted in order to find the stress distribution within the soil. These tests are conducted for different tire velocities, soil depths and Clayey Loam and LETE sand terrains.

1.5 Thesis Outline

This thesis will be presented in 6 chapters which are as follows.

Chapter 1: The motivation, problem statement, scope and objectives of the research work done with some background on the pneumatic tire is delivered.

Chapter 2: This chapter covers the previous research found on tire and soil modelled from an analytical and FEA perspective. It also covers the literature studied on soil stress analysis, static and dynamic tire-terrain interaction and their characteristics.

Chapter 3: This chapter covers the modelled and validated High Lug Farm Service tire using Pam-Crash simulation software. A 220/70B16 agricultural tire is modelled using FEM and validated against experimental data using simulation software.

Chapter 4: This chapter contains details related to the modelled and calibrated soil and sand terrain using terramechanics data. The two terrains were calibrated using a pressure sinkage test and shear test using SPH particles. The pressure sinkage and shear box test yield the plate displacement in soil, cohesion and angle of internal shearing resistance. Soil material parameters are calibrated to adhere to similar plate displacement, cohesion and angle of internal shearing resistance as found in literature.

Chapter 5: The study of soil dynamics is presented in this chapter. The HLFS tire's stress distribution within four depths of soil is obtained by applying a vertical load of 2 kN (450lbs) and inflation pressure of 344.74 kPa (50 psi). The effect of varying tire velocity on stress distribution is analyzed.

Chapter 6: The in-plane and out-of-plane rigid ring tire model parameters, the first vertical and longitudinal modes of vibration are determined in within this chapter. The in-plane parameters include total vertical stiffness, sidewall vertical stiffness, residual vertical stiffness. The total vertical damping and sidewall vertical damping constant and residual damping constant are also obtained. The rotational tire stiffness and damping constant are predicted. Next the total equivalent vertical stiffness in soil was found. Lastly, the longitudinal tire stiffness and longitudinal tread stiffness along with longitudinal tread damping was obtained. The out-of-plane parameters include the translational stiffness and damping constant; rotational stiffness and damping constant and lateral stiffness and damping constant on rigid surface and soil.

Chapter 7: The conclusions, results and contributions of this research study are summarized in this chapter. Future research recommendations along with the list of publications are also included.

CHAPTER 2 - LITERATURE REVIEW

2.1 Chapter Introduction

This chapter contains the prior research and background on tires and terrains using several techniques. Studies in regards to analytical and FEA models for both tire and soil are discussed. The advantage sand disadvantages of these models are clarified. The soil dynamics for a tire rolling on terrain is also reviewed.

2.1.1 Pneumatic Tires

The idea of using a pneumatic tire for transporting loads was first invented by Robert William Thompson and later developed by Dunlop and Michelin [3]. In 1845, Thompson used a leather tire enclosing a rubberized fabric tube which was filled with air. These “aerial” wheels ran for a long distance but was forgotten for a long time due to the expensive manufacturing of rubber. As the bicycle became more popular, in the year 1888, John Boyd Dunlop patented the pneumatic tire for bicycles and other vehicles. A few years later, the Michelin brothers started to use pneumatic tires on motored vehicles and sparked great interest in the 1895 Paris-Bordeaux road race [3]. In 1948, Michelin was the first company to introduce steel-belted radial tires. Ever since, almost all of the motor vehicles make use of the pneumatic tire. As a result, the study of pneumatic tires in physical experiments and computer software has shown great advance and is a huge industry. The finite element analysis of pneumatic tires has also shown great accuracy and cost efficient methodology.

2.2.2 Construction of HLFS

The construction of a pneumatic tire has to meet several important criteria. The have to have low rolling resistance, low vertical stiffness (for ride comfort), large sliding friction in wet and dry terrain, high longitudinal and lateral stiffness (in order to minimize sliding motions in the contact patch) and resistance to wear and damage.

A pneumatic tire is usually restrained on the wheel using beads that are molded into the tire edges. The tire edges are channelled onto the rim's circumference and held firmly against the edge by the inflation pressure within the tire. This pressure is carried by layers of cords which are within the rubber which contains the air and provides high friction with the ground. The carcass ply consists of all these belts and cords and provide the different tire characteristics. The tire makes use of the tread for traction and sidewall for cushioning and retaining the vertical load. Three different pneumatic tires can be seen in Figure 2-1.

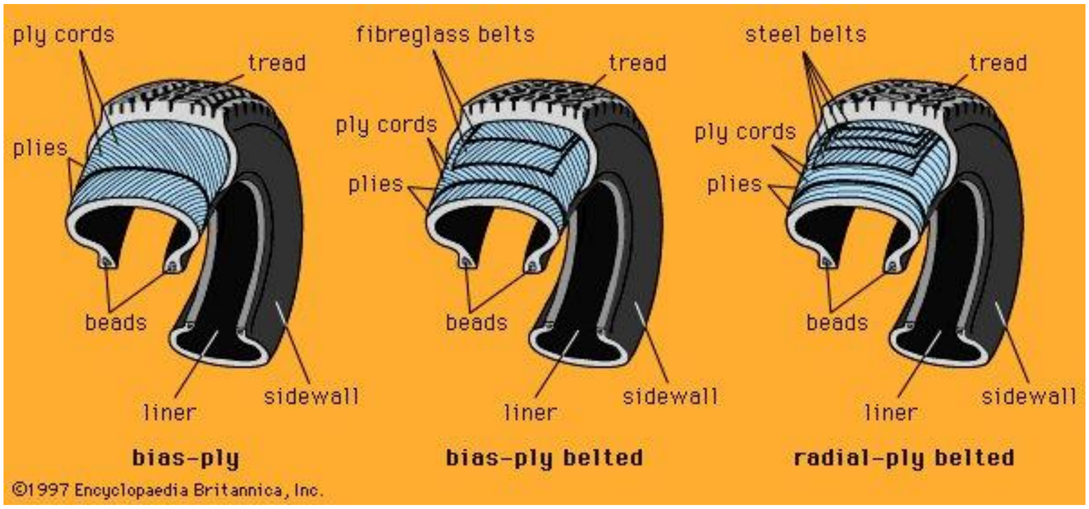

Figure 2-1 Bias-ply belted and radial-ply belted pneumatic tires [3].

The ply or the way which the layers of cords in the carcass are constructed is perhaps the most important part of the tire. The crown angle is the angle of the cord's alignment with the longitudinal axis. In a bias-ply tire the crown angle are higher than 25 degrees, roughly around 50 degrees and arranged in successive plies across one another. In a bias-ply belted tire, an extra set of cord overlies the bias-laid ones. This belt is usually constructed from fiberglass. In a radial structure, the crown angle is less than 25 and sometimes lie almost perpendicular to the axis of the tire tube. This maximizes the tension across the width of the tire and gives a greater resistance in the lateral direction and therefore provides better cornering characteristics. In terms of ride comfort, the bias-ply and bias-ply belted provide better cushioning effect. Due to having good cornering, small distortion of the tread, low wear and lower rolling resistance, many passenger cars make use of the radial-ply tire. The agricultural industry deals with severe irregular surfaces and therefore bias-ply tires are used for ride comfort. In this study an agricultural tire of size 220/70B16 is researched.

2.2 Tire Modelling

This section covers the background and research conducted in regards to analytical, empirical, and FEA tire models.

2.2.1 Analytical and Empirical Tire Modelling

Several analytical tire models tire and its dynamics using a set of masses springs and dampers. These parameters may be used in equations of motion in order to understand the dynamics of the tire and vehicle.

When analyzing the tire-ground interaction, if the surface irregularities are not important and the tire is running at a constant velocity, the point contact model may be used for vehicle vibration dynamics under steady-state conditions. If the irregularities are great, then the point contact model cannot represent the contact relationship between the tire and the ground.

Captain et al, in 1979, and Loo in 1985 make use of the one point model where the contact region between the tire and the ground is a point that is a projection of the center of the tire onto the ground [4, 5]. This simple model resulted in a very sensitive tire response due to the single point deflections being high in road irregularities had short periods or wavelengths. It is optimal to use this model for surfaces which have long wavelength road irregularities. The point contact model may be seen in Figure 2-2. This model may be used with two conditions. The tire stiffness is considered as a concentrated stiffness coefficient and is constant in terms of varying the vertical dynamic load of the tire. It does not manifest nonlinear characteristics of tires with large deformations undergoing non steady maneuvers such as rapid accelerating or braking [6]. As stated earlier, the calculation of the vertical force due to surface irregularities will have a large error for very irregular surfaces. This is due to the error between the vertical deformation calculated and the practical tire deformation due to severe surface irregularities.

The fixed contact patch model of tires is based on converting the equivalent concentrated stiffness of the tires into a number of equivalent distributed stiffness within a fixed length of the contact patch [6]. In comparison to the single point contact model, the fixed contact patch model inhibits the comprehensive effect of the force from the surface irregularities within the contact patch. This gives a dynamic force which is more accurate compared to the practical value. Once again, the equivalent stiffness is a constant value and is not optimal for analysis of the vehicle under large deformations in the contact patch.

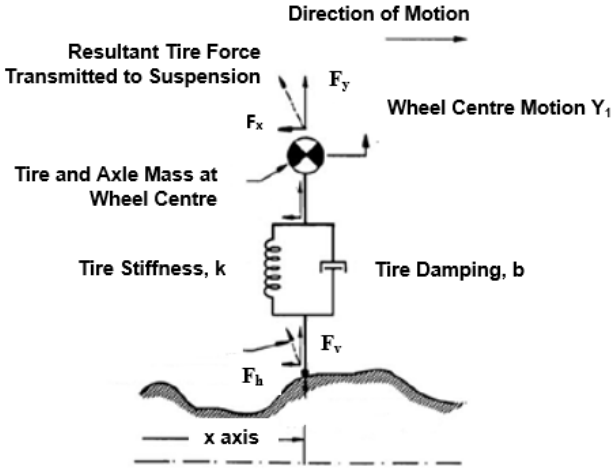

Figure 2-2: Point Contact Mechanism by Captain et al *[4]*.

The previous fixed contact patch model is further bettered by introducing the time-varying contact patch model of tires. This model ensures that the dynamic vertical load acting on the tire is the comprehensive contribution of the surface irregularities on the contact patch. The load that is found from this model is much closer to the experimental data. This is due to the equivalent concentrated stiffness of the tire changes with the contact patch. As an example, if there is sudden accelerating or braking, as the vertical load increases suddenly, then the contact patch will also vary suddenly. As more elements contribute to deforming the tire, the stiffness increases as opposed to the fixed contact patch model, where the stiffness decreases. As a result, this model may be considered a nonlinear time-varying model [6].

When a tire is able to absorb the vertical influence of surface irregularities, it is considered to have enveloping characteristics [6]. This allows for a better representation of the surface irregularities presents a more accurate calculation of vertical stiffness and force acquisition. The physical representation of the point-contact model, fixed contact patch and enveloping tire models are shown in Figure 2-3.

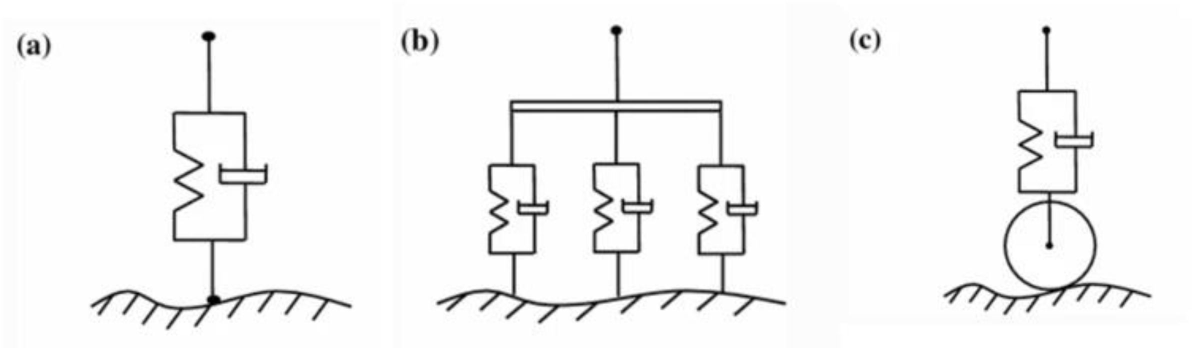

Figure 2-3: Tire-surface models: a) Single point contact model, b) Fixed Contact Patch model, c) Enveloping Tire-surface model *[6]*.

In 1984, Takayama and Yamagishi researched a mass-spring model having five degrees of freedom to obtain the tangential and radial axial forces as a result of rolling over a cleat [7]. The rigid ring is used to model the belt and tread region. The degrees of motion included the longitudinal, vertical, local longitudinal, vertical and rotational. The rigid ring parameters for a passenger tire 165SR13 were obtained form experiments. The tire was loaded at 1780N and driven at 40 km/h over a cleat in order to predict the longitudinal and vertical forces and modes of vibration. Their predicted forces were similar to experimental data. The rotational, longitudinal and vertical vibration modes were 40 Hz, 67 Hz and 74 Hz respectively. The lumped mass-spring tire model may be seen in Figure 2-4.

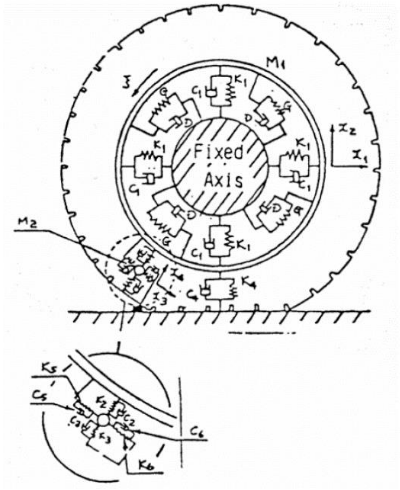

Figure 2-4: Takayama and Yamagishi’s Lumped Mass-Spring Tire Model *[7]*.

In 1993, K. Guo used a tire roller contact model for simulating vehicle vibration input using an effective road input [8]. The computer simulation consisted of a thirteen degrees of freedom vehicle model using two different tire models. His study concluded that the roller contact tire model gave better results and accuracy in comparison to the single point contact model.

In 1997, Davis created a tire model consisting of two-dimensional radial springs which cover the contact patch [9]. This enveloped the irregular displacements of the terrain and translated it to an equivalent ground plane which reflects the elevation and slope of the terrain and contact patch interface. He used three methods in order to predict the maximum displacement of the tire to capture an equivalent ground plane and the radial force exerted on the tire.

In 1997, A. Dhir and S. Sankar used the rigid tread band model where the point contact is replaced with wheel radius follower enabling the contact point to move relative to the wheel center. Their research showed that the single point contact did not allow for accurate modelling of the horizontal forces. [10] They also made use of the fixed foot-print model where the tire-ground contact is fixed over a finite footprint and replacing the single spring damper system to several systems. A more sophisticated adaptive footprint model was also used by A. Dhir and S. Sankar to model the dynamics of the tire-terrain interaction. They proposed a continuous radial spring and an equivalent damping element as shown in Figure 2-5a. Assuming an ideal wheel deflection by joining a straight line between the beginning and end of the contact patch, P1 and P1 shown in Figure 2-5b, they integrated the spring displacement over the contact patch to calculate the net footprint force acting on each wheel [10].

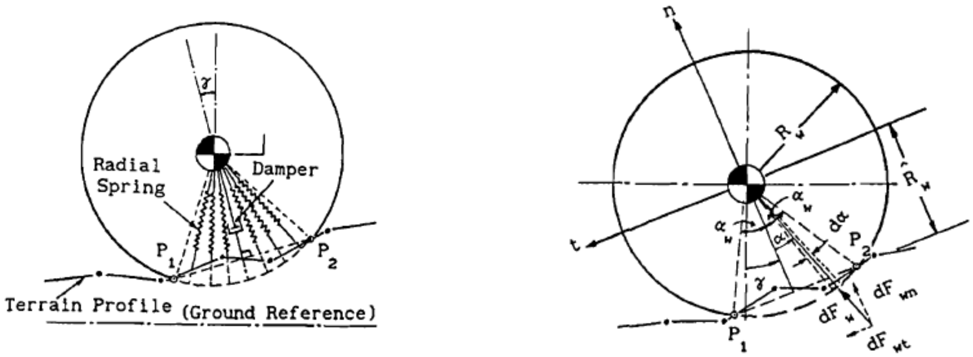

Figure 2-5: a) Adaptive foot-print wheel model; b) Calculating net foot-print force from idealized wheel deflection *[10]*.

They concluded that the proposed wheel model required the least computational time and yielded predictions with good agreement to their experimental data. However, the point contact model also performed well when the profile elevations were gradual [10].

In 1997, Kim and Savkoor made use of a rigid ring model but included an additional elastic spring element on the circumference of the rigid tire to incorporate the tread rubber compliance [11]. The elastic ring represented a flexible tread band along with the belts while the elastic foundation represented the sidewalls. The rigid ring parameters were obtained from vertical load versus deflection of a passenger car tire. The traction force distributions at the contact area and rolling resistance coefficients were calculated at different speeds.

The rigid-ring tire model by Zegelaar and Pacejka in 1997 [12], studied the brake torque vibrations induced on the tire during intermittent braking and can be seen in Figure 2-6. The tyre model is able to generate tire vibrations with a frequency range of 0-100 Hz. The tread is analyzed as a rigid body with respect to the rim. Because of its simplicity, accuracy and robustness, this model may be used in vehicle simulations efficiently. It makes use of the theoretical characteristics of a brush tire model. The tire tread band is modelled by a rigid ring on elastic sidewall. The tire tread has three degrees of freedom: the displacement in the longitudinal axis, the displacement in the vertical axis, and rotation about the wheel axis. Their studied showed that the rigid ring model represented the dynamic tire responses to brake torque variations accurately. The rigid ring parameters were successfully estimated using the measured frequency response functions. The model may be bettered in static experiments by changing from the brush type characteristics to the Magic Formula which was developed from earlier work.

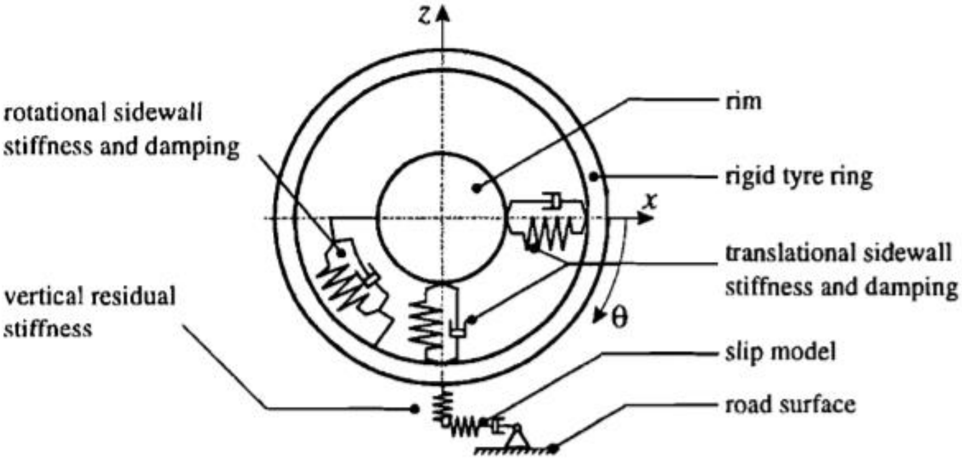

Figure 2-6: Rigid-ring tire model by Zegelaar and Pacejka [12].

In 1999, J. Sui and J. Hirshey extracts necessary parameters for the analytical tire models from a Virtual Tire Testing using LS-DYNA. They make use of the point contact tire model, equivalent plane tire model, effective road input tire model and the flexible roller contact model. It was concluded that the flexible roller contact model and the effective road input tire model were close to the Finite element tire model using simulations. The point contact tire and equivalent plane model seem to overestimate tire response to the road's profile [13]. The different tire models are represented in Figure 2-7 and Figure 2-8.

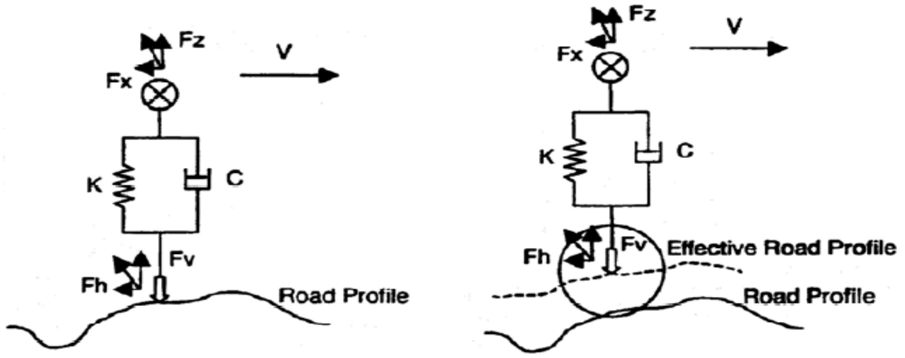

Figure 2-7: Point contact mechanism (left) and Effective road surface model (right) *[13]*.

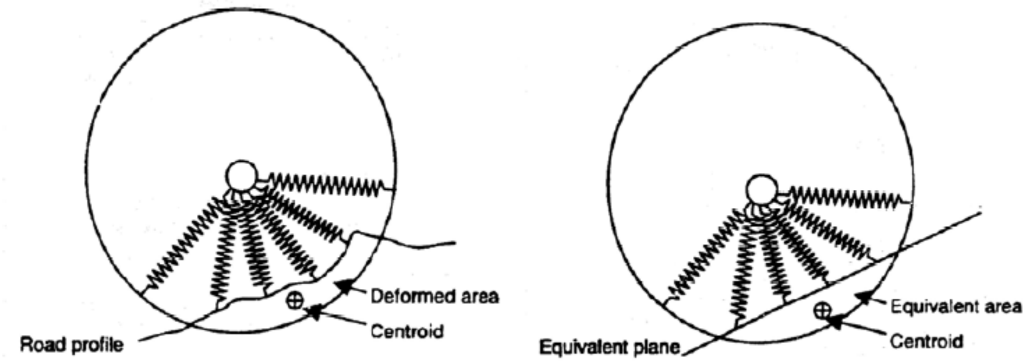

Figure 2-8:Representation of the equivalent plane tire-road contact model *[13]*.

In 2003, Cho et al. presented a new method of predicting the axle weight of a dynamic vehicle using piezoelectric sensors and an adaptive -footprint tire model [14]. The difficulty of weighing dynamic vehicles was surpassed by introducing a piezoelectric sensors signal which is constructed using the inverse dynamics of a high-pass filter. This signal is normalized using the tire's contact patch length obtained form the adaptive-footprint model. This study was performed on three vehicles ranging from 1,400 kg to 28, 040 kg. The new method showed more consistency in weighing a moving vehicle comparing to experimental data [14].

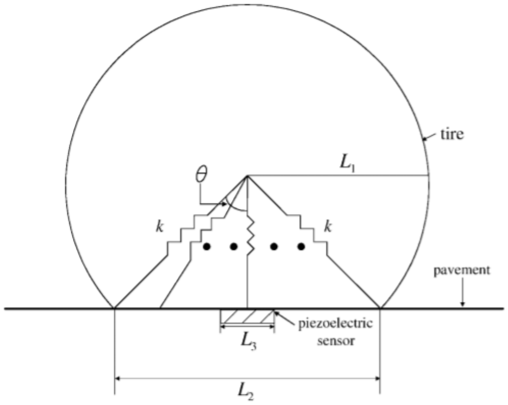

Figure 2-9: The adaptive foot-print tire model with a piezoelectric sensor integrated into model *[14]*.

In 2006, Chae et al. further improved the rigid ring tire model to include the out-of-plane tire parameters [15]. This model included the sidewall behaviour, tread and slip characteristics shown in Figure 2-13. In 2006, Chae obtained the rigid ring parameters for both in-plane and out-of-plane tire operation. These parameters were found using simulations as physical testing is costly. Chae developed a non-linear three-dimensional FEA tire model for a truck with size 295/75R22.5. The FEA tire model was validated by obtaining the in-plane and out-of-plane parameters with experimental measurements.

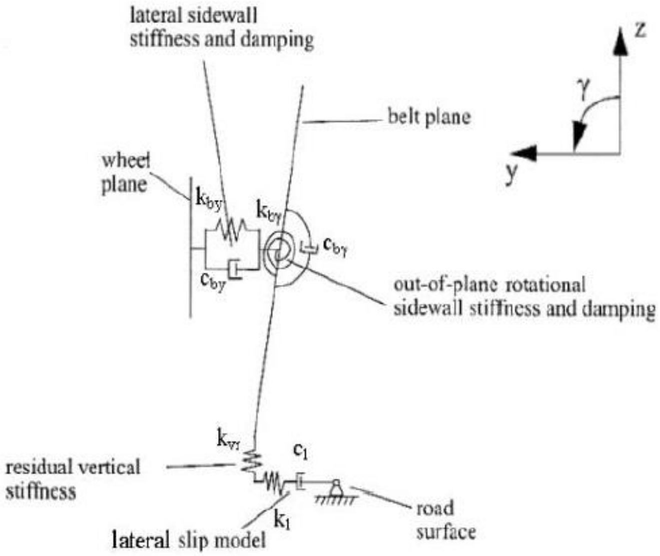

Figure 2-10: Chae’s Out-of-plane Rigid-ring model *[15]*.

In 2008, S. Kim et al. developed a tire model consisting of four components; a rigid ring, a six degree of freedom spring and damper system, a static circular beam and residual springs in the radial axis. In this study, the rigid ring corresponded to the inertia properties of the tire. The transient behaviour of the tire is provided by the 6-DOF spring which connects to the rim. The belts are modelled using a static circular beam element. Lastly, the residual stiffness in the radial direction is modelled using the radial springs. Using this model, S. Kim et al. estimated the radial deformation along the radial direction; radial deformation in 2D area as a result of a vertical load; estimation of the contact pressure distribution; shear deformation; forces and moments [16]. This tire model is represented in Figure 2-7.

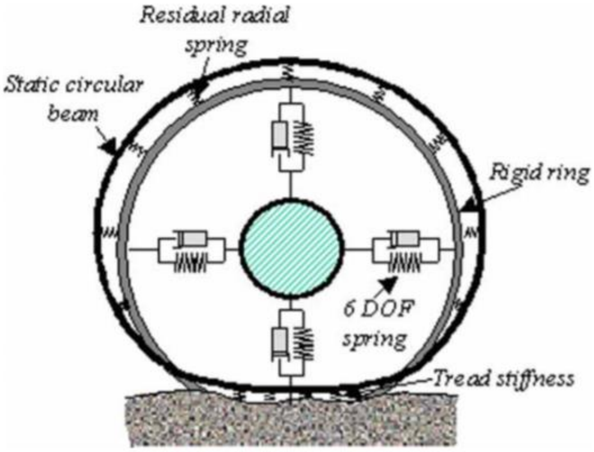

Figure 2-11: S. Kim et al's tire model *[16]*.

In 2008, J. Svendenius et al. made use of the brush tire model in which the pressure distribution is parabolic at the contact patch [17]. It generates tire forces by dividing the contact patch into regions of adhesion and sliding as shown in Figure 2-9. The tread volume between the tire and surface is modelled as infinitesimal elements of rectangular blades where each blade deforms independently and are linearly elastic in the longitudinal and lateral directions. Analytical expressions were obtained for the force contribution in the adhesive and sliding regions. The model was validated against empirical data at a speed of 48km/h and an inflation pressure of 2.4 bar [17].

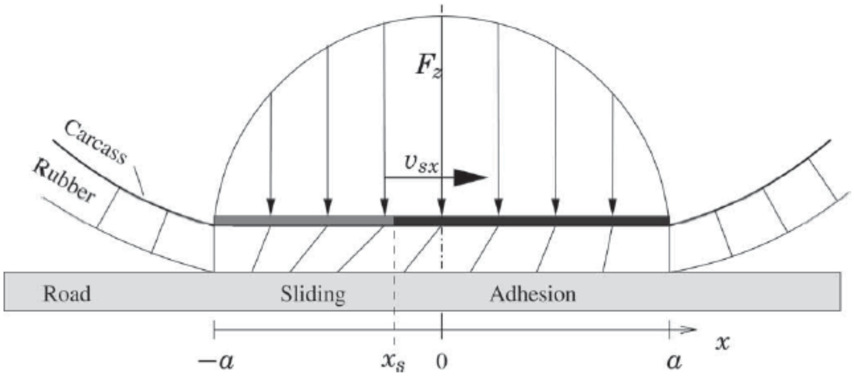

Figure 2-12: Brush tire model with regions of sliding and adhesion in contact patch *[17]*.

In 2009, Slade developed a novel rigid ring model with the incorporation of soft soil terrain dynamics in both in-plane and out-of-plane [18]. In addition, he studied the cornering characteristics of a passenger tire running on soft soil by determining the lateral forces over a slip angle range of 0 to 20 degrees. The self-aligning moment stiffness and relaxation length were also obtained. He concluded that the model is valid for up to 12 degrees. It was found that the passenger tire running on sandy loam soft soil had a rolling resistance coefficient of around three times higher than a hard road surface. The longitudinal slip stiffness for sandy loam was a quarter of the longitudinal slip stiffness on the rigid road. The sandy loam corresponds to a quarter of the tractive force compared to the rigid road. Due to the soft soil, the cornering stiffness decreased in comparison to rigid road.

In 2011, Futoshi and Yoshiaki made use of a distributed lumped mass-spring model where a rigid wheel is attached to several tire-masses by Voigt elements [19]. A three-dimensional interactive model along with a numerical simulation of the tire-terrain interaction with elastic deformation and soft ground with large displacements were developed. The soft terrain consisted of rigid soil particles. They found that their model's slip ratio and cornering performance agreed well with results of previous experiments [19].

In 2012, Madsen et al. [20] developed a three-dimensional vehicle/terrain interaction model. They made use of a tire and a deformable terrain model for use in real-time vehicle dynamic simulators. Instead of using the empirical terramechanics' models, they used physics-based equations. The tire uses a lumped-mass model with radial spring-damper mass distribution. A soil model was also created in conjunction with the tire to measure the vertical and later force and displacements of the soil. Ultimately, this data can be used to calculate the required energy and power to deform the terrain. Their model is represented in Figure 2-10.

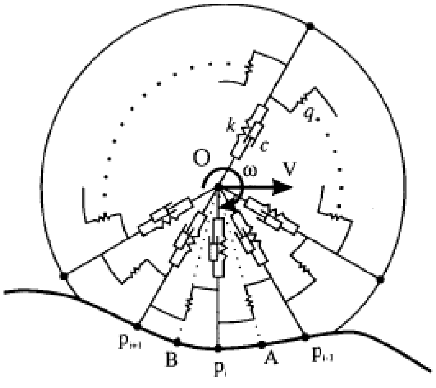

Figure 2-13: A Radial-interradial spring-damper tire model made by Madsen et al *[20]*.

2.2.2 FEA Tire Modelling

The finite element analysis has been extensively used in the automotive industry. The use of computational software to predict the mechanics and dynamics of vehicles under various conditions has been implemented since the 1970s. More specifically, tire mechanics and dynamics is studied to better tire and vehicle characteristics under different conditions.

In the early 1970s, finite element analysis served as a great method that allowed the generation of approximate solutions for deformation and internal loading of complex structures such as tires. The complex geometry of the tire or structure is mathematically predicted using simpler interconnected structural elements. Energy principles, flexibility, element stiffness, mass the loading matrices may be acquired and thus solve for displacements and forces at element boundaries using algebra.

In 1973, Zorowski made use of an FEA tire model where he predicted the profile shapes of an inflated tire under dynamic analysis [21]. He studied the effect of internal pressure on the profile geometry of the tire under specific dynamic loading. The results showed good agreement with the measured shape although a few difficulties were encountered. The stability of the iterative solution from element to element was really sensitive to the element size and the loading was to be applied in a gradual incremental load curve. This was time consuming as the calculations at each element needs to be stable before the proceeding load increments. The problem increased with unsymmetrical deformations causing large calculation time due to large carcass deformations where the analysis is based on the undeformed shape. His studies showed there is great potential for using FEA to model and analyze tires in comparison to prior analytical models.

In 1974, Ridha analyzed the deformation of the tire due to shrinkage by making use of the composite theory and finite element technique for modelling the material properties and the structural behaviour [22]. The temperature time lapse and the buildup of shrink forces during curing are obtained experimentally. A good relation is obtained between the calculated and experimental displacements. Further improvements of the solution and accurate experimental methods should obtain even closer relations. For future works, it was concluded that a closer study of the shrink forces and variation of the shrink force at different locations, and study of geometric stiffness through a nonlinear finite element analysis should be carried out.

In 1978, Young et al researched the interaction of a tire and a soil terrain [23]. A previously developed model is improved in order to include the effect of flexibility of the tire's carcass where as the vehicle is on the verge of moving, there is energy losses. The comparison between the analytically calculated drawbar pull and the experimentally obtained drawbar pull for three types of tires showed a strong correlation and deemed FEA as an accurate representation.

Tielking modelled a four-ply bias tire as finite elements to study the tire-pavement interaction [24]. The study focuses on the model's ability to calculate the effect of tire design variations on the tire performance. The different effects of nylon and polyester cords on the deformation of the tire, contact area pressure distribution and traction was analyzed.

The vast use of agricultural vehicles in the 1900's led to more research being conducted on agricultural tires. In 1994, Hu et al investigated the mechanical characteristics of a rubber tire and its interaction with a rigid surface using a two-dimensional finite element model [25]. The model consisted of a rigid rim and a rigid contact surface. Several distinct elastic parameters were used to model the beads, sidewall, tread and lugs. The boundary conditions included variation of tire loads and inflation pressures along with different displacement of tire and friction between tire and the surface. The tire deformation, lateral and vertical displacements, normal contact pressure, frictional forces and stress distribution of the tire were studied using Finite Element Method and showed good results in comparison to measured data. The accuracy seemed to show more at higher load and inflation pressures.

In 1999, Shida et al. conducted a rolling resistance simulation method for tires in terms of a static finite element method [26]. Their aim was to enable easy input data preparation, less computational time and reasonable accuracy. A static deflection analysis was conducted before the stress and strain were acquired in conjunction with the material's losses in order to predict the energy dissipation of a rolling tire. Using hysteresis loops, the dissipation energy density of the element group was acquired. These simulated results were compared to the experimental loss factors of the rubber using the homogenization theory of dynamic viscoelasticity and predicted the rolling resistance accurately.

A vehicle's movement on unpaved surfaces is vastly seen in the military, agricultural and construction industry just to mention a few. As a result, the research of the tire-terrain interaction for off-road purposes should be studied. In one study, Shoop et al, created a three-dimensional finite element tire model to simulate a tire running on snow [27]. The snow is modelled as an inelastic material and made use of the critical-state constitutive modelling technique along with the plasticity theory. The snow was validated based on the mechanical deformation of snow using a plate sinkage test. Various tires of different size and applications in the freight and off-road military purposes were rolled on snow at several depths. The combination of the tire-terrain model was validated using force measurements obtained from instruments within the vehicle along with the snow deformation. Their study showed an accurate representation of the rolling resistance forces and snow deformation for the simulations conducted.

In 2007, Korunovic et al. conducted a static analysis on a tire using FEM [28]. A tire was modelled and a static stress analysis was done. The tire shown in Figure 2-14 shows the loading done on the tire model. Initially it is mounted, then inflated to various inflation pressures and lastly a rigid body is pressed at a quarter of the normal vertical load onto the tire. The carcass tension in terms of the meridional distance at different inflation pressures was obtained. A finer mesh at the beads boundaries proved to show better results for the contact stress distribution.

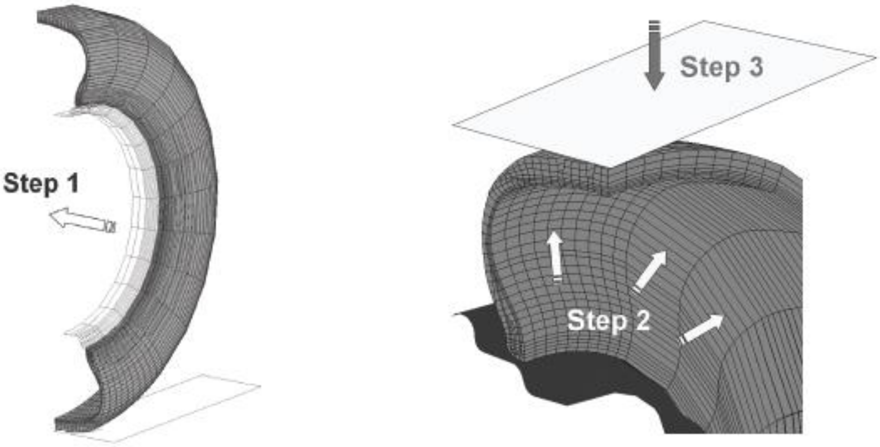

Figure 2-14: Loading steps on the static tire analysis by Korunovic et al *[28]*.

In 2000, Kabe et al. [29] studied the characteristics of tire analysis by use of FEM and an implicit/explicit finite element analysis was conducted. The steady state cornering simulations were done in implicit code while the transient cornering simulations were done using the explicit code. Cornering simulations at seven different slip angles of 0°, +1°, -1°, +2°, -2°,+3°,-3° inflation pressure of 200 MPa, vertical load of 4kN and velocity of 10 km/h were conducted. The cornering force and self-aligning torque were measured at the various slip angles. The contact stress distribution for the tire was also obtained. The predicted cornering forces of a passenger car's tire using both implicit and explicit simulations proved to show consistency with the experimental results obtained from MTS Flat-Test Tire Test Systems. They found that the implicit analysis had around 30 times less computational times compared to the explicit analysis.

In 1998, Zhang et al. used a finite element tire model for vibrational analysis. A tire model was developed for vehicle dynamics analyses and ground simulations [30]. The model was validated through static and dynamic simulations such as the lateral stiffness, free-drop test and low speed rolling cornering stiffness. The 3D free vibration and forced vibrations with a rigid surface was also studied. Their novel approach of using the explicit nonlinear dynamic finite element code compared to the NASTRAN modal analysis proved to be successful. The simulations were conducted in LS/DYNA3D in the time domain where the vibration modes were produced using the Fast Fourier transformation.

In 2006, Chae [15] modelled a truck tire model of size 295/75/R22.5 used for hauling purposes. The tire was created using a three-layer membrane elements, solid elements of hyper elastic materials and beam elements. The tire was validated through several static and dynamic tests. Due to its efficiency, he used the rigid ring model to model the tire and obtain the in-plane and out of plane rigid ring parameters through virtual simulations. These rigid ring parameters are compared to physical measurements and showed good agreement. The Vertical displacement, tire contact force and moments were validated through simulations. The dynamic in-plane and out-of-plane tire responses under a variation of tire loads are predicted. Additional load is also added as a sprung mass and a suspension system is incorporated in his model to resemble a quarter vehicle model and can be used in real vehicle applications. The quarter vehicle model under different running speed rolling over a ditch of 45° and 90° showed good agreement with physical measurements.

In 2008, Allen et al. [31] also developed a rigid ring quarter-vehicle model with the use of a road profile algorithm to predict tire durability and ride comfort. A new five-degree of freedom in-plane rigid ring quarter vehicle model along with a force dependent effective road profile is found and programmed in Matlab/Simulink. This model used the tire-terrain's vertical contact force to update the effective road height and slope at every time step integration. The model simulated the response of a free rolling tire over road surface with irregularities. As Chae did, Allen validated the model using tire spindle vertical acceleration data from the FEA quarter-vehicle model tests. His studies showed that the force dependent effective road profile showed a better representation of the vertical tire spindle acceleration in comparison to the force independent effective road profile.

In 2009, Dhillon et al. [32] developed a truck tire – soil interaction model using FEA and Smoothed-Particle Hydrodynamics. The tire is modelled based on standard heavy vehicle tires. It is validated by performing the static deflection, contact footprint and first mode of vibration in a dynamic analysis. The soil is also validated using pressure sinkage and shear strength tests. The tire is rolled over the soil to obtain the rolling resistance and tire forces which show good correlation to available experimental data for the same tire.

In 2009, Mohsenimanesh et al. [33] conducted a research on the modelling of a pneumatic tractor tire and its interaction with multi-layered soil. The contact pressure distribution for various vertical loads and inflation pressures was studied. The tire model incorporated the geometry and orientation of the cords in each ply, the incompressible property of the tread rubber block and the non-linear and large deformation of the carcass. The soil was modelled as a linear three soil layers and a hardpan layer. The simulations were conducted on ANSYS FE software and the contact pressure distribution were analyzed. The simulation results were compared to the measured data and showed good agreement of pressure distribution at the tire-soil interface under varying loads and inflation pressures. The predicted peak tire-soil interface pressures were found to be around 32%-53% less compared to the field test data.

Ragheb et al. developed a three-dimensional, non-linear Finite Element off-road tire using ESI's PAM-CRASH application as seen in Figure 2-15 [34]. The trends of vertical load deflection, cornering characteristics and self-aligning moment on rigid terrains were predicted and compared to published measured data for validation. The first mode of vibration was obtained by performing a drum-cleat test for a tire load of 26.7 kN and an inflation pressure of 7.58 bars. The first mode was found to be 46 Hz due to its large diameter and softer tire material. The tire is also rolled on a rigid surface for slip angles of 0, 2, 4 and 6° and the cornering force is obtained which had excellent agreement to measured data provided by Michelin. Similarly, the aligning moment, vertical stiffness on soft soil, rolling resistance on soft soil had good agreement with measured data. The tire models are used to study the multi-pass behaviour of the wheels rolling and steered on soft terrain.

Figure 2-15: Hossam Ragheb's combat vehicle FEA tire model for an 8x8 combat vehicle *[34]*.

In 2015 Reid provided a detailed analysis of the construction, validation and applications of a wide base tire modelled in FEA as shown in Figure 2-16 [35]. An optimization algorithm was used in order to tune the parameter of its materials until the behaviour of the FEA model agrees with the behaviour of the physical tire. The optimized tire model had an error of only 1.78% between the rolling resistance force obtained from simulation and physical experiments. The FEA wide base tire was used to generate the in-plane and out-of-plane rigid ring model on rigid surfaces. An increase in the inflation pressure resulted an increase in total static vertical stiffness, total dynamic vertical stiffness, translational stiffness and lateral stiffness. On the other hand, the translational damping constants decreased with increasing inflation pressure.

Figure 2-16: Adam Reid’s wide base FEA truck tire (right). Real Michelin wide base tire (left) *[35]*.

In 2016, Marjani constructed a new virtual wide-base tire model and validated it on hard surfaces [36]. The rolling resistance on various soft soil models was performed through PAM-CRASH software. The soft soil is validated through the shear-displacement and pressure sinkage tests through simulations. It was found that the SPH method has long computational solving time and as a result, a hybrid soil model is studied and changed to achieve a lower computational time with reasonable accuracy. The rolling resistance is simulated at different vertical loads and inflation pressures and compared to physical results. It was found that the use of the hybrid soil model reduced the computational time by almost half.

2.3 Soil Modelling

This section will cover the literature review of soil modelling conducted FEA and SPH soil models. Past research and necessary background in each of these models are presented. The study of soil mechanics has been expedited since the mid 1950’s. As an example, terramechanics has been the overall performance of a machine in relation to its terrain of operation. It varies from the agricultural applications, automotive industry, and off-road construction as major parts of its application. The computational efficiency of finite element analysis has paved way to model soil through different virtual techniques and will be discussed.

2.3.1 FEA Soil Modelling

Finite Element soil modelling is conducted in many sophisticated engineering problems including geotechnical problems. The study of soil and rock terrain has great capabilities in several engineering fields. The study has expanded in civil engineering, mechanical engineering and automotive engineering just to name a few.

In 1972, Marr et al. [37] used finite element analysis of elasto-plastic soils for application to lunar earth sciences. The sensitivity analysis of the stress-strain behavior of soils is investigated. The models assume a small strain theory which include a non-dilant, a dilant and a strain hardening constitutive relation. Another two models were created using a large strain theory which include a hyperbolic and a tresca elastic perfectly plastic material. The soil models were used to analyze retaining walls and footings. The solutions were found to be very for the failure load of the retaining walls in the drained frictional soil.

In 1990, Chi et al. [38] developed a three-dimensional finite element model to simulate the soil cutting with a tillage tool. The model applied was the hyperbolic stress-strain for the constitutive relationship of soil. They concluded that it is feasible to use soil parameters obtained from triaxial and shear strength test to accurately predict the forces on the tools by making use of the Duncan-Chang stress-strain model. The simulations showed that the force opposing the tool increased as the displacement of the tool increased in the travel direction. As the displacements increased, the reaction force on the blade did not increase as much and the soil structure is said to have failed. This reaction force is used as the cutting force for cutting the soil.

In 2015, David et al. [39] studied the interaction of structural elements and a soil medium using a 2D finite element analysis. It was found that the main concern in regards to modelling soil-structure interaction is the accuracy of replicating soil behaviour in varying simulations. This literature study concluded that the most common soil constitutive models are the Mohr-Coulomb model, hyperbolic model and Modified Cam Clay model.

Later in 2017, Ungureanu et al. [40] researched the FEM modelling of soil behaviour under compressive loads. As mentioned before, soil compaction is a critical form of degradation of agricultural soils. The soil compaction is greatly influenced by the magnitude of the vertical load, moisture within the soil, size and shape of the contact patch area, type of soil and number of passes. In this study, simulations were conducted on a cohesive and a non-cohesive soil with known properties. The stress distributions under loads of 4.5 kN and 21 kN with different footprint sizes were obtained for the two different soils. Their research concluded that soil stresses increase with wheel load and vary according to the type of soil.

2.3.2 SPH Soil Modelling

The fundamentals needed for Smoothed-Particle Hydrodynamics technique for modelling particles and the previous research done on SPH soil modelling is covered within this section. Finite Element Analysis (FEA) was preliminary used to model soft soils for tire-terrain interaction purposes. However, several researches have proven the superiority of SPH technique over FEA to model soil shear characteristics [41]. The shear characteristics of soil are significantly important when computing the rolling resistance of off-road tire operations.

2.3.2.1 SPH Fundamentals

SPH is a technique used in application where continuum is needed in modelling and simulation. It was invented for computation and simulation of astrophysical problems ad has been very useful in Computational Fluid Dynamics (CFD) [42]. It does not use a grid/mesh but instead it uses Langrangian formulation and allows for ease of computation in movement of particles [42]. The movement of these particles are portrayed in time history. SPH particles contain material properties and their interactions are varied using a smoothing function [42]. These functions include partial differential equations such as the Navier-Stokes formula and computes variables such as density, energy, velocity and acceleration locally [42]. Since the particles relative position and state are represented in time history and a finite continuum, the particles may undergo large deformations [42]. The interaction between tire and soil contains complex motions and is represented accurately using SPH methods.

FEA to SPH

FEA uses meshes or discretization of small subdomains within a continuum [42]. Meshing may be limited in complex problems as it must have similar numerical and physical compatibility conditions [42]. As a result, problems with free surfaces, moving boundaries and extensive deformation are difficult to compute. It is more optimal modelling the sand in SPH instead of FEA due to the large deformation of sand. In FEA the material deforms to a large extent and element tingling occurs [41]. This renders the FEA results as no longer reliable and therefore SPH is needed [43]. SPH material enables the terrain to be modelled as a sphere at its center of mass. These particles are accompanied with a mass, velocity and a stress state which are generated using conservation equations.

Smoothing Length

The smoothing length is an important parameter in regards to SPH formulation. This formulation consists of an integral representation of the particles field functions and also its approximation [44]. The smoothing length is used within the integral representation of a field function and defines the area of influence of the smoothing function [44]. The smoothing length of the SPH particle changes at different time steps according to the kernel function [44]. As the distance between particles increase, the smoothing length increases and as this distance decreases, the smoothing length also decreases. The particle's domain of influence and the maximum and minimum smoothing length are shown in Figure 2-17.

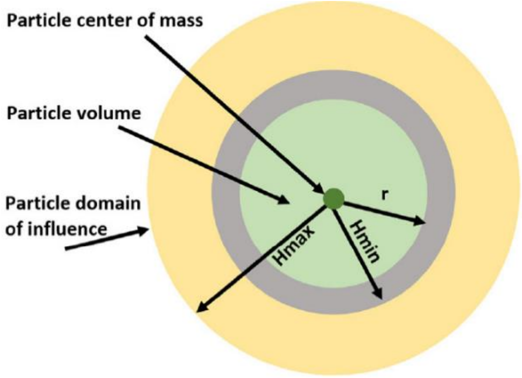

Figure 2-17: SPH Particle with radius r, Max and Min Smoothing lengths *[45]*

Monaghan-Gingold Artificial Viscosity

When using SPH particles an artificial viscosity is applied to the particles in order to dissipate local velocity differences between particles. These local velocities are converted into heat and therefore creates entropy within the particle [44]. This entropy does not allow the particles to penetrate each other and have post shock vibrations [45].

The Monaghan-Gingold viscosity allows for shocks to be simulated as it spreads the shock over many adjacent particles [45]. Furthermore, this viscosity has three desired features. It is a Galilean invariant, the viscosity vanishes for rigid body rotations, and it conserves total linear and angular momenta [46]. The

LETE sand particles are modelled using three Monaghan-Gingold artificial viscosity parameters of 0, 1.5 and 3 obtained from Zeinab's soil calibration [47].

Contact Thickness

In order to simulate the interaction of LETE sand particles with the box or tire, there must be contact between the box/tire and the sand particles. The contact type used for the sand soil and box interaction is an asymmetric node to surface contact type where the slave nodes do not penetrate the master segments. Within the material and part card, a contact thickness is inputted for the LETE sand particles. This thickness is the distance away from the mid surface of a master segment at the contact surface between the master and slave segments [48]. The contact thickness is illustrated in Figure 2-18.

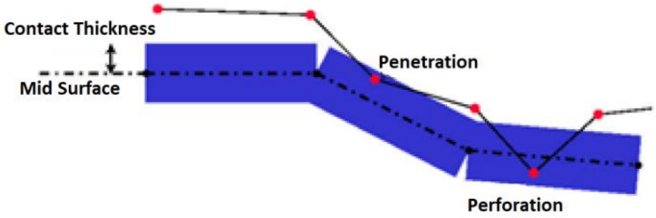

Figure 2-18: Contact thickness, penetration and perforation between master and slave segments *[48]*

The remainder of this section will cover the research conducted using Smoothed-Particle Hydrodynamics technique. The applications of the research range from fluid dynamics, soil flow analysis and other geotechnical problems. In this study, the soil applications involving SPH are covered.

In 2007, Bui et al [49] used the application of SPH to simulate soil-water interaction. The water is modelled as a viscous fluid with low compressibility and the soil is modelled as an elastic-perfectly plastic material. The plastic flow regime and the stress states of the soil apply the Mohr-Coulomb failure criteria. The dry soil model is a one phase flow while the saturated soil have both water and soil phases. The soil-water interaction is obtained by finding the pore water pressure and seepage force. Simulations of the soil excavation using a water jet are calculated. Excavation is carried out on the dry soil and fully saturated soil separately. Their research proved that the numerical results of soil failure through gross discontinuities is valid.

In 2010, Lescoe et al. developed new soil models using both FEA and SPH. The importance of mesh size, soil plot size and edge constraints are studied [50]. The SPH parameters for the soil are determined for complete and partial replacement of FEA elements in the soil model as a hybrid of FEA and SPH. The rolling resistance tests are obtained through simulations using FEA, SPH and FEA/SPH soil models. This study showed that using a high depth of SPH particles increased the rolling resistance. On the contrary, increasing the SPH particle density had minor effects on the rolling resistance [50].

In 2011, Blanc et al. [51] made use of a stabilized SPH Taylor-Galerkin algorithm for researching soil dynamics problems. The problems of using FE in geomaterials include the volumetric locking, influence of mesh alignment resulting in unrealistic failure surfaces, not optimal propagation properties of diffusion and dispersion and large deformation analysis. The paper contains how the Taylor-Galerkin method can be further applied to a meshless formulation such as the SPH technique. The advantage of this method included better accuracy due to the use of stresses and displacements as nodal variables which avoids tensile instability. The algorithm was assessed in cases such as elastic propagation of waves in a bar and failure of a vertical slope of a cohesive soil. The study showed that the model has good propagation properties, it avoided tensile instability, acceptable results for soil slope stability and providing valid definitions of shear bands.

Huang et al., in 2011, [52] adopted the SPH to study the flow processes of liquefied soils. The Bingham model along with the Mohr-Coulomb yield criterion, equivalent Newtonian viscosity and the verlet neighbor list method is applied in the SPH framework to create an algorithm for flowing of liquefied soils. A shaking table test is used from literature for SPH analysis to validate the SPH method. The simulations produced the flow process of liquified soil and estimate the horizontal and vertical displacement, and the soil velocity after liquefaction. The corresponding points of extracting the simulated data matches the shaking table test and the simulated results match well with the physical test results.

In 2013, Dhillon et al. [53] modelled a soil using the SPH technique and validated using the pressure sinkage and shear strength tests. A dry sand, clayey soil (Thailand), and heavy clay soil models were validated. A truck tire is modelled and validated by obtaining the static deflection, contact footprint and first mode of vibration. The tire was rolled over the SPH sand and the results showed higher accuracy compared to FEA models for soft soils. The rolling resistance on the SPH soil was higher than the FEA models. The FEA soils did not show the same penetration and shearing of the soil layers comparable to a more rigid soil.

Later in 2013, Dhillon et al. [54] examined the design parameters of the SPH materials. The influence of mesh configuration, particle orientation and interaction properties were researched. The mesh configuration has a great influence on the compressive and shearing properties of soil. Using a tetrahedral mesh, the soil had a larger sinkage due to higher shearing resistance in comparison to the hexahedral mesh. A larger smoothing length, the sinkage increased and less shearing resistance.

One study by Grabe et al. [55] studied two scenarios where he used SPH soil and water particles in the study. The tests include a drainage of water from a vertical sand column, and seepage through a vertical dam. A sand column of dimension 4 m height and 0.6 mm thickness is used to contain fixed sand particles which exert a force of interaction with the water particles that are under the force of gravity. The second scenario included the seepage of water particles through fixed sand particles in a vertical dam, also known as the Muskat problem. This study implemented drag force into the equations of conservations for the SPH particles using Darcy's law. The results for the simulation and analytical solutions agreed very well in terms of seepage through various dam thickness.

Later in 2015, Grabe et al. [56] extended their previous study to a truly coupled analysis and made use of a two-phase model for saturated soils. Contrary to the initial study, where the soil particles were fixed, the soil particles were subjected to displacements. The soil is constructed of a hypo plastic constitutive model and considers a liquefaction threshold in low effective stress and tension cases. The two phase model, including water and soil, are studied including laminar and turbulent flow. Several methods of evaluating the interaction coefficients were introduced and evaluated. Four tests cases were simulated and showed that the SPH model is capable of produce good results, especially when soil water interaction with large velocity impact and large displacements are studied.

In 2018, Mao et al. [57] studied the behaviour of lunar dust on the moon using SPH particles. The complications of dust particles on the moon include having a small lunar gravity and subjected to the influence of an electrostatic field in the universe. The understanding of the particulates is essential for exploration of the moon. The SPH model with elastic-perfectly plastic constitutive equation and Drucker-Prager yield criterion are applied to the simulation. The simulation studied a cohesive soil's natural failure and electrostatic transport of charged soil particles under an electric force and lunar gravity. Their simulations proved that SPH is a reliable method in studying the behaviour of soil particles under a complicated electric field and low gravity.

2.3 FEA Tire Terrain Interaction

In 1978, Yong et al. [58] used finite element analysis to analyze and predict the tire-soil interaction and performance. A previously developed estimation of rigid tire-soil interaction is improved to include the effect of a flexible carcass so that the energy loss in the development of movement is accounted for and a simpler boundary condition specification using the input load. The drawbar pulls for the predicted (FEA) and the experimental testing have good correlations.

In 1997, Hiroma et al. [59] developed a viscoelastic model of soil to investigate the tractive performance of a tire rolling on a soft terrain. Using finite element method, the stress distributions under the tire while taking into consideration the friction and adhesion between the tire and terrain was analyzed. The wheel was sunk into the soil and moved with a constant contact load, velocity and slip. Their results showed that the maximum normal stress was seen at the front of the tire and the lowest point of the wheel. The tangential stress increased in the rear part of the contact patch. Their results showed good agreement with experimental results and the tractive performance was estimate at various slip angles.

In 2000, Liu et al. [60] conducted a large strain finite element analysis of sand. The model, its algorithm and application to the numerical simulation of the tire-sand interaction is discussed. A new nonlinear elastic law is suggested for the response of geomaterials. An implicit return mapping algorithm for elastoplastic models of the geomaterials is presented for large strain applications. The tangent moduli are derived and a modified critical state model along with the new nonlinear elastic law is applied in the FEA software MARC. The simulations of the tire-sand model using the proposed model was conducted. It was found that considering the large strains yields more accurate numerical results. In comparison to the drawbar pull experimental data, the simulations had relatively close agreement. The predicted and measured stress distributions also showed good agreement. Further improvements include studying the friction law as it has a great impact on the contact pressure and friction force along the tire-terrain interface. The shearing behaviour needs a more accurate representation for the rolling-slipping process in order to obtain more realistic results. The conventional finite element method does not consider the local failure and the large flow of sand under the moving tire.

In 2001 Shoop [61] incorporated theoretical mechanics within off-road vehicle performance by using numerical modelling techniques. A full 3D tire model simulating a rolling tire over deformable terrain was developed. The tire’s were simulated using a rigid wheel, a deformable tire, and modal analysis tire models were used. The study found that the simplified tire model was computationally efficient. However, the modal analysis model gave better contact stress distribution. Each tire model was combined to roll on deformable terrain. The critical-state plasticity model was used for the fresh snow and compacted sand surfaces. The tire terrain model was validated using field measurements of snow deformation and tire forces.

In 2010, Han et al. [62] created a three dimensional FEA tire and soil model for off-road purposes using ABAQUS software. The tire had specifications of 175R14. The steady state static tire-soil model was analyzed for the stress, strain and deformation of the tire and soil under a specific sinkage value. The relationship between the applied load and the contact pressure was also obtained to help further study the tire-soil interaction under more critical conditions.

In 2011, Xia [63] introduced the fundamental formulations on soil compaction and tire mobility using finite element analysis The Drucker-Prager model is implemented in ABAQUS software in order to model soil compaction. A finite strain hyper elasticity model is created to model a nearly incompressible rubber for the tire material. The transient spatial density as a result of tire compaction on the terrain is modelled. The effects of tire inflation pressure, rolling speed and frictional properties on the rolling radius, acceleration, traction and torque are obtained from the tire-terrain FEA model. The research proved that the numerical model serves as a robust tool to predict the soil compaction and tire mobility.

In 2012, Nankali et al. [64] researched the stress analysis of a tractor tire which interacts with soil using a two-dimensional finite element method. Their objective included developing a model for soft soil in response to tire pressure and axle loads using FEM. A two-dimensional axisymmetric Drucker-Prager material was used with the model for analyzing the soil behaviour under a variation of loads and inflation pressure. A maximum soil/tire pressure of 83.7 kPa was obtained for an inflation pressure of 70 kPa and axle load of 12 kN. This simulated result was around 30% less than the stress at the contact patch obtained from experimental data. In addition, the maximum distributed stress was found at the tire side wall and proved the finite element method modelled the tire-soil stresses with reasonable accuracy.

In 2013, Li et al. [65] used the finite element method to analyze the soil compaction and tire mobility. Soil compaction causes soil degradation and accounts for the increase of soil strength. Two finite element tire models were created based on the geometry and size of the Bridgestone bias tire. Physical experiments were conducted using a single wheel tester to validate the FE tire and soil model. The effect of axle load and inflation pressure on the soil compaction was researched with a finite element tire model using coarse meshes. This ensured the computational efficiency is increased while maintaining simulation accuracy. The impact of inflation pressure and vertical axle load on the soil compaction varies at different soil depths. The inflation pressure greatly effects the topsoil compaction where the vertical load greatly affects the lower soil. The relation between the slip ratio, slip angle and tire mobility was researched through virtual simulations using fine meshes. Lastly, the effects of axle loads and inflation pressure on the dynamic behaviour or the tire were studied. A lower inflation pressure shows a larger drawbar pull, braking force and cornering force and lower rolling resistance. The FEA model for the agricultural tire and soil model is shown in Figure 2-19.

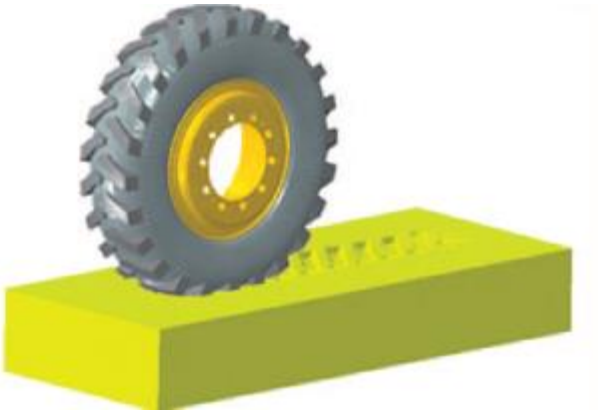

Figure 2-19: Li's FEA agricultural tire running on soft soil terrain *[65]*.

In 2017, Lardner [66] predicted the off-road rigid ring model parameters for a truck tire and soft soil interaction. The in-plane and out-of-plane rigid ring parameters were determined for a Regional Haul Drive (RHD) truck tire at several operating conditions. The study showed that the most of the in-plane parameters were strongly influenced by the inflation pressures. The influence of inflation pressure on the total equivalent vertical stiffness on dry soil was determined. The cornering stiffness was found to be load dependent. However, the inflation pressure influenced the cornering stiffness at very high vertical loads.

In 2018, El-Sayegh et al. [67] modelled and predicted the tire-snow interaction by obtaining the rolling resistance coefficient. An off-road truck tire of size 315/80R22.5 was modelled using FEA and simulations were conducted in the static and dynamic response of the tire. The tire was validated against published measured data for the given tire. Snow particles are modelled using SPH with hydrodynamic elastic-plastic material and calibrated to measurements found in terramechanics data. The forces generated in simulations are through the node-symmetric node-to-segment with contact edge treatment. The rolling resistance coefficient of the tire-snow interaction is calculated for several vertical loads, inflation pressure, tire longitudinal speed and snow depth.

2.4 Chapter Summary

This chapter covered the literature review and background knowledge for the modelling and dynamic analysis of tires and their respective surfaces or terrains. The FEA research on tires have been vast through out the past few decades. This chapter summarizes the research for tire stress, vibrations, vehicle dynamics and surface stresses. The simulations conducted on many FEA models have been validated through experimental or measured data. It has been found that the FEM has been successful in predicting the forces and mechanics of tire-terrain interaction. A novel approach to modelling sand using Smoothed-Particle Hydrodynamics and its benefits have been covered.

Since 2006, the study of vehicle tires on terrain has led to state-of-the-art tire-terrain models. The virtual simulations conducted in ESI's PAM-Crash and other software have become more sophisticated with the study of several types of tires running on different types of terrains such as water, snow, soil/water mixture. The study of soil stress and compaction along with tire characteristics have been conducted.

A novel approach to studying agricultural tires on soil has been proposed using the SPH technique. The accuracy of the SPH technique will be utilized in conjunction with an FEA tire model to study the dynamics of a High Lug Farm Service agricultural tire and Clayey Loam soil. The off-road rigid ring parameters will be predicted along with a study of soil dynamics under a variation of load and inflation pressures.

CHAPTER 3 MODELLING AND VALIDATION OF HLFS TIRE

3.1- Introduction

This chapter presents a new High Lug Farm Service (HLFS) agricultural tire size 220/70B16 tread design used for off-road agricultural operation. The HLFS tire is modelled using Finite Element Analysis (FEA) technique in Visual Environments Pam-Crash software. The HLFS tire rubber is modelled using a combination of different materials including the Mooney-Rivlin material for rubber parts. The Mooney-Rivlin material is an elastic plastic material and it accurately resembles the mechanics and behavior of rubber used in tires. The Finite Element Analysis (FEA) tire model is then validated against manufacturers provided data for several tire characteristics including radial, lateral, and tangential stiffness.

3.2 FEA Tire Modelling

The HLFS tire model was designed in reference to an FEA model of the off-road Michelin Stryker tire that was previously modelled and validated in previous research work [68]. The FEA Michelin tire size 12R20 was scaled in all directions to match the size of the HLFS tire as a 220/70B16. First the Michelin tire was changed by deleting all the tread pattern elements from the tire resulting in a bald tire. This bald tire was scaled smaller in size to that of the HLFS bald tire in order to get proper sidewall width, tire width and height dimensions. The Michelin tire was scaled by a factor of 0.76754 in both the z and x axis and a factor of 0.62857 in the y axis. This resulted in very accurate sidewall width, tire width and height dimensions.

3.2.1 FEA Lug Design

A single lug was designed on the bald tire by first creating nodes which covered the lug's dimensions. The lug is 140 mm long, 25 mm wide at the contact patch and has 30 mm depth. It was found that the connection between the bald tread and the lugs were stronger and more well connected by ensuring there were maximum possible nodes on the bald tread which coincided with the nodes created for the lugs. Furthermore, the lug's wireframe was designed by creating nodes at the corners of the upper portion of the lug. Afterwards, solid elements were created by connecting 6 nodes using the three-dimensional node option. The designed hexa solid elements were then re-meshed into a finer mesh in order to insure more accuracy in the contact algorithm calculations. Since the lugs have an offset of 8 degrees on each side, another lug was created on the opposite side with an 8-degree rotation about the tire y-axis from the initial lug using a similar methodology.

The single lugs designed on both sides of the tractor tire were then rotated 19 times about the tire center using an angle of 18 degrees. This created the full HLFS tire tread with a total of 40 lugs equally spaced out between each other. The nodes created on the surface of the bald tread due to these lugs are now duplicated due to the rotation of the lugs. All coincident nodes for which the maximum gap was less than 0.1 mm were eliminated and fused. This ensured that the coincident nodes between the lugs and the bald tread were the only ones found in the check. These coincident nodes were then fused in to one node as to create a fully connected tread pattern. The lugs and the under tread were then joined together into one part and compared to the Michelin Stryker as seen in Figure 3-1.

Mooney-Rivlin material was assigned to the designed tread. Research indicates that this material best describes many plastic elastomers which includes natural rubber [69]. The isotropic elastic behaviour of the Mooney-Rivlin material was represented by the strain energy density function W. The function W is a linear combination strain invariants or coefficients of the characteristic polynomial and can be seen in Equation 3-1.

$$W = \sum_{i=0}^{n} \sum_{j=0}^{n} \sum_{k=0}^{n} C_{ijk} (I_1 - 3)^i (I_2 - 3)^j (I_3 - 1)^k \qquad (n = 1,2,3 \ldots.,\infty) \qquad (3\text{-}1)$$

Within the strain energy function, I_1, I_2, I_3 are the strain invariants. Equation 3-1 may be simplified to Equation 3-2. Where C_{10} and C_{01} are material constants related to the distortional response and are determined experimentally.

$$W = C_{10}(I_1 - 3) + C_{01}(I_2 - 3) \qquad (3\text{-}2)$$

The Mooney-Rivlin coefficients obtained from earlier experiments and research will be used to model the HLFS tire properties [34].

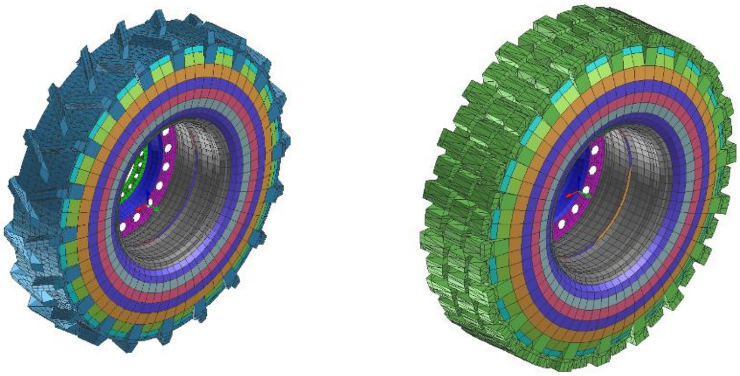

Figure 3-1: FEA model of the HLFS agricultural tire shown on the left and the Michelin Stryker shown on the right *[34]*.

3.2.2 HLFS Tire Construction

The new design is modelled according the HLFS Tire made by Barez Tires [70] and is seen in Figure 3-2. The HLFS tire has the dimensions of 220/70B16 and has a bias ply body. The tire width is 220 mm, and the outer diameter is 840 mm, the rim width is 406 mm. The tread portion is made of a total of 42 lugs. Each lug is 139 mm in length, 25 mm in width, and has a depth of 30 mm. The lug angle with the transverse y-axis is 34 degrees. The tire has a total mass of 37.2 kg.

Figure 3-2: The HLFS agricultural tire made by Barez Tires *[70]* and its model in Pam-Crash.

The HLFS tire is designed using the Visual Environment's Pam-Crash application from ESI Group. A previously modelled and validated off-road Michelin Stryker [68] tire was used as a basis for the HLFS tire design. The HLFS tire is made of 21 parts which make up the rim, tread, under tread, layered belts plies, and sidewalls.

The HLFS tire is meshed using different elements for each part. The rim is created using quad shell elements. The lugs and the under tread are created using solid hexa elements. The tread base is part of the whole tread design and is what the lugs are attached to. They are created using a Degen tetra solid elements. The tire shoulder is made from solid penta elements. The sidewall layers and plies are all created using a membrane quad element. Lastly, the beads are created using beam elements to have them act very rigid. A section cut for the HLFS tire is created using these elements and rotated to create the full tire.

The rim consists of 1 rigid part, sidewall consists of 13 parts, the layered belts and plies have 4 parts, 1 tread, 1 under tread and 1 shoulder part. The rim shown in Figure 3-3 is considered a rigid part where it does not experience any deformation when loads are applied to it. The center of the rim is considered the center of the tire and all forces are applied at the center.

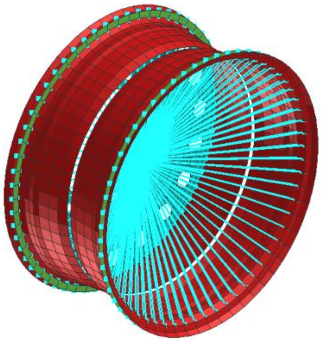

Figure 3-3: Rigid body constraint applied to the HLFS tire's rim.

Figure 3-4 shows the modelled HLFS agricultural tire, the tire is scaled as 1:1 in accordance to the dimensioned mentioned above for the actual HLFS tire. The tread is made of a Mooney Rivlin Solid and best represents the rubber material used in tractor tires. It has a mass density of 1225 kg/m^3 [68]. It also has a first Mooney-Rivlin law coefficient of 0.67, and a second Mooney-Rivlin Law coefficient of 2.46 and a Poisson’s ratio (loading) of 0.46. The Mooney-Rivlin coefficients are obtained from a previous research for off-road tires [68].

The under tread is also made of a Mooney-Rivlin Solid with mass density of 1224 kg/m^3, first and second Mooney-Rivlin law coefficients of 0.051 and 0.186, and a poison’s ratio of 0.49.

The tire sidewall is made of multiple layered membrane with one isotropic parent sheet and two fiber layers. The mass density for the whole sidewall is 1496 kg/m^3. The parent sheet has a Young's modulus of 800 MPa and a Poisson's ratio of 0.46. The first and second fiber layers have a Young Modulus and a shear modulus of 800 MPa and 1 MPa respectively.

Table 1, 2, 3, 4 shows the material properties of the FEA tire parts and layers. There are 6 layers of belt plies in the tire carcass. These correspond to a density of 1496 kg/m^3, Poisson's ratio of 0.46 and a parent sheet Young's modulus of 1 MPa. The first fiber layer has a Young's modulus of 1 MPa and a shear modulus of 600 MPa. The second fiber layer has a Young's modulus of 1 MPa and a shear modulus of 600 MPa. The beads are made of beam elements and has a density of 23,700 kg/m^3, a Poisson's ratio of 0.4, a Young's modulus of 92.31 GPa and a yield stress of 1E20 MPa.

The rim is made of a null shell material and has a mass density of 800 kg/m^3, a Young's modulus of 200 GPa and a poisons ratio of 0.3. The total mass of the tire using the mass inertia data was found to be 38 kg. This accurately represents the actual tire model's weight with a percent error of 2.1%.

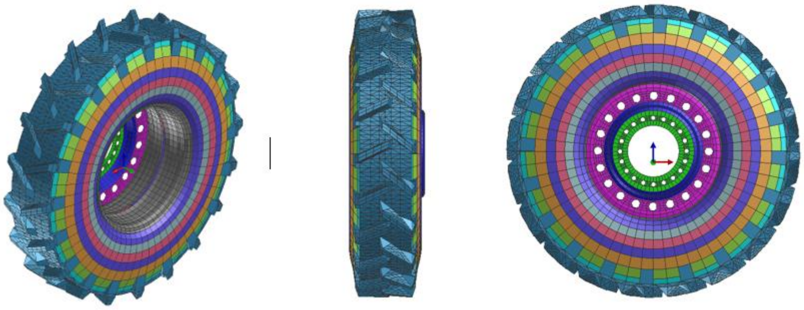

Figure 3-4: The HLFS agricultural tire and rim assembly.

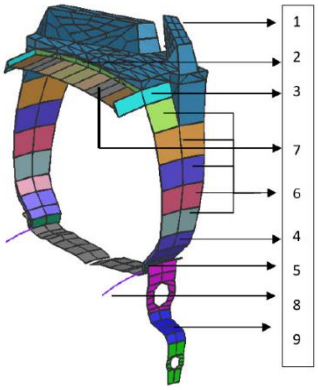

Figure 3-5: The HLFS tire section cut with numbers corresponding to Material I.D in Table 3-1 to 3-4.

Table 3-1: Material properties of the Mooney-Rivlin rubber solid elements.

Tire Component	Tread	Under Tread	Shoulder	Sidewall	Sidewall
Material I.D	1	2	3	4	5
Density (ton/mm^3)	1.39E-9	5.962E-10	1.35E-9	8.81E-10	8.82E-10
1st Mooney-Rivlin Coefficient (C10)	0.67	0.051	0.67	0.0392	0.0392
2nd Mooney-Rivlin Coefficient (C01)	2.46	0.186	2.46	0.1268	0.1268
Poisson's Ratio	0.49	0.499	0.499	0.499	0.499

Table 3-2: Material properties of the membrane elements.

Tire Component	Sidewall	Plies
Material I.D	6	7
Density (ton/mm^3)	1.65E-9	1.85E-9
Isotropic Parent Sheet Young's Modulus (MPa)	800	1
Isotropic Parent Sheet Poisson's Ratio	0.46	0.46
Layer 1 Young's Modulus (MPa)	800	1
Layer 1 Shear Modulus (MPa)	1	600
Layer 1 Angle of Fibers with R-axis	0°	0°
Layer 2 Young's Modulus (MPa)	800	1
Layer 2 Shear Modulus (MPa)	1	600
Layer 2 Angle of Fibers with R-axis	90°	90°

Table 3-3: Material properties of the beam elements.

Tire Component	Beads
Material I.D	8
Density (ton/mm^3)	2.37E-8
Young's Modulus (GPa)	92.31
Poisson's Ratio	0.4
Yield Stress (MPa)	1E20

Table 3-4: Material properties of the shell elements.

Tire Component	Rim
Material I.D	9
Density (ton/mm^3)	8E-9
Young’s Modulus (GPa)	200
Poisson’s Ratio	0.3

3.3 FEA Tire Validation

The FEA tire model is further validated against the tire characteristics provided by the manufacturer [71]. The drum-cleat test is first performed to determine the first mode of vibration of the tire that is then used to calculate the damping ratio. Later, three different tests are performed to determine the vertical, lateral, and longitudinal characteristics of the tire.

3.3.1 Validation Techniques

The Drum-Cleat test shown in Figure 3-6 is used to determine and validate the first mode of vibration of the tire. The drum-cleat consists of a drum of 2.5 m radius with a single semi-circular cleat of 15 mm radius. The tire is placed on top of the drum and it is constrained in lateral and longitudinal translation and rotation about the vertical and longitudinal axis. The tire is first inflated to the desired inflation pressure, then a constant vertical load is applied to the center of the tire and the tire is allowed to settle on the drum. Then, an angular velocity of 11.1 rad/s is applied to the center of the drum which excites the tire and allows for the calculation of the vertical first mode of vibration. The first vertical mode of vibration is found and its corresponding frequency in Hertz is obtained. This frequency is used to calculate the sidewall damping coefficient.

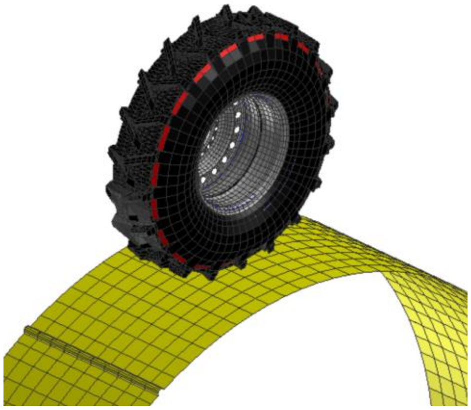

Figure 3-6: FEA tire-drum-cleat model.

The vertical force as a function of time during the simulation is extracted and the Fast Fourier Transformation (FFT) function implemented in Pam-Crash is used to transform from time domain to frequency domain. The variation of the vertical force as a function of frequency in Hz after applying the FFT is then plotted. The first peak corresponds to the frequency at which the rotation of the tire occurs, while the second peak corresponds to the frequency which represents the first mode of vibration. The sidewall damping coefficient α is then calculated using Equation (3-3). Where ω is the first mode of vibration frequency in rad/s and ζ is the critical damping which is estimated to be 5% based on literature [2].

$$\alpha = \frac{2\zeta\sqrt{KM}}{M} = 2\zeta\sqrt{\frac{K}{M}} = 2\zeta\omega \qquad (3-3)$$

The damping is added to the tire's sidewall through the application of a damping load through the structural loads application within Pam-Crash. As a result, the damping is added through a load instead of the material properties itself. There are two ways of adding damping within this application; using a nodal factor or a curve. Damping is added to the sidewall using a mass proportional nodal damping coefficient also known as the nodal factor that is calculated using Equation (3-3). The sidewall is selected for the parts to be used where nodal damping is added to the sidewall. This sidewall damping is maintained throughout the full simulation.

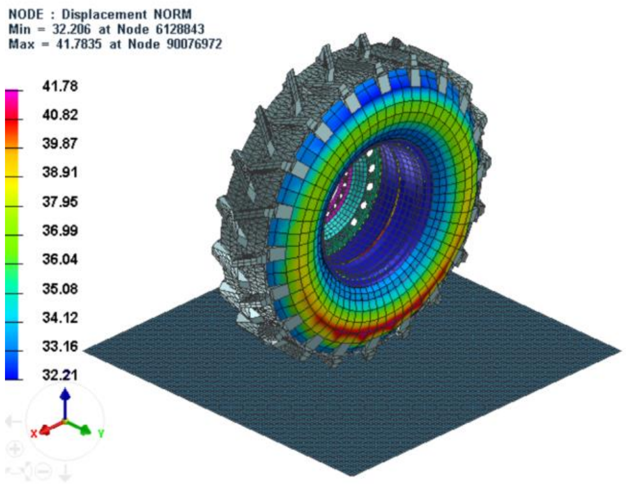

Figure 3-7: Normal displacement in tire sidewall during vertical stiffness test.

The first validation test shown in Figure 3-7 depicts the vertical deflection test performed on a hard surface. This test is used to determine the vertical stiffness of the tire when subjected to a ramp load. The HLFS tire is placed on top of a rigid road, the tire is constrained in the lateral and longitudinal translational motion and in all rotational direction. The tire is first inflated to the desired inflation pressure then a ramp load is applied to the center of the tire. The vertical force along with the vertical deflection of the tire with respect to time are extracted and plotted to determine the vertical stiffness. The slope of vertical force as a function of the vertical displacement is regarded as the vertical stiffness. Figure 3-7 shows the normal displacement in the tire sidewall elements during the vertical stiffness test, it is noticed that the lower part of the sidewall which is closest to the contact surface has the highest displacement value recorded to be 41.8 mm.

The lateral stiffness test is then performed to determine the lateral stiffness of the HLFS tire at a vertical load of 5895 N, lateral load of 400 N, and an inflation pressure of 193 kPa. The tire is first inflated to 193 kPa, and then a constant vertical load of 5895 N is applied to the center of the tire. Once the tire is stable on the ground, a lateral load of 400 N is applied to the center of the tire until a steady state lateral displacement is achieved. Then, the lateral load is removed, and the tire is allowed to oscillate in lateral direction until steady state is achieved again. The initial steady state displacement obtained from the simulations is used in Equation (3-4) to determine the lateral tire stiffness. Where the lateral force is that applied to the center of the tire and is equal to 400 N.

$$k_l = \frac{Lateral\ Force}{lateral\ Drisplacement}\left(\frac{N}{mm}\right) \qquad (3-4)$$

The longitudinal test is then used to determine the longitudinal stiffness of the tire. The tire is first inflated to 193 kPa, then a constant vertical load of 5898 N is applied to the center of the tire. Upon contact, a longitudinal force of 1500 N is applied to the tire's center of gravity. The load is held until steady state longitudinal displacement is achieved and released enabling the tire to reach initial steady state conditions once again. The longitudinal force along with the translational and rotational velocities are extracted from the simulation. The slip is then calculated using Equation 3-5, and the longitudinal force as a function of slip (%) is plotted. The slope of the longitudinal force versus slip at approximately 0 % slip is regarded as the longitudinal tire stiffness as shown in Equation 3-6.

$$Longitudinal\ \%\ slip_{|traction} = \left(1 - \frac{v}{r * \omega}\right) * 100\% \qquad (3-5)$$

$$k_{k,soil} = \frac{\partial\ Longitudinal\ Force}{\partial Slip\%}\ |\ Slip = 0 \quad \left(\frac{N}{Unit\ slip}\right) \quad (3-6)$$

In order to calculate the longitudinal tread stiffness k_{cx}, the longitudinal tire stiffness, k_k is divided by half the projected contact length a, as shown in Equation 3-7. The projected contact length a corresponds to the length of the HLFS tire which is in contact with the ground.

$$k_{cx,soil} = \frac{k_{k,soil}}{a} \quad \left(\frac{N}{mm}\right) \qquad (3-7)$$

3.3.3 Validation Results

The drum-cleat test was first performed with a preliminary damping coefficient based on previous research. The vertical force as a function of time is extracted from the simulation and the FFT filter employed within Pam-Crash was used to determine the vertical force as a function of frequency as shown in Figure 3-8. The first mode of vibration for the HLFS tire was found to be at a frequency of 82 Hz, which is within the acceptable range for agricultural tires. Based on the estimated frequency the sidewall damping coefficient was then calculated to be 51.5.

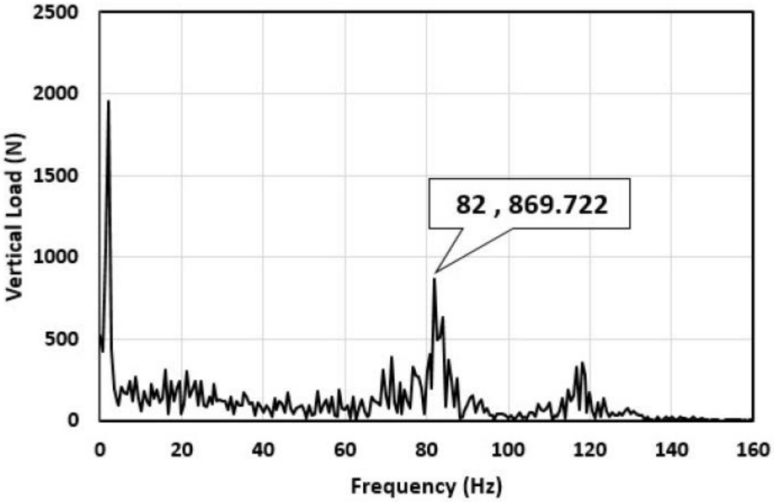

Figure 3-8: First mode of vibration at 5.55 rad/s speed, 10,000 N load, 193 kPa inflation pressure.

Table 3-5 shows the damping coefficient at several operating conditions. From Table 3- 5, it shows that there is an increase in damping coefficient as the inflation pressure increased at a drum cleat's rotational speed of 5.55 rad/s and a vertical load of 10,000 N. This is because the frequency at which the first mode of vibration occurs, increases as the inflation pressure of the tire increases. For a drum cleat with a rotational speed of 11.1 rad/s, the damping coefficients do not vary much with the change of inflation pressure. Under inflation and over inflation both require damping coefficients similar to operating inflation pressure. This means at higher speeds the tire is not sensitive to changes in inflation pressure in regards to the damping coefficients used for the simulations.

Table 3-5: Damping Coefficients as in terms of inflation pressure and cleat rotational speed

Inflation Pressure (kPa)	Damping Coefficient at 5.55 rad/s Rotational Speed	Damping Coefficients at 11.1 rad/s Rotational Speed
103	28.5	52.3
193	51.5	51.5
275	58	52.8

The vertical force as a function of the vertical deflection for both measurement and simulation at 103 kPa inflation pressure is shown in Figure 3-9. The slope of the vertical force versus vertical deflection represent the vertical stiffness, k_{tot}. It is recorded that the measured and simulated vertical stiffness are 250 N/mm and 422 N/mm, respectively. Furthermore, it is observed that for a small deflection of less than 6 mm both simulations and measurements are in good agreement and have almost the same behavior. For a deflection greater than 6 mm or a force greater than 2 kN the simulation and predicted values are different, and the simulation adhere a non-linear behavior.

It should be noted that generally the agricultural tires operate at low vertical loads generally less than 3 kN. Thus, the FEA tire model is considered to have a good behavior at normal operating conditions and requires further investigation at higher operating loads.

Furthermore, the vertical stiffness increases as the inflation pressure increases past 193 kPa (28 psi) or at the operating inflation pressure for the tire. The underinflated tire shows increased stiffness as well. The simulated vertical stiffness at 103, 193, 275 kPa (15, 28 and 40 psi) gave stiffness of 525.92, 422.14 and 448.13 kN/m, respectively. The results show that for both over inflation 275 kPa (40 psi) and under inflation 103 kPa (15 psi) the tire gets stiffer where more stiffness is seen in over inflation. The underinflated tire shows similar stiffness for a range of 6 mm deflection when compared to both the 193 kPa (28 psi) and 275 kPa (40 psi) tires. As the vertical force is increased past 3000 N and the tire has passed 6 mm deflection, the tire inhibits very stiff characteristics as the tire cannot compress vertically as easily. The vertical force will need to be increased a lot to deflect the side rubber of the tire. Research has indicated that rubber in tires show non linearity in vertical stiffness after a certain range. As a result, more research needs to be conducted in order to learn about this non-linearity. This sidewall rubber is very tough as the real-life tire exhibits these characteristics as well.

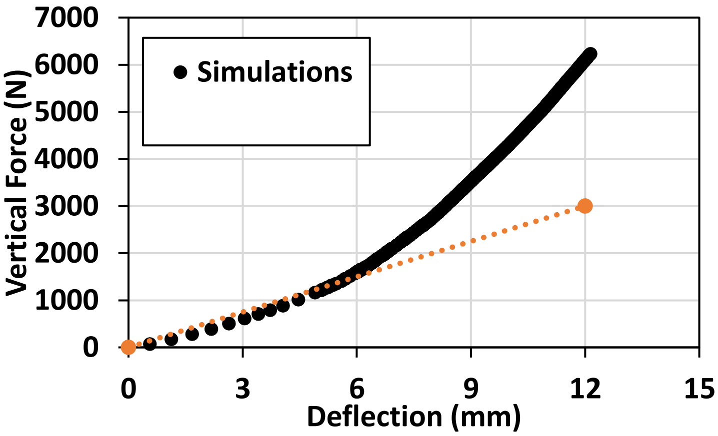

Figure 3-9: Vertical force as a function of vertical deflection for simulation and measurement tests.

Figure 3-10 shows the variation of the lateral displacement as a function of time at 400 N lateral force and 193 kPa inflation pressure. The computed lateral stiffness, $\boldsymbol{k_l}$ is 288 N/mm while the measured on is 305 N/mm. Thus, the error is around 5% which shows good agreement between the simulation and measurement results.

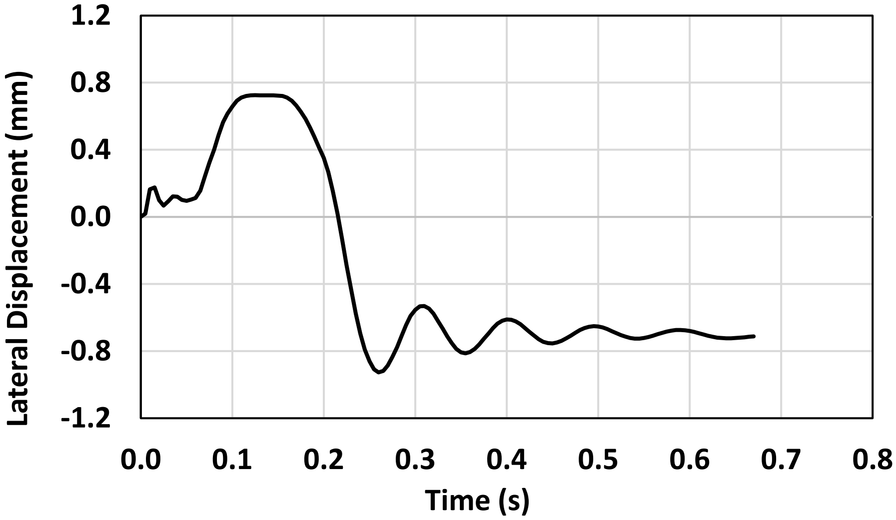

Figure 3-10: Lateral displacement as a function of time for the lateral stiffness test at 400 N force.

Figure 3-11 shows the variation of the longitudinal displacement as a function of the time at 1500 N longitudinal force and 193 kPa inflation pressure during the longitudinal stiffness simulation. The longitudinal stiffness, k_{cx} is computed to be 300 N/mm while the measured one is 302 N/mm. Thus, the error is calculated to be around 1%. Therefore, the simulated and measurement results are in good agreement.

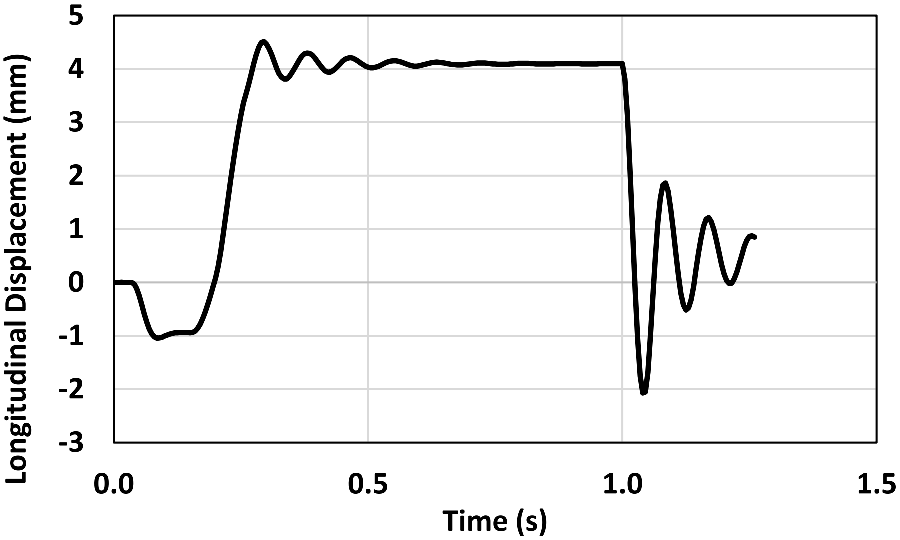

Figure 3-11: Longitudinal displacement as a function of time for tangential simulation.

Figure 3-12 shows the displacement in the longitudinal direction on the FEA tire at 1500 N longitudinal load and 193 kPa inflation pressure. The highest recorded displacement is around 9.5 mm at the front side of the tread and the lowest recorded displacement is around zero mm at the sidewall of the tire. It is also noticed since the rim is constrained and is considered as a rigid body; thus, it has no displacement as well.

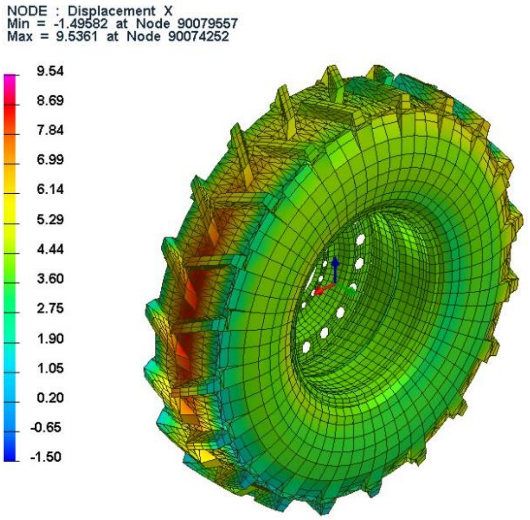

Figure 3-12: Longitudinal displacement on the tire at 1500 N and 193 kPa inflation pressure.

3.4 Chapter Summary

An FEA tire model of an agricultural tire size 220/70B16 was developed using Pam-Crash virtual environment. The FEA tire model consists of total of 42 lugs that were modelled using Mooney-Rivlin material. The modelled tire has 21 parts which make up the rim, tread, under tread, layered belts plies, and sidewalls. The rim was modelled as a rigid non-deformable body.

The tire was validated in static and dynamic response using the drum-cleat, vertical stiffness, lateral stiffness and longitudinal stiffness tests using measurement results provided by manufacturer. The first mode of vibration was computed to be around 82 Hz which falls in the normal range of agricultural tires. It was concluded that the FEA tire has a good representation of the physical tire in lateral and longitudinal characteristics. Furthermore, the FEA tire has a good presentation of the vertical behavior at low vertical loads which is in the normal operating conditions.

CHAPTER 4 - SOIL MODELLING AND VALIDATION

This chapter presents the modelling, calibration and sensitivity analysis of LETE sand and Clayey Loam using Visual Environment's Pam Crash. Soil is modelled and converted from Finite Element Analysis mesh (FEA) to Smoothed-Particle Hydrodynamics (SPH). The sand and soil are then calibrated using terramechanics published data by simulating a pressure sinkage test and direct shear box test using the SPH particles. The material properties such as tangent modulus, yield strength and bulk modulus are configured so the simulation's results match those of theoretical values. Sensitivity analysis of the calibrated LETE sand material is then investigated. The sensitivity analysis includes mesh size, plate geometry, smoothing length, max smoothing length, artificial viscosity and contact thickness. The effect of these parameters on the sand behavior is analyzed. The results found within this chapter will be further used to study understand the tire-terrain interaction.

4.1 Introduction

This chapter presents a new Clayey loam soil and LETE sand model using Smoothed-Particle Hydrodynamic (SPH) Technique. The two off-road terrains are modelled using SPH technique and hydrodynamic elastic-plastic material and calibrated using pressure-sinkage and shear-strength tests against published terramechanics value [72]. The simulations were conducted using Visual Environment's Pam Crash software. The ability to model the terrain using the SPH technique is very advantageous in tire-soil simulations simplicity for complex geometries and particle simulations. The SPH technique tracks the particle mass as Lagrangian formulations and has been a developing rapidly as it shows versatility for diverse problems. Using a finite element method, the software allows modelling of complex geometry by offering continuum beam, shell, membranes and solid elements. Hence it is very useful for the modelling and simulations of tire-soil interactions.

4.2 SPH Terrain Calibration Technique

In order to calibrate LETE sand, it is necessary to create two tests as described by Wong as the pressure sinkage and shear strength test [72]. The simulation of these test in Pam crash will be compared to published data and calibrated accordingly.

4.2.1 Pressure Sinkage Test

The pressure-sinkage test shown in Figure 4-1 is implemented by modelling LETE Sand and Clayey Loam particles within 800mm x 800mm x 800mm boxes separately. A circular plate of 150mm radius is used to apply pressures of 0, 10, 50, 100, 150 and 200 kPa on the two terrains for 0.4 seconds. The plate sinkage is computed for six different pressures at steady state. A plot of plate sinkage (dependent variable) as a function of applied pressure (independent variable) is obtained from the output file. The line of best fit for the plot is then compared to the line of best fit for theoretical data. Theoretical plate sinkage data is obtained by rearranging Bekker's relation [35] for plate sinkage as in Equation 4-1 and Equation 4-2.

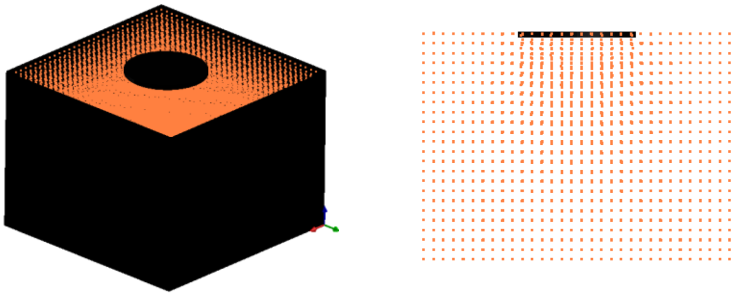

Figure 4-1: Pressure-sinkage test for one pressure plate using LETE Sand.

$$p = \left(\frac{k_c}{b} + k_\theta\right) z^n \qquad (4\text{-}1)$$

$$z = \left(\frac{p}{\frac{k_c}{b}+k_\theta}\right)^{\frac{1}{n}} \qquad (4\text{-}2)$$

Where p is the applied pressure (kPa), b is the radius of the circular plate (mm), z is the plate sinkage (mm), k_c, k_θ and n are terrain values obtained from terramechanics.

Several material parameters are calibrated to achieve the best fitting which best represents the LETE sand's behavior obtained from terramechanics. Within Pam-Crash's material cards, LETE sand was initially modelled as loose sand using previous publication [47]. The density and the shear modulus were kept constant throughout the simulations, while the bulk modulus, yield stress and tangent modulus were calibrated one at a time via trial and error method to obtain LETE sand.

4.2.2 Shear Strength Test

The shear box test is simulated using the same LETE Sand and Clayey Loam SPH material. There are three parts for the shear box; a top plate, a sliding top half of a box and a static bottom half of a box as seen in Figure 5. The dimensions of the box are 400 x 200 x 240 mm and is filled with the corresponding terrain particles. Six top plates apply pressure to six different boxes filled with the SPH particles while the top half of the boxes are dragged in one direction. Each plate has a 50 kPa increment of pressure applied ranging from 0 to 200 kPa. The output consists of a section force against time for each of the different pressures. Finally, the shear strength is found by dividing the section force by the cross-sectional area of contact between the plate and soil particles which is calculated to be 0.15024 m^2. A plot of the shear strength as a function of pressure is obtained and compared to the results obtained from Mohr-Coulomb failure criteria.

The theoretical max shear strength for the terrain are calculated using Equation 4-3 and Equation 4-4:

$$\tau = \tau_{max}\left(1 - e^{-\frac{j}{k}}\right) \qquad (4\text{-}3)$$

$$= (c + \sigma tan\theta)\left(1 - e^{-\frac{j}{k}}\right)$$

$$\tau_{max} = c + p\ tan\ \theta \qquad (4\text{-}4)$$

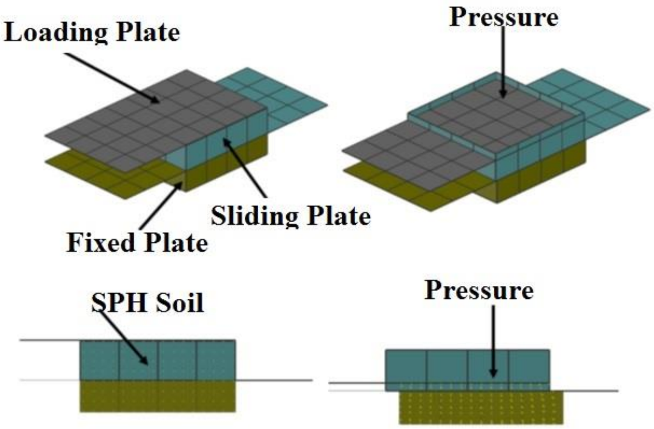

Figure 4-2: Shear box test for one pressure using LETE Sand [52].

In equations 4-3 and 4-4, τ is the shear stress (kPa), j is the shear displacement (mm), c is the cohesion (kPa), θ is the angle of internal shearing resistance of the terrain (rad) and k is the shear deformation modulus (kPa).

The LETE sand cohesion and shear resistance angles are obtained from terramechanics published results [72], and then compared to the simulation results. Now, similar to the pressure sinkage test, a shear box test is simulated for different parameters within the SPH materials card. Single parameters such as the bulk modulus, tangent modulus and yield strength of the materials were calibrated and the of best fit of these simulated were obtained.

4.3 Terrain Calibration Results

To calibrate the LETE sand and Clayey Loam soil parameters, the material parameters of loose sand from previous published calibration paper was used [47]. A mass density of 1.44 E-09 ton/mm^3, and a shear modulus of 7 MPa has been used for all of LETE sand and Clayey loam calibrations. Furthermore, a plot of the plate sinkage and shear strength has been obtained using a loose sand material with tangent modulus of 0.25 MPa, a yield strength of 0.004 MPa and a bulk modulus of 2.5 MPa. It was observed that plate sinkage amounted to 157 mm for 200 kPa pressure. The theoretical value for LETE sand's plate-sinkage is to be around 15.79 mm. As a result, LETE sand is considered to be a lot harder than loose sand and needed further calibration. After trial and error, the parameters in Table 4-1 were obtained and best described LETE sand and Clayey Loam's theoretical plate-sinkage and shear strength.

Table 4-1: Material card parameters for Clayey Loam and LETE Sand *[73]*.

Material Type	E_t (MPa)	C_1 (MPa)	G (MPa)	σ (MPa)	ρ (ton/mm^3)
Clayey Loam	0.25	2.5	7	0.02	1.44E-9
LETE Sand	0.35	17	7	0.09	1.44E-9

Figure 4-3 shows that the parameters used within the material card show an accurate representation of LETE sand and are similar to theoretical values. The line of best fit for the measured and simulated data for plate displacement show a percent error of 4.69%.

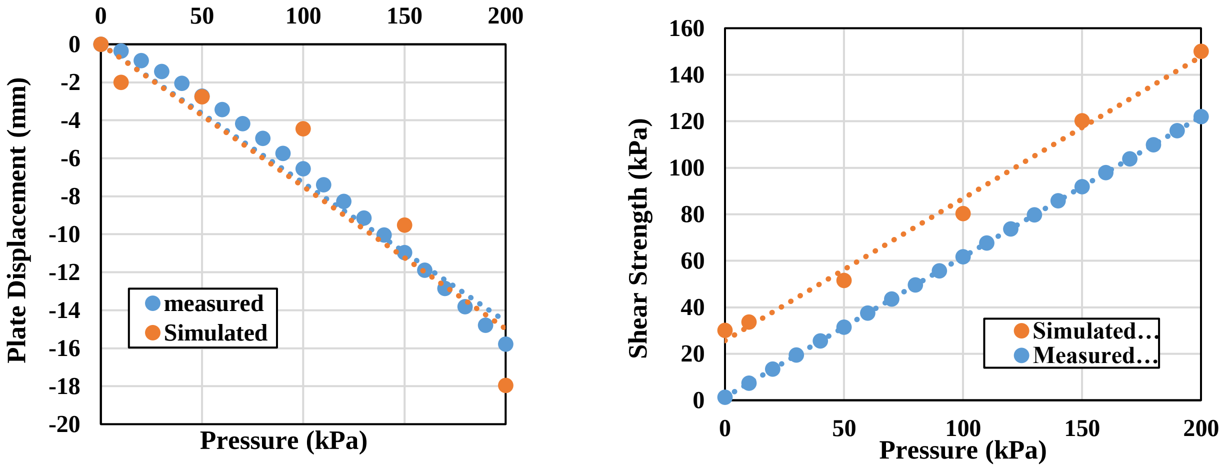

Figure 4-3:Plate displacement and shear strength as a function of pressure for measured and simulated LETE Sand pressure sinkage and shear box test.

Figure 4-3 shows that the line of best fit for theoretical and simulated data for shear strength are also very similar. The y-intercept or the cohesion of the sand is increased to 25.65 kPa for the simulated data. The slope of the shear strength as a function of pressure graphs represents the angle of internal shearing resistance. For calibration purposes, the angle of internal shearing resistance must be similar for the LETE sand's measured and simulated results. Since the slope for both simulated and measured data in Figure 4-3 are similar, LETE sand's shear behavior is therefore calibrated.

The material properties used to model clayey loam soil are shown in Table 4-1. According to the graph shown in Figure 4-4 the Clayey Loam soil sinkage at pressure of 80 kPa for experimental test, Bekker model and simulation method is around 48, 49 and 42 mm, respectively. It shows the pressure and sinkage relationships obtained with the SPH technique are in good agreement with the experimental data and Bekker's model.

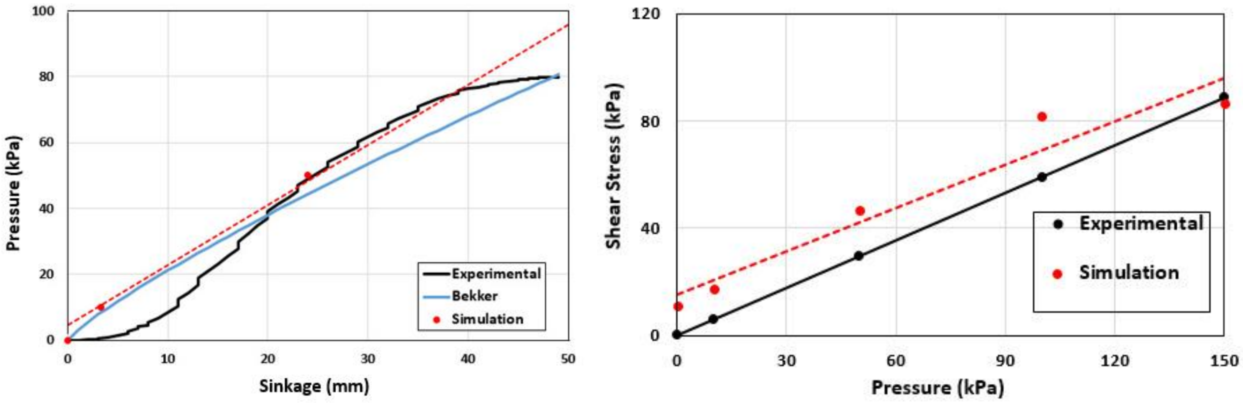

Figure 4-4: Comparison of Clayey Loam soil pressure sinkage and shear stress values in simulation and experimental data [71].

Figure 4-4 also shows the shear strength to pressure relationship for clayey loam soil for both simulation and experimental data. The slope of the graph for experimental and simulated data is similar, which indicates the angle of internal shearing resistance of soil, is 30.51 degree for experimental data and 28.42 degree for simulated data. Since the internal friction angle of soil is an important parameter to calibrate the soil, the calibrated method is appropriate for the soil shear behavior.

4.4 SPH Sensitivity Analysis

Now that SPH LETE sand has been modelled and calibrated, further investigation is done in regards to changing the part card parameters and mesh size. The original mesh size and part card parameters used for the calibration of LETE sand is shown in Table 4-2. Next the sensitivity analysis was conducted by changing each of these parameters in Table 4-2. The mesh size will be varied to see it’s effect on the plate’s vertical displacement, shear strength and cohesion. Similarly, the particle smoothening length to radius ratio, maximum smoothing length, M-G artificial viscosity and the anti-crossing force parameter is changed in order to analyze its sensitivity on the plate displacement, shear strength and cohesion.

Table 4-2: LETE Sand part card parameters.

Mesh Size	25 mm
Particle "Smoothening Length to Radius" ratio	1.2
Maximum Smoothing Length	100
Alphamg: First Parameter for the M-G art Viscosity	0
ETA: Anti-crossing Force parameter	0.1

4.4.1 Mesh Configuration

The mesh size used in FEA analysis depends on the geometry of the part and its complexity. LETE Sand particles undergo high deformation and endure different forces during compaction from the tire. The mesh size was varied within this section (10 mm, 25 mm, 50 mm, 75 mm) and its effect on the place displacement and shear box test was analyzed. The computation time for solving these simulations have a strong correlation to the mesh size used within the PC (Pam Crash) file. As a result, larger size meshes were created first as it took the least time.

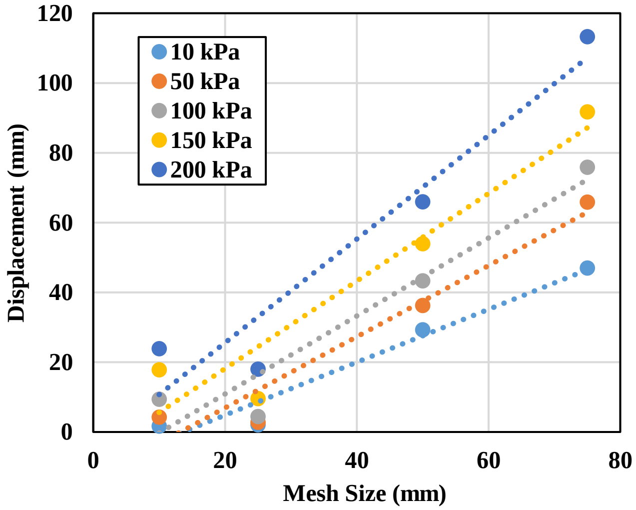

Figure 4-5: LETE sand displacement as a function of mesh size for different pressures.

Figure 4-5 shows that the LETE sand becomes less dense and therefore sinks a large amount at higher pressures for larger mesh sizes. The sand particles were calibrated for a 25 mm mesh size. The results also show that for a mesh size of 10 mm, the displacements are even larger compared to a mesh size of 25 mm. This shows that using smaller than 25 mm mesh size shows inaccuracy in plate displacement. There are less particles interacting with each other and therefore less resistive forces. However, increasing the mesh size further to 50 mm and 75 mm also shows a linear increase in plate displacement. Generally, increasing the mesh size results in more displacement of the soil.

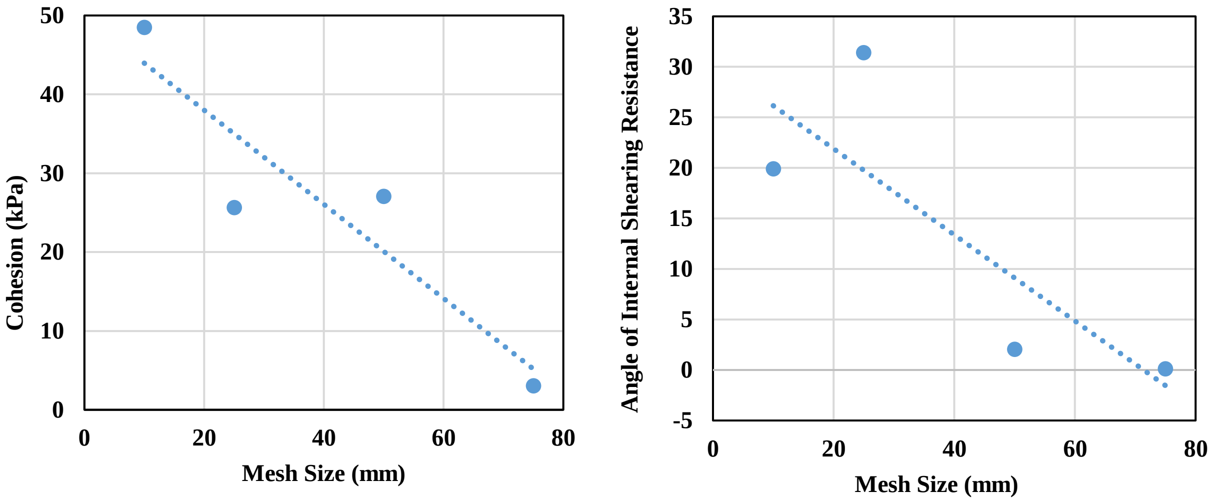

Figure 4-6: LETE sand cohesion and angle of internal shearing resistance as a function of mesh size (10mm, 25 mm, 50 mm, 75mm).

When decreasing the mesh size to 10 mm, the displacement for lower pressures accurately represent those of 25 mm mesh. However, at higher pressures, the 10 mm mesh size shows more displacement. This means that there is more interaction between the sand particles and compaction leading to a higher displacement. Increasing the mesh size to 50 and 75 mm shows higher displacements for all six pressures applied. Having larger mesh size represents less particles and less interaction between particles. When subjected to a certain load, the particles of higher mesh size displace more extensively due to less resistance between the particles.

As the mesh size increased, the cohesion for the LETE sand particles generally decreased as shown in Figure 4-6. The cohesion is the togetherness or solidarity of the sand particles when exposed to 0 kPa pressure. This decrease in cohesion is due to less particles which allow enhanced shearing. There are less repulsive forces and less internal energy within the sand particles and therefore are less cohesive and do not stick to each other.

The angle of shearing resistance is also decreased whether the mesh size is increased (to 50 and 75mm) or decreased (to 10mm) as shown in Figure 4-6. This results in inaccurate modelling of LETE sand as the mesh size is changed. As a result, if using different mesh size, further calibration is needed in order to accurately represent LETE Sand. When performing these tests, the computational time for a 10 mm mesh was very high (5.315 E 05 seconds or approximately 6 days). It was therefore simulated first. The reduction in mesh size is not useful for our purpose as it took longer and needed further calibration for higher pressures.

4.4.2 Smoothing Length

Next, the smoothing lengths to radius ratio was increased from 1.2 to 1.5 and then to 2.1. This means that the domain of influence between the particles are increased and there will be less interactions between them. The results for the tests are shown in Figures 4-7 to 4-9.

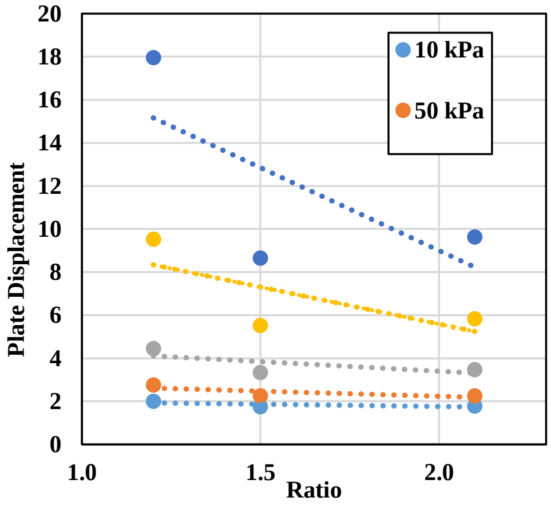

Figure 4-7: Plate displacement as a function of smoothing length to radius ratio (1.2, 1.5, and 2.1).

Increasing the particles smoothing length to radius ratio has made the particle seem more resistant to displacement at higher pressures. It makes the LETE sand particles behave like harder material. It can be seen from Figure 4-7 and Figure 4-4 that the displacement is a lot less than our calibrated LETE sand (Figure 4-4). This is because the particle interacts with a lot more adjacent particles as the smoothing length increases. The increased particles interactions prevent the LETE sand from sinking. Increasing the smooth length to radius ratio shows a larger decrease in plate displacement for large pressures. At low pressures, changing the ratio has minimal effect on place displacement.

The cohesion is increased within the LETE sand particles as the ratio is increased. This is reasonable since the particles domain of influence is increased. This results in higher attraction forces between the particles and displaces more as the pressure is increased as seen from Figure 4-8.

Figure 4-8 also shows the decrease in angle of internal shearing resistance when the particles smoothing length to radius ratio is increased. When the angle of internal shearing resistance is decreased, the particles max shear strength at corresponding pressures is also decreased. As a result, it's resistance to shearing is decreased. The particle's larger domain of influence on other particles prevents the shearing. This can also be explained by the higher displacement changes for higher pressures as shown in Figure 4-7.

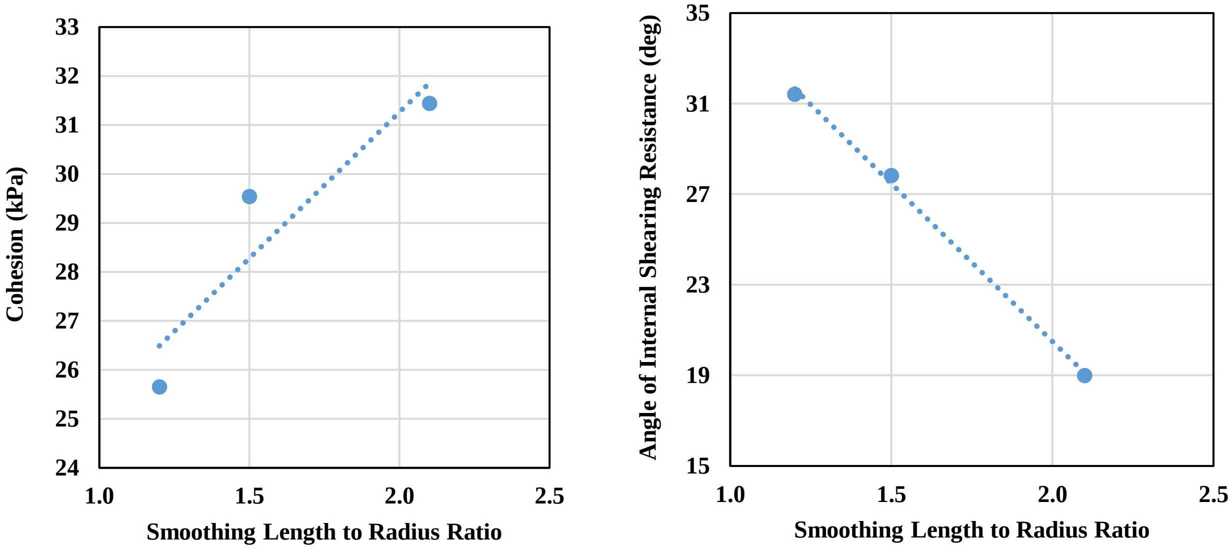

Figure 4-8: Cohesion and angle of internal shearing resistance as a function of smoothing length to radius ratio.

Since the particle is experiencing higher vertical pressures, it is more susceptible to vertical displacement in comparison to shear displacement. Since the characteristics of the LETE sand particles change as the smoothing length to radius ratio is increased, further calibration is needed in order to provide accurate representation of LETE Sand.

4.4.4 Maximum Smoothing Length

Another parameter used for the sensitivity analysis is the max smoothing length. The max smoothing length is decreased from 100mm to 50mm and further to 30mm and its results are shown in Figures 4-9 to 4-10.

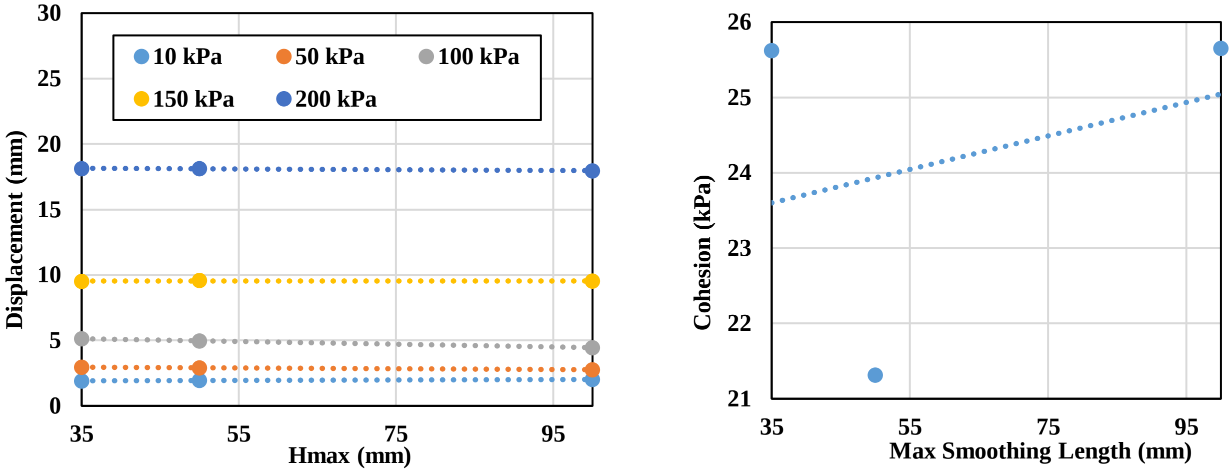

Figure 4-9: Displacement and cohesion for LETE sand as a function of max smoothing length.

Decreasing the max smoothing length shows very small change in displacements for the six corresponding pressures as shown in Figure 4-9. This means that the particles smaller domain of influence is not affected when pressures are applied. If further testing is required using a lower max smoothing length, the results will be similar and further calibration is not needed.

The cohesion is also generally decreased as the smoothing length is decreased. A maximum decrease is shown when the max smoothing length is decreased to 50. Furthermore, as the max smoothing length is decreased further to 35, the cohesion increases and is similar to that of 100 max smoothing length.

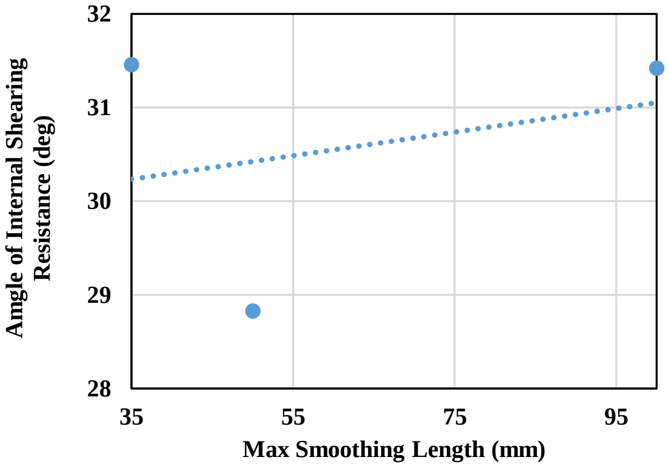

Figure 4-10: Angle of internal shearing resistance as a function of max smoothing length for LETE sand.

The angle of internal shearing resistance graph shown in Figure 4-10 also shows a similar relationship to the cohesion graph shown in Figure 4-9. Angle of internal sheering resistance is decreased to a maximum for a max smoothing length of 50 and then increased for a max smoothing length of 35. Therefore, the LETE sand particles can be modelled using a max smoothing length of 35 as the results are very similar to those of 100 smoothing length. On the contrary, further calibration is needed for a max smoothing length of 50.

4.4.5 Monaghan-Gingold Artificial Viscosity

The Monaghan-Gingold's artificial viscosity parameter alphamg was also changed and its sensitivity analysis is conducted as shown in Figures 4-14 to 4-17.

Figure 4-11 shows the plate displacement as a function of alphamg for six different pressures. The results show that as the artificial viscosity parameter is increased, the plate displacement decreased at higher pressures. Viscosity is a measure of the mediums resistivity to flow. As a result, when an artificial viscosity is added, the displacement also decreased. The highest decrease in displacement is shown for pressure of 150 kPa and 200 kPa.

Since tire-soil interaction deal with relatively higher pressures, it is not accurate to change the viscosity parameter as it does not represent LETE sand's calibrated results. The sand particles may need to be denser in order for the particles to displace as much as the calibrated results. This is not acceptable as we need a similar slope to accurately represent LETE Sand. Furthermore, increasing the viscosity has also ensured that the particles achieve steady state at an earlier time step. This is noticed even in the lower pressures. This could be useful when analyzing simulations where smaller pressures are needed.

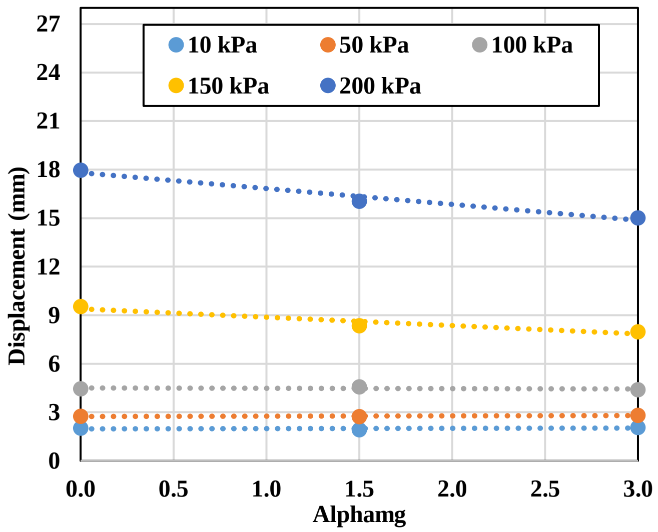

Figure 4-11: Displacement as a function of alphamg viscosity parameter for LETE sand.

As alphamg is increased to 1.5, Figure 4-12 shows that the cohesion is increased slightly. As it is increased to 3, the cohesion drops significantly. Therefore, the simulation results are not accurate for an alphamg of 3. The LETE sand is generally less cohesive as the viscosity is increased. If a higher viscosity is to be used, further calibration of the LETE sand is needed. This can be obtained by increasing the max smoothing length or the max smoothing length to radius ratio.

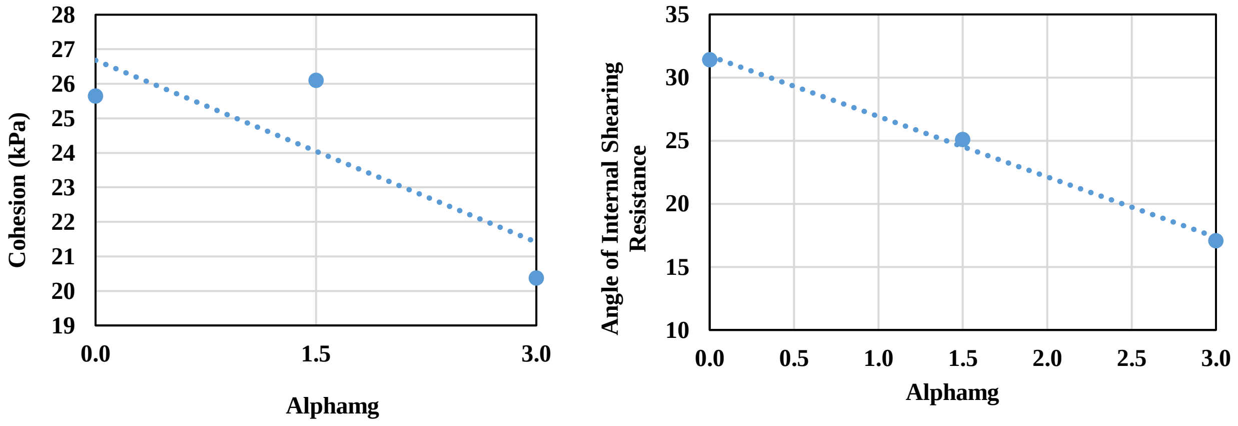

Figure 4-12: Cohesion and angle of internal shearing resistance as a function of alphamg viscosity parameter for LETE sand at 0 kPa normal pressure.

The increase in alphamg shows an almost perfect linear trend for the angle of internal shearing resistance as the line of best fit in Figure 4-12 goes through all the data points. As the viscosity parameter is increased, the angle of shearing resistance decreases. Similarly, the LETE sand is not accurately portrayed as the viscosity increases.

4.4.6 Contact Thickness

The results shown in Figure 4-13 to Figure 4-14 show the change in plate displacement and cohesion as the contact thickness for the LETE sand particle are changed to 2, 5 and 7 mm.

Figure 4-13 shows that as the contact thickness is increased, the plate displacement is generally decreased an equal amount. The increase in the contact thickness results in an increase in the contact area between the plate and SPH soil, thus leading to more soil to be considered as part of the contact. The increase in the number of SPH particles in contact with the plate results in more resistance and thus less sinkage.

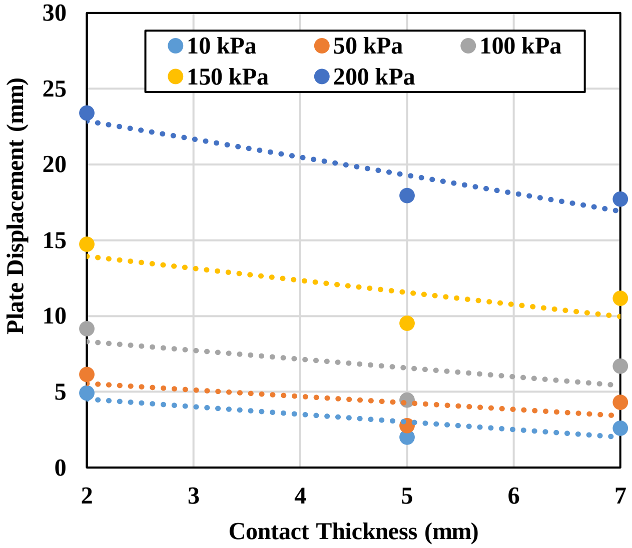

Figure 4-13: Displacement as a function of contact thickness for six different pressures.

The relationship between the angle of internal shearing resistance and the contact thickness is opposite of that shown for the cohesion as a function of contact thickness. That is as the contact thickness is decreased or increased, the angle of shearing resistance has decreased.

Figure 4-14 represents the general increase in cohesion as the contact thickness is increased. Originally the contact thickness was set to 5 mm. Both decreasing to 2 mm and increasing to 7 mm have increased the cohesion of the LETE sand particles. Therefore, the particles need to be calibrated further if a contact thickness of 2 mm or 7 mm is used.

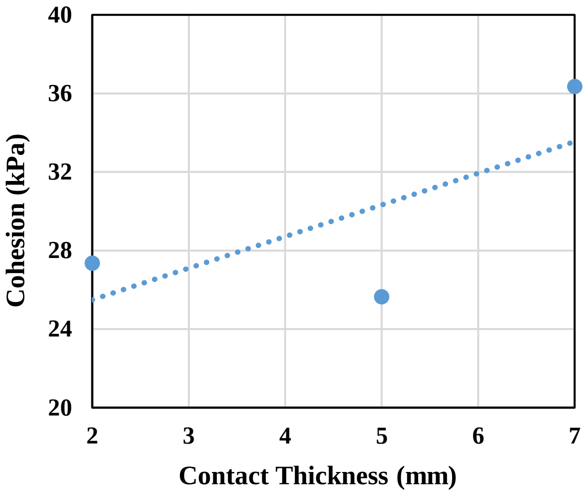

Figure 4-14: Cohesion as a function of contact thickness for 0 kPa normal pressure.

4.4.7 Square Pressure Plate

The last sensitivity analysis is conducted by using a square pressure plate instead of the circular plate used for the calibrated LETE sand particles. A square plate of 300 mm x 300 mm dimensions was used. This is corresponded to the 300 mm diameter circular plate used. The graph showing the plate displacement for the six different pressures for the square and circular plates are shown in Figure 4-16. This graph shows that using a square plate in the pressure sinkage test produces larger displacements within the LETE sand particles. The slope of the line of best fit for both the circular and square plates are very similar therefore the relationship is still the same. The larger displacements are caused due to a larger plate area in contact with the sand particles. With the square plate, the sand particles are more cohesive and need higher pressures to displace the same amount. At pressures from 0 kPa to 150 kPa the change in plate displacement is constant between the square and circular plate. However, at a pressure of 200 kPa there is not much difference between the square and circular plate.

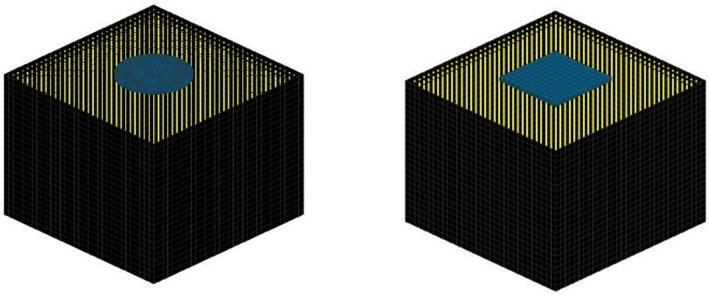

Figure 4-15: Square and circular plate displacement test for 200 kPa normal pressure.

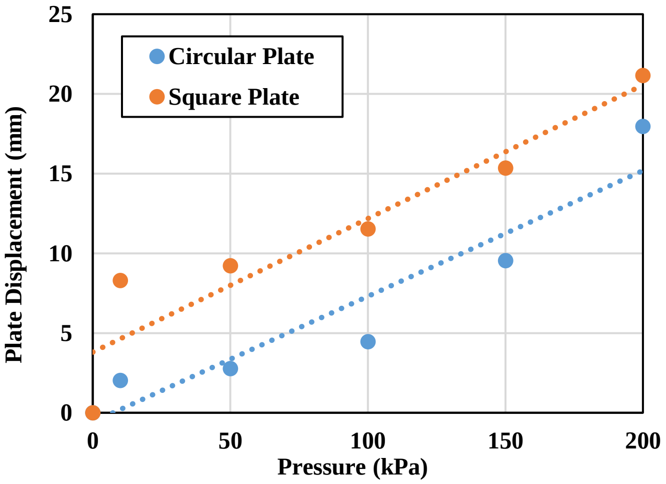

Figure 4-16: Plate displacement as a function of applied pressure for a circular and square plate.

In order to use a square plate during simulations, the part card parameters for the LETE sand must be changed and the terrain must be calibrated again. However, the trend for the plate displacement resembles very well to that of the circular plate. Further research should be done and experimental data for a square plate must be conducted in order to see if simulation results are accurate.

4.5 Chapter Summary

The modelling and calibration of LETE sand and Clayey Loam soil was conducted. The physical experiment were only available for the Clayey Loam soil model conducted in Urmia University by Azar et al. in Iran [74]. The sand and soil particles were modelled using a Smoothed-Particle Hydrodynamic technique. A pressure sinkage test and shear strength test was simulated in order to calibrate them to theoretical data and for clayey loam experimental data as well. The simulations result for both LETE sand and Clayey Loam were in good agreement with Bekker's Semi-empirical model and physical experiments.

A sensitivity analysis of different part card parameters is analyzed and their results are shown. The parameters included are the mesh size for SPH particles, the smoothing length, the smoothing length to particle radius ratio, Monaghan-Gingold's first artificial viscosity parameter, contact thickness and lastly using a square plate in the pressure sinkage test. Increasing the mesh size resulted in greater plate displacements within the soil, less cohesion and smaller angle of internal shearing resistance. Increasing the smoothing length to radius ratio showed a decrease in plate displacement for pressures of 150 kPa and 200 kPa. At lower pressure there wasn't a significant change. The cohesion increased and the angle of internal shearing resistance decreased as the smoothing length to radius ratio was increased. As the maximum smoothing length was increased from 35 mm to 50 mm and 100 mm, the plate displacement were constant for each pressure applied to the plate. The cohesion and the angle of internal shearing resistance were highest for maximum smoothing lengths of 35 mm and 100 mm and lowest for 50 mm. Furthermore, as the Alphamg artificial viscosity parameter was increased, the plate displacement decreased linearly at higher pressures. At lower pressures, the change in plate displacement was minimal. The cohesion and angle of internal shearing resistance decreased as the Alphamg parameter was increased. The contact thickness between the LETE sand and circular plate was increased and showed a decrease in plate displacement. The cohesion generally increased as the contact thickness increased. Lastly, a square plate was used for the simulations. The results showed a higher plate displacement using a square plate as compared to a circular plate.

CHAPTER 5 – ANALYSIS OF SOIL DYNAMICS

1.1 Chapter Introduction

This chapter includes the analysis of stress distribution for the HLFS tire running over Clayey Loam soil and LETE sand using the previous FEA-SPH techniques presented in earlier chapters. The study of stress distribution within soils is necessary for many agricultural and off-road applications. The forces applied to the agricultural terrain effect the quality and quantity of crop production [74]. The compaction of the soil due to excessive vehicle traffic also negatively impacts the number of soil pores and the prevention of water to those pores. This can result to runoff and kill tree roots. In this chapter the study of stress distribution as a function of different soil depth and wheel velocity is conducted using Finite Element Analysis and dynamic simulation of the HLFS tire on Clayey Loam and LETE sand terrain. Experimental data conducted in Urmia University in Iran is available for the stress distribution of the HLFS tire on Clayey Loam with a vehicle speed of 1 m/s and soil depth of 200 mm. Furthermore, the stress distribution for Clayey Loam and LETE sand at different soil depth (100 mm, 200 mm, 300mm, 400mm) and tire speed of (0.5 m/s, 1.0 m/s and 1.5 m/s) are conducted using Finite Element Method.

5.2 Methodology

The stress distribution for Clayey Loam and LETE Sand is obtained using a fully constrained rigid box with dimensions of 400 mm x 200 mm x 240 mm. The box contains SPH soil particles and a plate with dimensions 100 mm x 100 mm x 10 mm placed within the soil particles. The plate is constrained in all directions and placed at different depths of the soil using multiple simulations. The HLFS tire is rolled over the soil within the box at speeds of 0.5 m/s, 1 m/s and 1.5 m/s and a vertical force of 2 kN. There is a node-to-node contact with edge treatment applied between the soil and plate. Another contact is between the HLFS tire and the SPH soil. The simulation is ended when the tire has full rolled the length of the box. This can be seen in Figure 5-1.

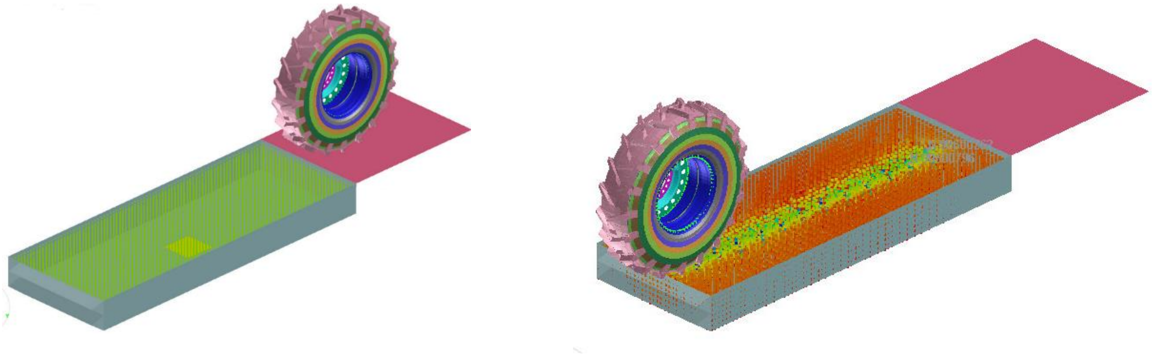

Figure 5-1: HLFS tire, SPH soil and plate model and stress distribution within SPH soil for 2 kN vertical load.

The first step in the procedure was to inflate the tire to an inflation pressure of 50 psi, similar to the experimental procedure. A vertical load of 2 kN is applied to the tire's spindle and allowed to rest onto a rigid platform and reach stability. The HLFS tire is then given a vertical velocity of 1 m/s and allowed to roll over the Clayey Loam soil.

The procedure shown in Figure 5-1 are conducted for the two terrains and the vertical force as a result of the tire's vertical load on the plate is obtained from the simulation's output file. The procedure is repeated for the plate placed at different soil depth's and changing tire longitudinal velocities. The force divided by the plate's area results in the stress induced onto the plate. This stress distribution as a function of time is then compared to experimental data *[74]*.

5.3 Stress Results and Discussion

The first simulation performed is to show the simulation's accuracy for stress distribution within a Clayey Loam soil by comparing with experimental results obtained from Urmia University [74]. The procedure included rolling the HLFS tire over a Clayey Loam soil and placing the plate at a soil depth of 200 mm. The tire has an inflation pressure of 193 kPa and longitudinal velocity of 1 m/s. The maximum stress on the plate is obtained from experimental and simulation and can be seen in Figure 5-2.

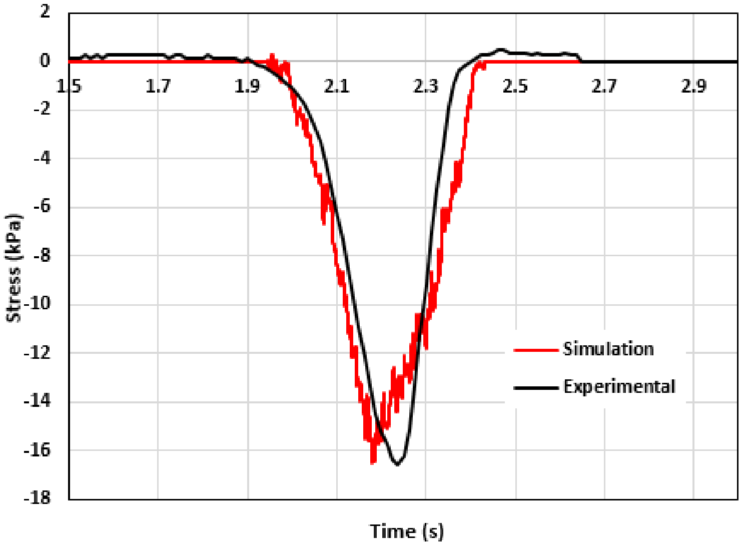

Figure 5-2: Stress distribution profile in simulation and experiment as a function of time for Clayey Loam. Procedure is for a 2 kN vertical load and 1 m/s tire velocity.

It can be seen from Figure 5-2 that the stress distribution as a function of time is very similar between the simulation and experimental results. The maximum stress in the experimental and simulation results are 16.592 kPa and 16.477 kPa, respectively which shows a 0.69% error. It can also be seen that the overall trend for the stress distribution as a function of time has a strong correlation between the experimental and simulated results. This verifies the accuracy of the stress obtained from simulations and stress results may be extracted at different times throughout the simulation. To conclude, at a soil depth of 200 mm and a tire velocity of 1 m/s, the stress distribution may be predicted using simulations with great accuracy.

Next, simulations at soil depth of 100 mm, 200 mm, 300 mm and 400 mm are conducted. Using a similar procedure, more SPH soil particles are added to the box in order to depict the stress in different soil depths. The results for the maximum stress and the stress distribution profiles are shown in Table 5-2 and Figure 5-3

Table 5-1: Maximum Stress for Simulation results at Clayey Loam soil depth of 100mm, 200mm, 300mm and 400 mm.

Soil Depth (mm)	Maximum Simulation Stress (kPa)
100	23.955
200	16.477
300	7.170
400	3.040

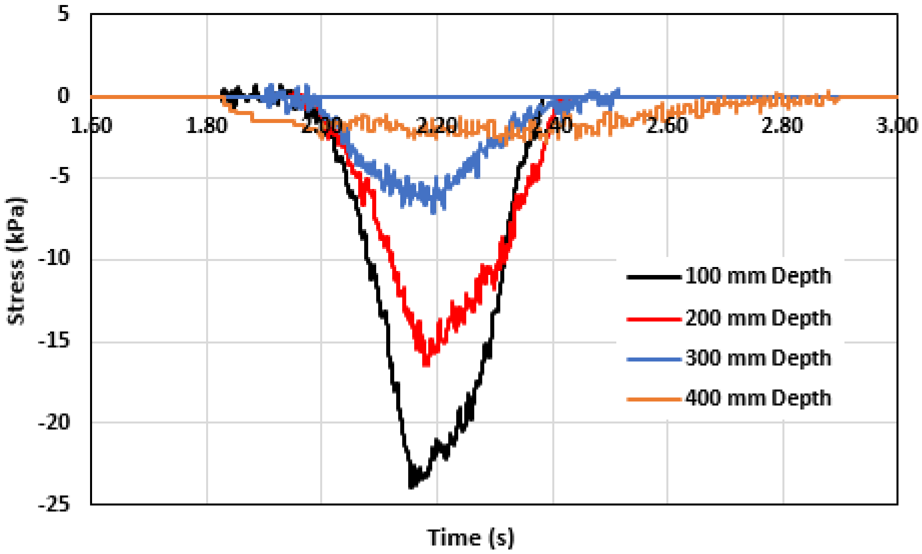

Figure 5-3: Stress distribution profile for Clayey Loam soil as a function of time for varying soil depth.

Table 5-2 shows that the maximum soil stress is obtained at a soil depth of 100 mm. As the soil depth is increased, the maximum stress decreases. This is due to loss of energy and forces felt between the soil and the plate. From Figure 5-3, the stress distribution profile’s also increase as the soil depth is increased. The time interval for the plate to feel the maximum stress is shorter and thus a narrow stress distribution profile is seen. It can also be seen that the forces from the tire are not properly felt at a soil depth of 400 mm. The experimental data using a soil depth of 200 mm and a tire speed of 1 m/s show great accuracy and therefore the other depths are assumed to be predicted with similar accuracy. In addition, other research conducted *[74]* have also shown similar trends for stress distribution but for varying vertical loads instead of soil depths. A moist Clayey Loam soil was modelled and maximum subsoil stress was determined for 1 to 15 passes of the HLFS tire with vertical loads of 1, 2, 4 and 5 kN; and soil moisture levels of 0, 10, 17 and 24%. The simulated results for stress distribution were compared with stress found in experiments. However, the research does not study the stress distribution at varying depths and varying tire velocity.

Moreover, the study of changing the tire velocity from 0.5 m/s to 1 m/s and further to 1.5 m/s is conducted. The tire is inflated to 193 kPa, a vertical load of 2 kN is applied and allowed to roll forward over the soil. The vertical forces are extracted for contact between the plate and soil at a soil depth of 200 mm. The stress distribution profiles for the varying tire velocity can be seen in Figure 5-4.

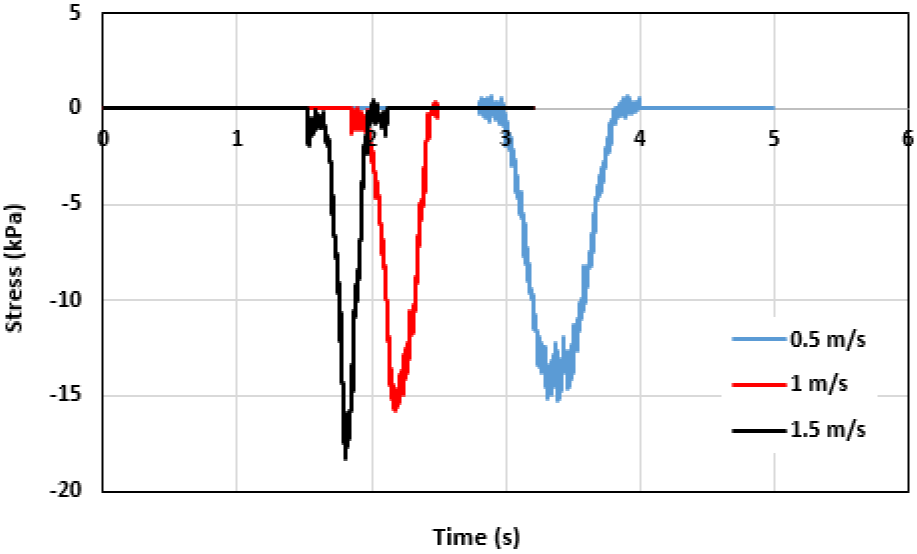

Figure 5-4: Stress distribution as a function of time for 2 kN vertical load, 344 kPa (50 psi) inflation pressure and varying tire speeds.

Figure 5-4 shows that the maximum stress is increased slightly as the tire velocity is increased. The stress increase (from 15.296 kPa to 15.817 kPa) is very subtle (3.1% difference) as the tire velocity is changed from 0.5 m/s to 1 m/s. However, as the velocity is further increased to 1.5 m/s, the maximum stress between the soil and plate is 18.345 kPa. This shows that the tire’s increase in velocity and dynamic change does show more forces being induced at a soil depth of 200 mm. The stress profile also shows that as the velocity is increased, the time interval for the stress increased is considerably shorter; as seen in the sharper and thinner stress profiles in Figure 5-4. The maximum stress is shown within 0.35 s, 0.53 s and 0.82s for tire speeds of 1.5 m/s, 1 m/s and 0.5 m/s respectively. The percent difference in time between 1.5 m/s and

1 m/s is 51.43%, while percent difference between 1 m/s and 0.5 m/s is 54.72%. This is expected as the speeds are increased 50% for the three simulations.

The last study conducted for stress distribution is for the LETE sand. The stress distribution simulation presented earlier are repeated for LETE sand. The material properties are changed to that of LETE sand and the tire is rolled over this sand at a tire velocity of 1 m/s, inflation pressure of 193 kPa and vertical load of 2 kN. The results are shown in Table 5-3 and Figure 5-5.

Table 5-2: Maximum stress for simulation results at a LETE sand depth of 100mm, 200mm, 300mm and 400 mm , tire velocity of 1 m/s, inflation pressure of 193 kPa and 2 kN vertical load.

Soil Depth (mm)	Maximum Simulation Stress (kPa)
100	27.226
200	23.083
300	22.132
400	12.072

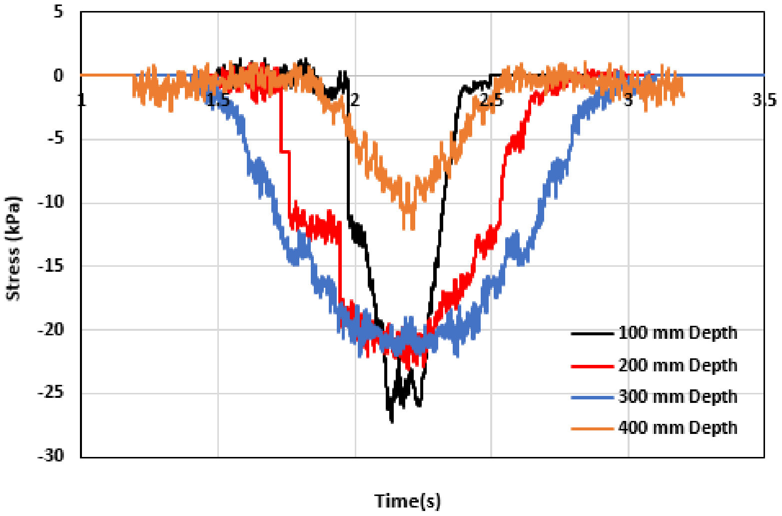

Figure 5-5: Stress distribution profile for LETE sand as a function of time for varying soil depth, 2 kN vertical load and 344 kPa (50 psi) inflation pressure.

The results for LETE sand show more force being transferred to corresponding soil depths when compared to Clayey Loam soil. The maximum stress at all four depths of the sand are higher than Clayey Loam. At a 100 mm depth the Clayey Loam had a maximum stress of 23.95 kPa while the LETE sand had a maximum stress of 27.23 kPa. At a 200 mm depth, the Clayey Loam had a maximum stress of 16.47 kPa while LETE sand had a maximum stress of 23.08 kPa. At a 300 mm depth, Clayey Loam had a maximum stress of 7.17 kPa while LETE sand had a maximum stress of 22.13 kPa. Lastly, at 400 mm depth, Clayey Loam had a maximum stress of 3.01 kPa while LETE sand showed a maximum stress of 12.07 kPa. Similar to Clayey Loam, the LETE sand has the highest stress at a 100 mm depth as expected. Although the increase of depth within the sand from 200 mm to 300 shows fairly similar maximum stress results. This shows that for Clayey Loam , the difference in stress does not show any change between the 200 mm to 300 mm depth.

5.4 Chapter Summary

This chapter studied the soil stress distribution for a Clayey Loam soil and LETE sand terrain found in many off-road applications. The previously modelled HLFS tire and two terrains are used in PAM-Crash's simulations. The tire with an inflation pressure of 193 kPa and vertical load of 2 kN is rolled over a box of SPH particles. Experimental stress results for this procedure were available for a soil depth of 200 mm. It was found that for this soil depth the forces found in the soil showed great accuracy between the experimental and simulated data. The maximum stress at a 200 mm depth for experimental and simulations were 16.592 kPa and 16.477 kPa respectively; with a percent error of 0.69%. The simulation was repeated for soil depths of 100mm, 200 mm, 300 mm and 400 mm. The simulated results show that as the soil depth increase, there is less force and therefore less stress transferred to lower depths. This is found for both the Clayey Loam and LETE sand terrain. It is also found that the forces transferred to the LETE sand particles are much higher at all the depths when compare to Clayey Loam. The effect of changing tire velocity in the simulations was also conducted. It showed that increasing tire velocity has a significant impact on the stress distribution at a soil depth of 200 mm. The greater difference in stress distribution is found between a tire velocity of 1 m/s and 1.5 m/s.

CHAPTER 6 - IN-PLANE AND OUT-OF-PLANE RIGID RING PARAMETERS

6.1 Chapter Introduction

This chapter covers the determination of the in-plane and out-of-plane off-road rigid ring model parameters for the HLFS agricultural tire running over Clayey Loam at different operating conditions. The parameters are calculated using a variation of operating conditions which include three vertical loads of 3000 N, 6000 N, and 9000 N; and three inflation pressures of 103 kPa, 193 kPa and 275 kPa. The vertical loads are decided based on the HLFS being much below operating load, at normal operating load and overloaded. Similarly, the inflation pressures are based on under inflation, normal operating tire pressure and over inflation. The in-plane and out-of-plane rigid rig parameters represents sets of translational and rotational stiffness and damping of the tire about the longitudinal and lateral axis. Due to the stiffness and durability of agricultural tires, low inflation pressures are used during operation. Determining these off-road rigid ring parameters for an agricultural tire on a clayey loam soil is a novel approach to study the tire's behaviour under varying operating conditions. It paves way for further implementing these parameters in full vehicle models where an overall performance of the vehicle may be studied.

6.2 In-Plane Rigid Ring Parameters

The rigid ring tire model proposed by Zegelar and Pacejka [12]and later implemented by Slade [18] and Lardner [66], using a soft soil is researched and their methods are implemented for this study. The in-plane parameters will be found using simulations conducted in ESI's Visual Environment PAM-Crash software. The rigid ring tire model proposed by Chae [2] is shown in Figure 6-1 and their parameters will be calculated.

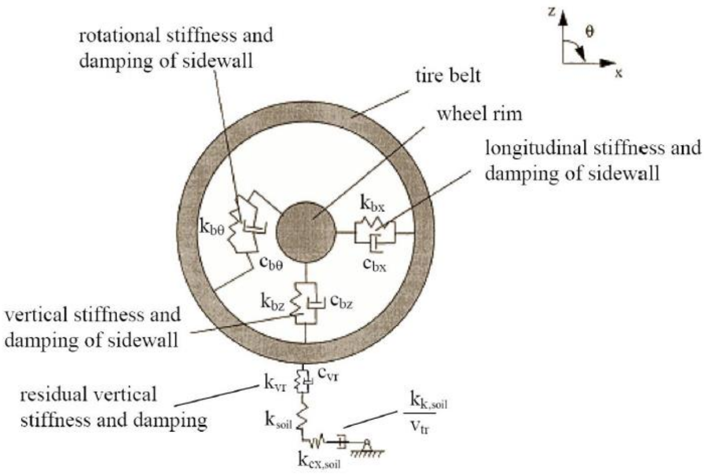

Figure 6-1: In-plane rigid ring tire model on soil and its parameters *[2]*.

The in-plane tire model proposes the wheel rim and tread band to be constructed as rigid bodies. The sidewall parameters are shown with a subscript 'b' and the tread behaviour are shown with subscript 'v'. The simple system is modelled using springs and dampers to study the stiffness and damping of the tire sidewalls and tread in conjunction with the soil's contribution.

In Figure 6-1, k_{bx} and c_{bx} is considered to be the longitudinal stiffness and damping of the tire's sidewall. This spring and damper system is contained between the rim and the rigid tread band. In our case, due to the tire model's symmetry, the longitudinal stiffness and damping is considered to be equal to the vertical stiffness and damping of the sidewall; k_{bz} and c_{bz}. A rotational spring and damper are used to model the rotational stiffness, $k_{b\theta}$, and damping of the sidewall $c_{b\theta}$ and are also located between the rigid rim and rigid tread band. In order to incorporate the tread stiffness and damping, a residual vertical stiffness k_{vr} and damping c_{vr} are included between the tire's tread and the longitudinal slip stiffness $k_{k,soil}$. The longitudinal slip stiffness considers the additional flexibility of the soil and is modelled in series with the tire's vertical residual stiffness. The tread's longitudinal stiffness with respect to the wheel is demonstrated using a longitudinal spring, $k_{cx,soil}$ and damper, $k_{k,soil}/v_{tr}$. This spring and damper system represents the longitudinal slip which occurs between the tread and contact patch at braking and accelerating.

6.2.1 Total Vertical Stiffness, $k_{tot,rigid\ surface}$

The total vertical stiffness on a hard surface is determined using simulations. The total vertical stiffness is the FEA tire model's resistivity to vertical or translational deformation after a force is applied. The tire is constrained to translate only in the vertical direction and inflated to inflation pressures of 103 kPa, 193 kPa and 275 kPa in three simulations. The tire is then brought down to settle on a rigid surface and reach stability after 0.5 seconds of the simulation. A ramp load of 3000 N is applied to the tire's spindle as shown in Figure 6-2. The output file obtained from simulations generates the load in terms of the vertical deflection as a plot. The slope of these curves represents the total vertical stiffness of the tire on a rigid surface. The total vertical stiffnesses were already calculated in Chapter 4 when validating the tire against experimental data. The total vertical stiffness has a linear trend and is expressed in Equation 6-1.

$$k_{tot} = \frac{Applied\ Load}{Vertical\ Deflection}\ kN/m \qquad 6\text{-}1$$

The total vertical stiffness is independent of the applied loading but depends on the inflation pressure. These values are listed in Table 6-1.

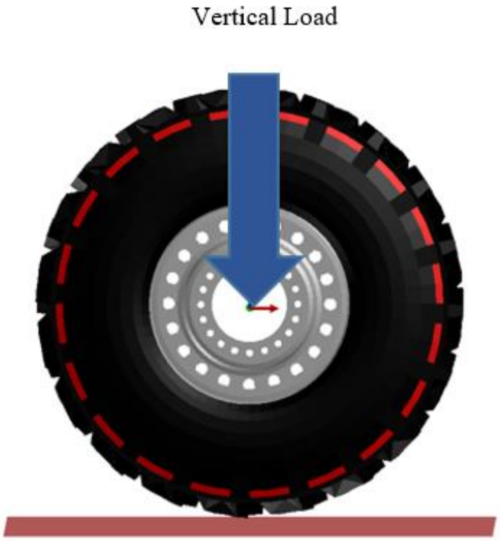

Figure 6-2: Total vertical stiffness test.

Table 6-1: Total vertical stiffness for several inflation pressures using 6000 N ramp load.

Parameter	103 kPa (15 psi)	193 kPa (28 psi)	275 kPa (40 psi)	Units
Total Vertical Stiffness – k_{tot}	525	422	448	kN/m

It is noticed that with an increase of inflation pressure from the nominal inflation pressure (193 kPa), the total vertical stiffness has also increased. It is interesting to notice that really under inflating the tire (103 kPa) has also increased the total vertical stiffness. This is due to the very stiff material the tire's sidewall and tread exhibit. As the tire is under inflated, the tire's material properties render the tire to have very stiff characteristics and do not deform as easily with the applied loading.

6.2.2 Vertical Stiffness and Residual Vertical Stiffness k_{bz}, and k_{vr}

The vertical stiffness and longitudinal stiffness represent the tire's sidewall stiffness in both the vertical and longitudinal direction. The tire's rotation about the lateral axis shows symmetry in both the longitudinal direction and vertical direction and as a result these stiffnesses are considered to be the same. The vertical stiffness and residual stiffness act vertically in series to the tire vertical axis as shown in Figure 6-1. The in-plane sidewall vertical stiffness, k_{bz}, and the residual vertical stiffness at the contact patch, k_{vr}, are calculated using the total vertical stiffness on a rigid surface and the tire's natural frequencies. The natural frequencies are obtained for the corresponding inflation pressure and loads although they do not differ too much in terms of load. As mentioned in Chapter 3, the vertical excitation of the tire on a rotating drum-cleat model gives us the first mode of vibration in Hz and ultimately gives us the natural frequency of the tire as seen in Equations 6-2 and Equation 6-3 and obtained from Chae [2], and Lardner [75].

The stiffness calculations are obtained using Equations 6-2 to 6-4:

$$\omega = \sqrt{\frac{k_{bz}+k_{vr}}{m_b}} \tag{6-2}$$

$$2\pi f = \sqrt{\frac{k_{bz}+k_{vr}}{m_b}} \tag{6-3}$$

$$\frac{1}{k_{tot}} = \frac{1}{k_{bz}} + \frac{1}{k_{vr}} \tag{6-4}$$

Where, ω is the natural frequency in rad/s

f is the vertical first mode of vibration frequency in Hz found using drum-cleat

m_b is the mass of the tire, corresponding to 37.2 kg

k_{bz} is the vertical sidewall stiffness in kN/m

k_{vr} is the residual vertical stiffness at contact patch in kN/m

k_{tot} is the total vertical deflection of the tire from simulations in kN/m

Using the above equations, the vertical sidewall stiffness and the residual vertical stiffness at the contact patch may be calculated. Table 6-2 shows the parameters for different loads and inflation pressures.

Table 6-2: HLFS sidewall vertical stiffness and residual vertical stiffness parameters.

		Inflation Pressure		
Parameter	Load (N)	103 kPa 15 PSI	193 kPa 28 PSI	275 kPa 40 PSI
First Mode Frequency- f (Hz)	3000	45.3	90.7	93.3
	6000	46.1	91.2	93.5
	9000	46.5	91.3	93.5
Natural Frequency – ω (rad/s)	3000	284.6	569.9	586.2
	6000	289.6	573.0	587.5
	9000	292.2	573.6	587.5
Total Vertical Stiffness – k_{tot} (kN/m)	3000	525.9	422.1	448.1
	6000	525.9	422.1	448.1
	9000	525.9	422.1	448.1
Sidewall Vertical Stiffness – k_{bz} (kN/m)	3000	2,334.2	11,644.3	12,318.4
	6000	2,450.2	11,776.6	12,375.0
	9000	2,510.9	11,802.1	12,375.0
Residual Vertical Stiffness - k_{vr} (kN/m)	3000	678.8	438.0	465.0
	6000	669.7	437.8	464.9
	9000	665.3	437.8	464.9

From the results, it can bee seen that as the inflation pressure increases, the sidewall vertical stiffness, k_{bz} increases. A large increase in the sidewall vertical stiffness (from around 2,000 kN/m to around 11,000 kN/m) is noticed when the tire is increased from an under inflated tire pressure (103 kPa) to nominal inflation pressure (193 kPa). As the inflation pressure increases to over inflation (275 kPa), the sidewall vertical stiffness increases further to around 12,300 kN/m.

The residual vertical stiffness at the contact interface, k_{vr}, has the highest values (around 670 kN/m) at under inflation pressure. At nominal inflation pressure the residual vertical stiffness is lowest at around 438 kN/m. As a result, the increase inflation pressure (103 kPa to 193 kPa) caused a decrease of 36.73% in residual vertical stiffness. When the inflation pressure is increased from 193 kPa to 275 kPa, a very slight increase (from 438 kN/m to 465 kPa) is seen in the residual vertical stiffness. The values for all three vertical stiffness parameters show negligible change as the vertical load during the simulations are increased from 3000 N to 9000N. Table 6-2 shows no change in total vertical stiffness for all inflation pressures as the vertical load is increased. The sidewall vertical stiffness shows very small change as the vertical load on the tire is increased. The greatest increase is obtained at 103 kPa inflation pressure and increasing vertical load from 3000 N to 6000 N. At inflation pressures 275 kPa, there is 0.46 % difference as vertical load is increased from 3000 N to 6000 N. Similar trends are shown in work done by Chae [2] and Lardner [75].

6.2.3 Total Vertical Damping, Vertical Sidewall Damping Constant and Residual Damping Parameters c_{tot}, c_{bz} and c_{vr}

This section includes the calculation of the total vertical damping and the residual damping constants which serve as vertical dampers in series from the tire rim, to the tread and contact patch. As previously discussed, due to the symmetry of tire's rotation about the tire spindle, the vertical sidewall damping constant c_{bz} is the same as the longitudinal sidewall damping constant c_{bx}.

Similar to the stiffnesses, the sidewall vertical damping constant and the residual damping constant at the contact patch are dampers in series. The inverse addition of both these damping constants will provide the total damping constant. As shown in Equation 6-5.

$$\frac{1}{c_{tot}} = \frac{1}{c_{bz}} + \frac{1}{c_{vr}} \qquad 6\text{-}5$$

The residual damping constant may be calculated using Equation 6-6;

$$c_{vr} = 2 \cdot \xi \cdot \sqrt{k_{vr} \cdot (m_b + m_a)} \qquad 6\text{-}6$$

Where, c_{vr} is the residual damping constant at the contact patch,

ξ is the critical damping ratio (5% as seen in most tire response)

m_b is the mass of the tire belt which is 37.2 kg

m_a is the mass of the rim which is 30 kg

The addition of the sidewall vertical damping constant and the residual damping constant are also related to the damping ratio, ξ, sidewall vertical stiffness constant, k_{bz}, and the residual vertical stiffness constant, k_{vr} as shown in Equation 6-7:

$$c_{bz} + c_{vr} = 2 \cdot \xi \cdot \sqrt{(k_{bz} + k_{vr}) \cdot m_b} \qquad 6\text{-}7$$

Using Equations 6-5 to 6-7, the total vertical damping constant, sidewall vertical damping constant and the residual damping constant were calculated the results are tabulated for the different vertical loads and inflation pressures in Table 6-3.

Table 6-3: The vertical sidewall damping, residual damping and total tire damping constants for HLFS tire over hard surface.

		Inflation Pressure		
Parameter	Load (N)	103 kPa (15 psi)	193 kPa (28 psi)	275 kPa (40 psi)
Vertical Sidewall Damping Constant c_{bz} (Ns/m)	3000	383.31	1,577.67	1,621.70
	6000	406.46	1,589.20	1,626.57
	9000	418.35	1,591.43	1,626.57
Residual Damping Constant c_{vr} (Ns/m)	3000	675.39	542.53	558.99
	6000	670.85	542.40	558.93
	9000	668.64	542.40	558.93
Total Tire Damping Constant c_{tot} (Ns/m)	3000	244.52	403.70	415.70
	6000	253.11	404.38	415.98
	9000	257.34	404.52	415.98

Table 6-3 showed that as the inflation pressure increases, the vertical sidewall damping constant and the residual damping constant increase as well. A large increase is seen in the vertical sidewall damping constant as the inflation pressure is increased from 103 kPa to 193 kPa. The damping constants have negligible difference as the load is increased similar to their stiffness calculated in the earlier section. The residual damping constant at the contact patch is seen to be the highest at under inflation (103 kPa), but still showed a general increase from nominal inflation pressure (193 kPa) to over inflation (275 kPa).

The vertical sidewall damping constant showed greatest increase (around 300% for all three vertical loads) as inflation pressure was increased from 103 kPa to 193 kPa. This means under inflation causes a significant change in the vertical sidewall constant. However, increasing from an inflation pressure of 193 kPa to 275 kPa caused an increase of around 3 percent in vertical sidewall damping constant. Similar to its corresponding stiffness, the vertical sidewall damping constant shows a slight increase as the vertical load is increased by 3000 N. As the vertical load is increased, the highest increase in vertical sidewall damping is shown at under inflation pressure and minimal change at over inflation pressure.

The residual damping constant was highest (around 670 Ns/m) at an inflation pressure of 103 kPa. As the inflation pressure increased to 193 kPa the residual damping constant decreased (around 20%) to around 542 Ns/m. Next, as the inflation pressure was increased to 275 kPa, the residual damping constant showed an increase of 3%. Table 6-3 also shows that as the vertical load is increased, there is almost no change in residual damping constant for nominal and over inflation pressure. However, at under inflation, increasing the vertical load has a slight decrease (around 0.74%) on the residual damping constant.

The total tire damping constant is greatly varied as the inflation pressure is increased from 103 kPa to 193 kPa with a percent increase of around 65.16%. As the inflation pressure is increased from 193 kPa to 275 kPa, the total tire damping constant changes from around 404 Ns/m to 415 Ns/m; which showed a slight increase of 2.7%. The change in vertical load showed an increase in total tire damping for under inflation pressure. Similar to the residual damping constant and the vertical sidewall damping constant, there is minimal change in the total tire damping constant as vertical load is increased to 6000 N and 9000N.

6.2.4 Rotational Tire Stiffness and Damping Constant, $k_{b\theta}$, and $c_{b\theta}$

The rotational tire stiffness, $k_{b\theta}$, and damping constant, $c_{b\theta}$, shows the resistibility of the tire's rotational motion when a rotational force is applied and its ability to dampen once the rotational force is released. The procedure consists of suspending the HLFS tire in space without contacting any surface. The rim is constrained so it cannot rotate or translate about any of the axis. The tire tread is considered to be rigid and constrained so it only rotates about the lateral axis. The tire is inflated at inflation pressures of 103 kPa, 193 kPa and 275 kPa and a tangential force (in the x-direction) is applied to the node in the base of the rigid tread as shown in Figure 6-3. The tread band then undergoes angular displacement about the lateral tire axis with respect to the rigid rim. Once the force is applied, it reaches a steady state angular displacement where the angular displacement does not change in respect with time. At steady state, the force is then suddenly removed which causes the sidewall and tread band to oscillate about the lateral axis which will allow for the damping constant in the rotational direction to be determined. The rotational stiffness may be calculated using Equation 6-8:

$$k_{b\theta} = \frac{Applied\ Moment}{Angular\ Displacement}\ \frac{kN \cdot m}{rad} \qquad 6\text{-}8$$

Where, the angular displacement is the steady state angular displacement during simulations.

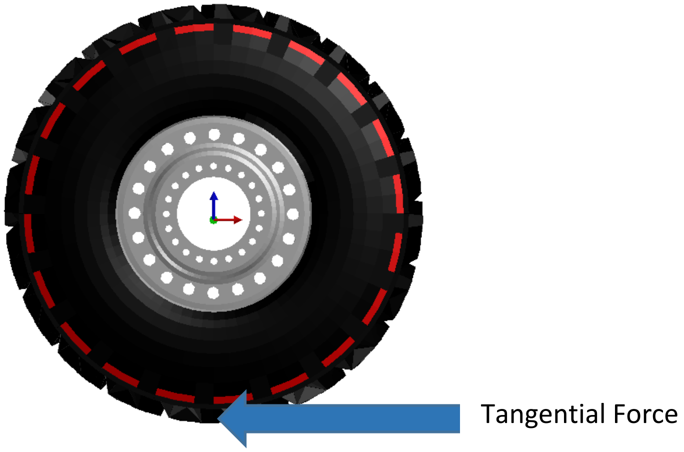

Figure 6-3: Rotational stiffness and damping simulation procedure for step load of 6000 N.

The partial graph for the angular displacement with respect to time is illustrated in Figure 6-4. From this data, the tread's steady state angular displacement, and its oscillating decay over time is obtained. Because of the stiff rubber properties, the angular displacements do not show much difference although a decrease in angular displacement is seen as the inflation pressure increases.

The damping constant, logarithmic decrement (δ) and damped period of vibration can now be calculated using the data obtained from Figure 6-4 and using Equations 6-9 to 6-15;

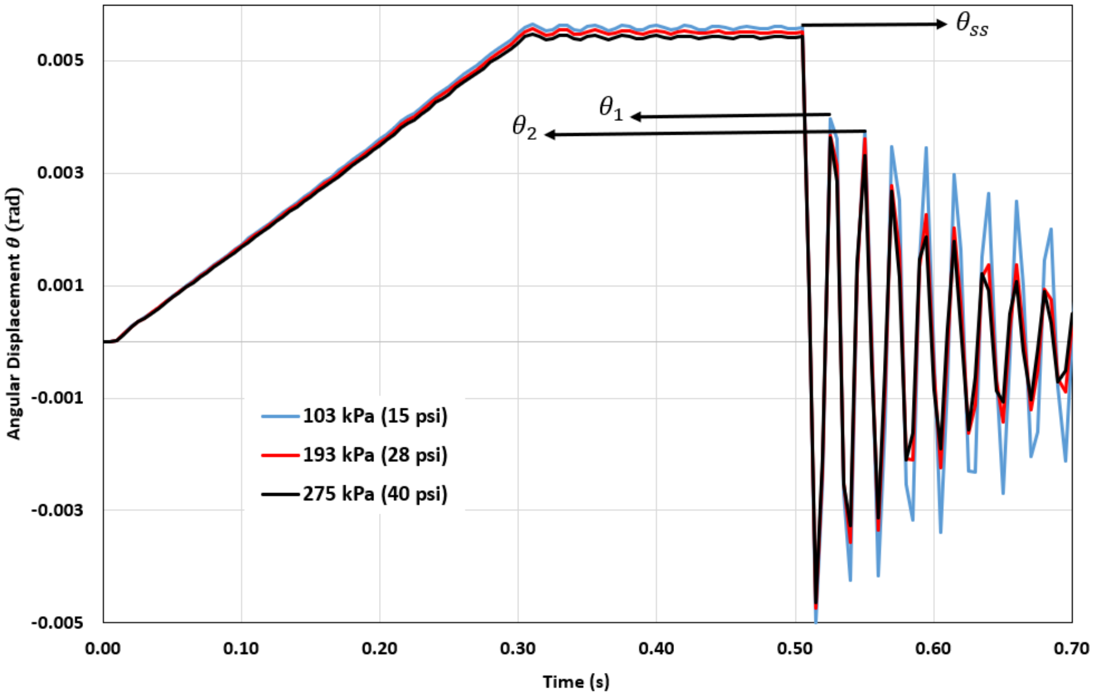

Figure 6-4: HLFS's angular displacement as a function of time for a rotational force of 6000 N and three inflation pressures.

Logarithmic Decrement:

$$\delta = \ln\left(\frac{\theta_1}{\theta_2}\right) \tag{6-9}$$

Damping Ratio:

$$\xi = \frac{\delta}{\sqrt{4\pi^2+\delta^2}} \tag{6-10}$$

Damped Period of Vibration:

$$\tau_d = t_2 - t_1 \tag{6-11}$$

Un-Damped Rotational Natural Frequency:

$$\omega_n = \frac{2\pi}{\tau_d\sqrt{1-\xi^2}} \tag{6-12}$$

Damped Rotational Natural Frequency:

$$\omega_d = \frac{2\pi}{\tau_d} \tag{6-13}$$

Critical Damping Constant:

$$C_c = 2 \cdot I_{by} \cdot \omega_n \tag{6-14}$$

Where I_{by} represents the mass moment of inertia of the tire belt, 5.586 kg·m^2

Rotational Damping Constant:

$$C_{b\theta} = \xi \cdot C_c \tag{6-15}$$

Table 6-4: Rotational Stiffness and Rotational Damping Constant Parameters

Parameter	103 kPa	193 kPa	275 kPa
Steady State Displacement - θ_{ss} – (rad)	0.00563	0.00554	0.00543
Rotational Stiffness - $k_{b\theta}$ - (kN·m/rad)	746.00	758.13	773.48
Logarithmic Decrement - δ	0.057	0.038	0.036
Damping Ratio – ξ	0.009	0.006	0.005
Damping Period of Vibration - τ_d – (s)	0.025	0.024	0.023
Un-Damped Rotational Natural Frequency - ω_n- (rad/s)	251.34	261.80	273.21
Damped Rotational Natural Frequency - ω_d – (rad/s)	251.32	261.80	273.18
Critical Damping Constant - c_c – (kN·m·s/rad)	2.806	2.924	3.052
Rotational Damping Constant - $c_{b\theta}$ – (kN·m·s/rad)	0.025	0.017	0.015

From Table 6-4, the rotational stiffness is shown to be very large as the sidewall rubber is a very stiff material and its rotation about the lateral axis is very hard to obtain. As the inflation pressure increased from 103 kPa to 193 kPa the rotational stiffness increased from 746 kN•m/rad to 758 kN•m/rad (1.6% difference). As the inflation pressure increased from 193 kPa to 275 kPa, the rotational stiffness increased from 758 kNm/rad to 773 kNm/rad (1.9% increase). The rotational damping constant decreased from 0.025 kN•m•s/rad to 0.017 kN•m•s/rad as inflation pressure increased from 103 kPa to 193 kPa. Furthermore, as the inflation pressure is increased to 275 kPa a rotational damping constant of 0.015 kN•m•s/rad.

6.2.5 Total Equivalent Vertical Stiffness, $k_{tot,Soil}$

The soil under the tire may also be represented as a stiffness (k_{soil}) in series with the vertical stiffness and residual vertical stiffness and is determined through simulations. The tire is inflated to the desired inflation pressure. The tire is constrained to translate only in the z-axis and the necessary damping and vertical loads are applied. The vertical stiffness of the soil is determined by applying vertical loads of 3000 N, 6000 N and 9000N on the tire's spindle with a Clayey loam soil box underneath. The slope of the load deflection curve for the tire spindle on the Clayey loam soil is obtained. The slope of the curve represents the soil stiffness as shown in Equation 6-16. Once the soil stiffness is determined, the total tire stiffness in Clayey loam soil, $k_{tot,soil}$, is calculated using the tire's sidewall, tread's residual and soil stiffness as shown in Equation 6-17.

Slade [18], developed the following equations for the total vertical stiffness of soil;

$$k_{\ Soil} = \frac{Applied\ Loading}{Sinkage}\ kN/m \qquad 6\text{-}16$$

$$k_{tot,Soil} = \frac{1}{k_{Dry\ Soil}} + \frac{1}{k_{bz}} + \frac{1}{k_{vr}}\ kN/m \qquad 6\text{-}17$$

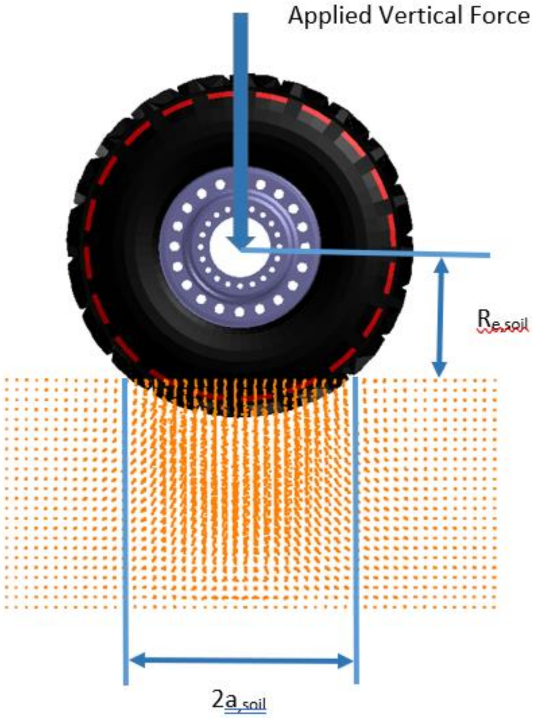

Figure 6-5: HLFS total equivalent vertical stiffness procedure on SPH Clayey Loam soil.

Figure 6-5 shows the procedure for calculating the Clayey loam stiffness. R_e represents the effective radius of the tire rolling on the soil. The contact patch length is defined as 2a, soil. These values are obtained from the simulations for the respective inflation pressure and vertical load. The soil stiffness and the total soil stiffness are tabulated in Table 6-5.

Table 6-5: HLFS total vertical stiffness parameters on Clayey Loam soil.

		Vertical Load (N)		
Parameter	Inflation Pressure (kPa)	3000	6000	9000
Vertical Stiffness of Soil, k_{soil} – kN/m	103	38	67	98
	193	40	66	95
	275	40	67	94
Total Vertical Stiffness of soil, $k_{tot,soil}$- kN/m	103	36	59	83
	193	37	57	78
	275	37	58	78

It can be seen that the vertical stiffness of soil and the total vertical stiffness of soil is directly dependent on the vertical load. As the vertical load is increased, both stiffness increases proportionally. The stiffness values do not change much with respect to the inflation pressure. It can be seen that the vertical stiffness of the soil is about one fifth of the total vertical stiffness on a rigid road for a 9000N vertical load. For a 6000 N vertical load and 193 kPa inflation pressure the soil stiffness is about one sixth of the total vertical stiffness on a rigid surface. Lastly, for a 3000 N vertical load and 193 kPa inflation pressure, the soil stiffness is almost one tenth of the total vertical stiffness on a rigid surface. This is due to the fact that the soil stiffness is dependent on the vertical load where the total vertical stiffness on a rigid surface is independent of the vertical load. As the vertical load is increased, the soil is compacted and the stiffness increases.

6.2.6 Longitudinal Tire Stiffness, $k_{k,soil}$

The longitudinal slip stiffness, $k_{k,soil}$, is modelled as a spring positioned between the tire and surface. It models the longitudinal slip and the forces felt while the tire is undergoing braking or accelerating. This parameter is obtained assuming its value is equal under braking or acceleration. As mentioned earlier, the soil is also assumed to act as a linear spring in series with the residual vertical stiffness similar to the in-plane rigid ring model.

A virtual test, as shown in Figure 6-6, is performed where the tire is given 100% slip conditions on the clayey loam soil. The tire is inflated and a vertical load is applied to the tire's spindle. The tire is quickly accelerated to a rotational velocity of around 20 rad/s which is around 30 km/h given a tire radius of 0.420 m, and the tire is allowed to roll forward in the Clayey Loam soil. The tire is rolled over the Clayey Loam until around 0% slip condition is obtained and the simulation is ended. The longitudinal force is obtained from the contact between the tire and the Clayey Loam soil. The percent slip is found from the tire's angular and translational velocity. At each time step the longitudinal force is obtained for a percent slip from 0% slip to 100% slip. The longitudinal tire stiffness is considered to be the slope of the longitudinal force vs percent slip for percent slip of 0% to 10% and is described by Equation 6-18.

$$k_{k,soil} = \frac{\partial Longitudinal\ Force}{\partial Slip\%}\Big|_{slip=0\%} \frac{kN}{unit\ slip} \qquad 6\text{-}18$$

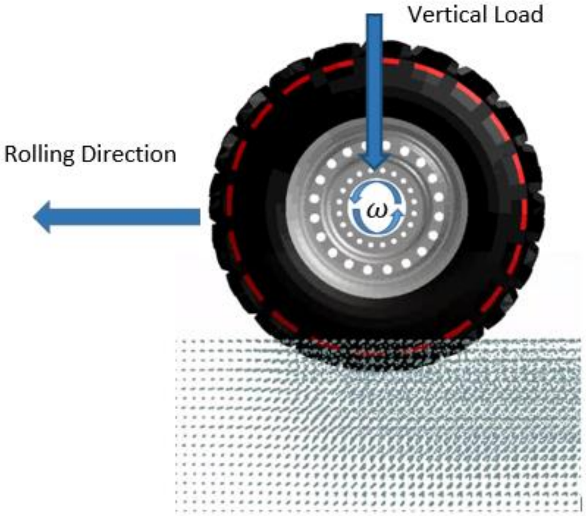

Figure 6-6: Longitudinal tread stiffness test at 0% slip condition.

The longitudinal slip stiffness plot for an inflation pressures of 103 kPa, 193 kPa and 275 kPa, and a vertical load of 9000 N is shown in Figure 6-7.

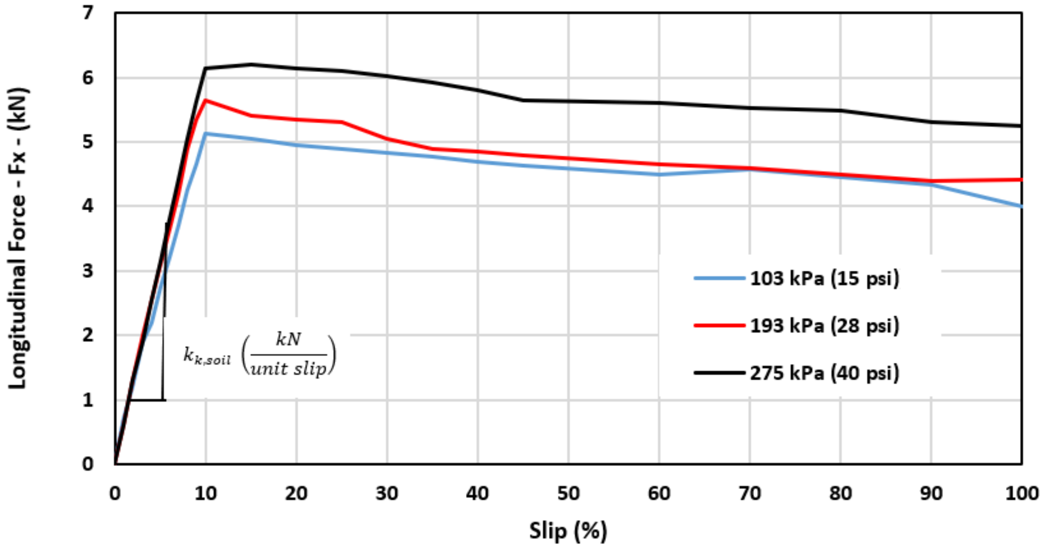

Figure 6-7: Longitudinal force as a function of slip at 9000 N vertical load and different inflation pressures.

Figure 6-7 shows that the highest longitudinal force for all three inflation pressures are obtained within a 10% slip condition. The largest peak longitudinal force (6.12 kN) is seen for 275 kPa. For an inflation pressure of 103 kPa, the lowest peak of 5.09 kN is seen. Lastly, an inflation pressure of 193 kPa showed a peak longitudinal force of 5.68 kN. For all three inflation pressures, the longitudinal force decreases slightly until a 100% slip condition is achieved.

The longitudinal tire tread damping is shown as a ratio between the longitudinal tire stiffness found from Figure 6-7, and the steady state linear velocity measured at the tire's spindle (v_{tr}). The longitudinal tread stiffness, k_{cx}, is calculated by dividing the longitudinal tire stiffness by half of the contact length as shown in Equation 6-19. This equation was defined primarily by Zegelaar and Pacejka [12], and later implemented by Chae [2], Slade [18] and Lardner [75]. It is noted that Equation 6-19 is only valid for slip ratios less than 0.1 meaning there is adhesion between the tire and the surface it is rolling on [12].

$$k_{cx,soil} = \frac{k_{k,soil}}{a} \quad \frac{kN}{m} \qquad \text{6-19}$$

Where, a is half the contact length between the HLFS tire and Clayey Loam for a variation of inflation pressures and vertical loads.

Table 6-6 contains the data and calculations for the longitudinal tire and tread stiffness, longitudinal tread damping, projected contact length, effective rolling radius, and steady state tread speed.

Table 6-6: HLFS longitudinal tire and tread stiffness parameters on Clayey Loam

		Inflation Pressure (kPa)		
Parameter	Load (N)	103	193	275
Longitudinal Tire Stiffness - $k_{k,soil}$ (kN/unit slip)	3000	15.3	16.7	18.9
	6000	22.1	24.3	36.1
	9000	51.3	56.0	61.4
Longitudinal Tread Stiffness - $k_{cx,soil}$- (kN/m)	3000	64.2	70.2	78.8
	6000	83.6	91.9	139.2
	9000	177.8	193.1	211.4
Projected Contact Length – $2a_{soil}$ (m) (As shown in Figure 6-5)	3000	0.477	0.476	0.480
	6000	0.529	0.529	0.530
	9000	0.577	0.580	0.581
Effective Rolling Radius - $R_{e,soil}$ (m)	3000	0.341	0.345	0.345
	6000	0.331	0.329	0.330
	9000	0.329	0.326	0.324
Tread Speed - v_{tr} (m/s)	3000	7.31	7.31	7.31
	6000	7.04	7.04	7.04
	9000	6.31	6.31	6.31
Longitudinal Tread Damping - $\frac{k_{k,soil}}{v_{tr}}$ (kN·s/m)	3000	2.1	2.3	2.6
	6000	3.2	3.5	5.1
	9000	8.1	8.9	9.7

It can be seen that the longitudinal tire and tread stiffness, increased as the vertical load is increased. For an inflation pressure of 103 kPa, the longitudinal tire stiffness increased from 15.3 kN/unit slip to 22.1

kN/unit slip as the vertical load increased from 3000 N to 6000 N (44% increase). As the vertical load was increased to 9000 N, the longitudinal tire stiffness increased from 22.1 kN/unit slip to 51.3 kN.unit slip (132% increase). A very similar trend is observed for inflation pressures of 193 kPa and 275 kPa. As the inflation pressure increases, the longitudinal tire stiffness shows a slight increase at a 3000 N load and larger increase at 9000 N.

The longitudinal tread stiffness shows very similar trends as the longitudinal tire stiffness. For a 3000 N vertical load, as the inflation pressure is increased to 193 kPa and 275 kPa, a percent difference of 9.34% and 12.25% is obtained in the longitudinal tread stiffness. At an inflation pressure of 103 kPa, as the vertical load is increased to 6000 N and 9000 N, a percent difference of 30.21% and 112.68% is obtained in the longitudinal tread stiffness.

Similarly, the contact length increased as the vertical load was increased and negligible difference was seen as the inflation pressure was increased. For an inflation pressure of 103 kPa, as the vertical load was increased from 3000 N to 6000 N, the contact length increased from 0.477 m to 0.529 m. Similarly, as the vertical load was increased from 6000 N to 9000 N, the contact length increased from 0.529 m to 0.577.

The effective rolling radius decreased as the vertical load is increased, which shows the tire had sunk into the Clayey Loam as the vertical load is increased. Similar to the contact length, the effect of increasing the inflation pressure was minimal on the effective rolling radius. Lastly, the longitudinal tread damping has also increased as the vertical load increased although the effect of inflation pressure was insignificant. A higher increase in the longitudinal tread damping was found as the vertical load was increased from 6000 N to 9000 N.

The in-plane rigid ring parameters, effective contact patch and effective rolling radius at inflation pressures of 103 kPa, 193 kPa and 275 kPa are tabulated in Table 6-7 to Table 6-9 for vertical loads of 3000 N, 6000 N and 9000 N, respectively.

Table 6-7: In-plane off-road rigid ring parameters for 3000 N vertical load.

In-Plane Rigid Ring Parameters 3000 N Load	**103 kPa**	**193 kPa**	**275 kPa**
Total Vertical Stiffness - k_{tot} (kN/m)	525.92	422.14	448.13
Sidewall Stiffness - k_{bz} (kN/m)	2,334.2	11,644.3	12,318.4
Residual Vertical Stiffness - k_{vr} (kN/m)	678.8	438.0	465.0
Vertical Damping Constant - c_{bz} (kN.s/m)	383.31	1,577.67	1,621.70
Residual Damping Constant - c_{vr} (kN.s/m)	675.39	542.53	558.99
Tire Damping Constant - c_{tot} (kN.s/m)	244.52	403.70	415.70
Rotational Stiffness - $k_{b\theta}$ (kN.m/rad)	746.00	758.13	773.48
Rotational Damping Constant - $c_{b\theta}$ (kN.m.s/rad)	0.025	0.017	0.015
Soil Stiffness, Clayey Loam – k_{soil} (kN/m)	38	40	40
Total Equivalent Vertical Stiffness, Clayey Loam - $k_{tot,\text{soil}}$ (kN/m)	36	37	37
Longitudinal Tread Stiffness, Clayey Loam– $k_{cx,\text{soil}}$ (kN/m)	64.2	70.2	78.8
Longitudinal Tire Stiffness, Soil $k_{k,\text{soil}}$ (kN/unit slip)	15.3	16.7	18.9
Longitudinal Tread Damping, Clayey Loam - $k_{k,\text{soil}/vtr}$ (kN.s/m)	2.1	2.3	2.6
Effective Contact Patch, Clayey Loam - $2_{a,\text{soil}}$ (m)	0.341	0.345	0.345
Effective Rolling Radius, Clayey Loam - ($R_{e,\text{soil}}$) (m)	0.341	0.345	0.345

Table 6-8: In-plane off-road rigid ring parameters for 6000 N vertical load.

In-Plane Rigid Ring Parameters 6000 N Load	**15 psi**	**28 psi**	**40 psi**
Total Vertical Stiffness - k_{tot} (kN/m)	525.92	422.14	448.13
Sidewall Stiffness - k_{bz} (kN/m)	2,450.2	11,776.6	12,375.0
Residual Vertical Stiffness - k_{vr} (kN/m)	669.7	437.8	464.9
Vertical Damping Constant - c_{bz} (kN.s/m)	406.46	1,589.20	1,626.57
Residual Damping Constant - c_{vr} (kN.s/m)	670.85	542.40	558.93
Tire Damping Constant - c_{tot} (kN.s/m)	253.11	404.38	415.98
Rotational Stiffness - $k_{b\theta}$ (kN.m/rad)	746.00	758.13	773.48
Rotational Damping Constant - $c_{b\theta}$ (kN.m.s/rad)	0.025	0.017	0.015
Soil Stiffness, Clayey Loam – k_{soil} (kN/m)	67	66	67
Total Equivalent Vertical Stiffness, Clayey Loam - $k_{tot,\text{soil}}$ (kN/m)	59	57	58
Longitudinal Tread Stiffness, Clayey Loam– $k_{cx,\text{soil}}$ (kN/m)	83.6	91.9	139.2
Longitudinal Tire Stiffness, Soil $k_{k,\text{soil}}$ (kN/unit slip)	22.1	24.3	36.1
Longitudinal Tread Damping, Clayey Loam - $k_{k,\text{soil}/vtr}$ (kN.s/m)	3.2	3.5	5.1
Effective Contact Patch, Clayey Loam - $2_{a,\text{soil}}$ (m)	0.529	0.529	0.530
Effective Rolling Radius, Clayey Loam - ($R_{e,\text{soil}}$) (m)	0.331	0.329	0.330

Table 6-9: In-plane off-road rigid ring parameters for a vertical load of 9000 N.

In-Plane Rigid Ring Parameters 9000 N Load	**15 psi**	**28 psi**	**40 psi**
Total Vertical Stiffness - k_{tot} (kN/m)	525.92	422.14	448.13
Sidewall Stiffness - k_{bz} (kN/m)	2,510.9	11,802.1	12,375.0
Residual Vertical Stiffness - k_{vr} (kN/m)	665.3	437.8	464.9
Vertical Damping Constant - c_{bz} (kN.s/m)	418.35	1,591.43	1,626.57
Residual Damping Constant - c_{vr} (kN.s/m)	668.64	542.40	558.93
Tire Damping Constant - c_{tot} (kN.s/m)	257.34	404.52	415.98
Rotational Stiffness - $k_{b\theta}$ (kN.m/rad)	746.00	758.13	773.48
Rotational Damping Constant - $c_{b\theta}$ (kN.m.s/rad)	0.025	0.017	0.015
Soil Stiffness, Clayey Loam – k_{soil} (kN/m)	98	95	94
Total Equivalent Vertical Stiffness, Clayey Loam - $k_{tot,\text{soil}}$ (kN/m)	83	78	78
Longitudinal Tread Stiffness, Clayey Loam– $k_{cx,\text{soil}}$ (kN/m)	177.8	193.1	211.4
Longitudinal Tire Stiffness, Soil $k_{k,\text{soil}}$ (kN/unit slip)	51.3	56.0	61.4
Longitudinal Tread Damping, Clayey Loam - $k_{k,\text{soil}/vtr}$ (kN.s/m)	8.1	8.9	9.7
Effective Contact Patch, Clayey Loam - $2_{a,\text{soil}}$ (m)	0.577	0.580	0.581
Effective Rolling Radius, Clayey Loam - ($R_{e,\text{soil}}$) (m)	0.329	0.326	0.324

6.3 Out-of-Plane Rigid Ring Parameters

This section outlines the prediction of the out-of-plane off-road rigid-ring parameters for the HLFS agricultural tire on an SPH Clayey Loam soil at various operating conditions. All of the rigid ring parameters are found using inflation pressures; of 103 kPa (15 psi), 193 kPa (28 psi) and 275 kPa (40 psi) and vertical loads of 3000 N, 6000 N, and 9000 N. The out-of-plane off-road rigid ring parameters are shown in Figure 6-8.

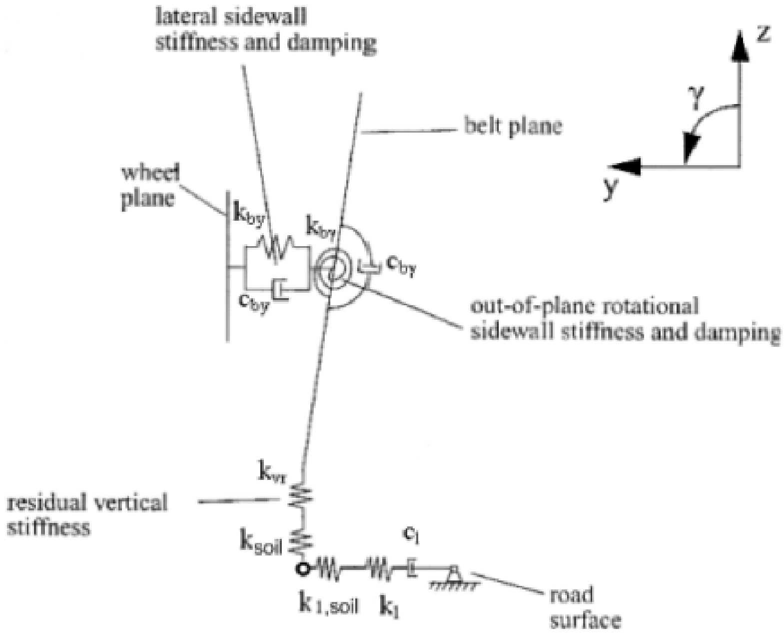

Figure 6-8: Out-of-plane off-road rigid ring parameters *[2]*.

The out-of-plane rigid ring model depicts the stiffness and damping of the tire in the lateral axis and about the longitudinal axis. The translational sidewall stiffness, k_{by}, and damping constant, c_{by}, is shown in Figure 6-8. The rotational sidewall stiffness, $k_{b\gamma}$, and damping constant, $c_{b\gamma}$, are modelled using torsional springs and dampers and predict the tire's rotational resistivity about the longitudinal axis. The residual vertical stiffness and damping are the same for both in-plane and out-of-plane model. In order to incorporate the effect of soil, the vertical tire stiffness under soil are represented by k_{soil} as obtained from the in-plane off-road rigid ring parameters. The tire's sidewall lateral stiffness, k_l, and damping, c_l, shown as a horizontal spring and damper represents the sidewall's resistivity and damping to any lateral force applied at the spindle of the tire. The lateral stiffness of the soil, $k_{l,soil}$, represents the flexibility of the soil with a lateral load applied to the tire's centre. In upcoming sections within this chapter, the simulation procedure and results will be discussed more thoroughly.

6.3.1 Translational Stiffness and Damping Constant, k_{by}, and c_{by}

The translational stiffness is needed in order to learn the resistivity of the tire to a lateral load applied to the top and bottom portion of the tire. The damping constant allows for the energy absorption and damping capability of the tire when these loads are applied. The simulation conducted may be seen in Figure 6-9. The tire is constrained in space and the rim is considered to be a rigid body. The tread base and tread band are constrained so they are only allowed to translate in the lateral direction. The tire is then inflated to a certain inflation pressure and two lateral loads of 15,000 N are applied to the top and bottom nodes on the tread. Once the load is applied for a few seconds, steady state displacement in the lateral direction achieved. The two loads are then simultaneously released and the tire will oscillate about the equilibrium position until it reaches equilibrium. From the translational displacement as a function of time plot, the steady state lateral displacement, logarithmic decrement, and transience is observed. The calculations for the translational stiffness and damping constants are calculated using Equations 6-20 – 6-27.

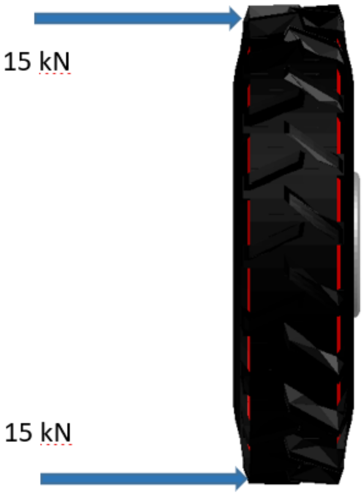

Figure 6-9: HLFS translational stiffness test with two 15 kN translational loads.

The plot for the translational stiffness simulation for three different inflation pressures can be seen in Figure 6-10.

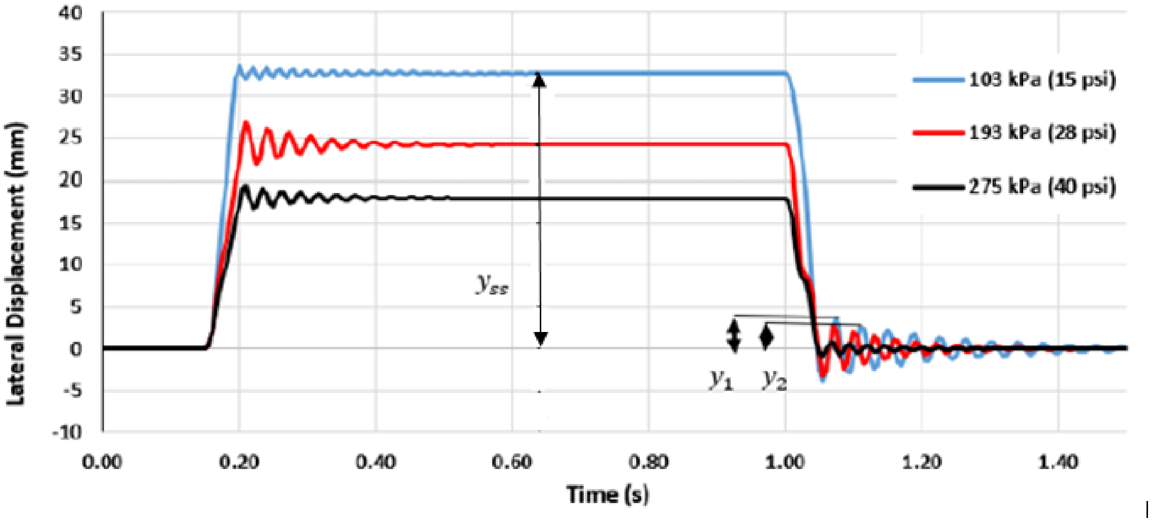

Figure 6-10: HLFS out-of-plane translational stiffness procedure at 15 kN lateral load.

The sidewall translational stiffness, k_{by} is calculated by dividing the combined applied lateral force by the steady state translational displacement of the tire as shown in Equation 6-20.

$$k_{by} = \frac{Lateral\ Force}{Lateral\ Displacement}\ kN/m \tag{6-20}$$

The tire's sidewall is the part of the tire that elastically deforms during this test as the tread band is assumed to be rigid. When the tire's lateral load is taken away rapidly, the vibration in the lateral direction decreases over time. The initial and second amplitude of the oscillations (as seen in Figure 6-10) are used to calculate the logarithmic decrement, δ. Similarly, the time period between the first and second oscillation is used to calculate the damped period of vibration, τ_d. The damping ratio, ξ , is then calculated using the logarithmic decrement. The un-damped translational natural frequency is then calculated using the damping ratio and the damped period of vibration. Next, the damped translational natural frequency is calculated using the damped period of vibration. Lastly, the critical damping constant and the translational damping constant are calculated using the mass of the tire belt, un-damped translational natural frequency and the damping ratio. The following equations show these calculations.

Logarithmic Decrement:

$$\delta = \ln\left(\frac{y_1}{y_2}\right) \qquad 6\text{-}21$$

Damping Ratio:

$$\xi = \frac{\delta}{\sqrt{4\pi^2+\delta^2}} \qquad 6\text{-}22$$

Damped Period of Vibration:

$$\tau_d = t_2 - t_1 \qquad 6\text{-}23$$

Un-Damped Translational Natural Frequency:

$$\omega_n = \frac{2\pi}{\tau_d\sqrt{1-\xi^2}} \qquad 6\text{-}24$$

Damped Translational Natural Frequency:

$$\omega_d = \frac{2\pi}{\tau_d} \qquad 6\text{-}25$$

Critical Damping Constant:

$$C_c = 2 \cdot m_b \cdot \omega_n \qquad 6\text{-}26$$

Where $m_b$is the mass of the tire, 67.2 kg.

Translational Damping Constant:

$$C_{by} = \xi \cdot C_c \qquad 6\text{-}27$$

Table 6-10 contains the calculations for the translational sidewall stiffness and damping constant parameters for three different inflation pressure. The parameters are considered to be independent of the lateral load applied.

Table 6-10: Sidewall translational stiffness and damping parameters for a 30 kN lateral load.

	Inflation Pressure (kPa)		
Parameter	103 kPa	193 kPa	275 kPa
Steady State Displacement -y_{ss}- (m)	0.032	0.024	0.018
Translational Sidewall Stiffness - k_{by}- (kN/m)	937.500	1,250.000	1666.666
Logarithmic Decrement – δ	0.332	0.320	0.173
Damping Ratio - ξ	0.053	0.051	0.028
Damped Period of Vibration - τ_d – (s)	0.040	0.030	0.030
Un-Damped Natural Frequency - ω_d – (rad/s)	157.080	209.440	209.440
Critical Damping Constant - C_c – (kN·s/m)	21.141	28.185	28.159
Translational Damping Constant - C_{by}(kN·s/m)	1.120	1.437	0.788

From Table 6-10, it can be seen that the translational sidewall stiffness increases as the inflation pressure increases. This make sense as there is more resistance laterally as the inflation pressure is against the sidewalls and the steady state displacement decreases with increase of inflation pressure. As the inflation pressure increased from 103 kPa to 193 kPa, the translational sidewall stiffness increased from 937.5 kN/m to 1250 kN/m. As the inflation pressure was increased to 275 kPa, a translational sidewall stiffness of 1666.6 was obtained. This showed an increase of 33.3 % as the inflation pressure increased to 193 and 275 kPa. The translational damping constant increased as the inflation pressure was increased from 103 kPa to 193 kPa. However, when the inflation pressure is further increased to 275 kPa, the damping constant decreased to a value of 0.788 kNs/m.

6.3.2 Rotational Stiffness and Damping Constant, $k_{b\gamma}$ and $c_{b\gamma}$

The rotation about the tire's longitudinal axis is expressed by rotational spring and damper system as seen previously in Figure 6-8. The tire's sidewall rotational stiffness, $k_{b\gamma}$ predicts the sidewall's response to any rotational forces applied to the top and bottom of the rigid tread as shown in Figure 6-11. The simulation procedure is similar to the translational stiffness procedure, except the lateral forces on the top and bottom portion of the tread are in opposite direction. Similarly, the lateral forces are applied to the rigid tread while the rim is assigned a rigid body. The tire is also constrained to spin about the lateral axis or about its spindle. The lateral forces of 15 kN each are applied and held until a steady state rotational displacement is achieved. The forces are then taken off the tire suddenly and the tire is allowed to oscillate back to its original position.

Figure 6-11: Rotational stiffness test using 15 kN lateral load.

The plot for the angular displacement as a function of time is shown in Figure 6-12.

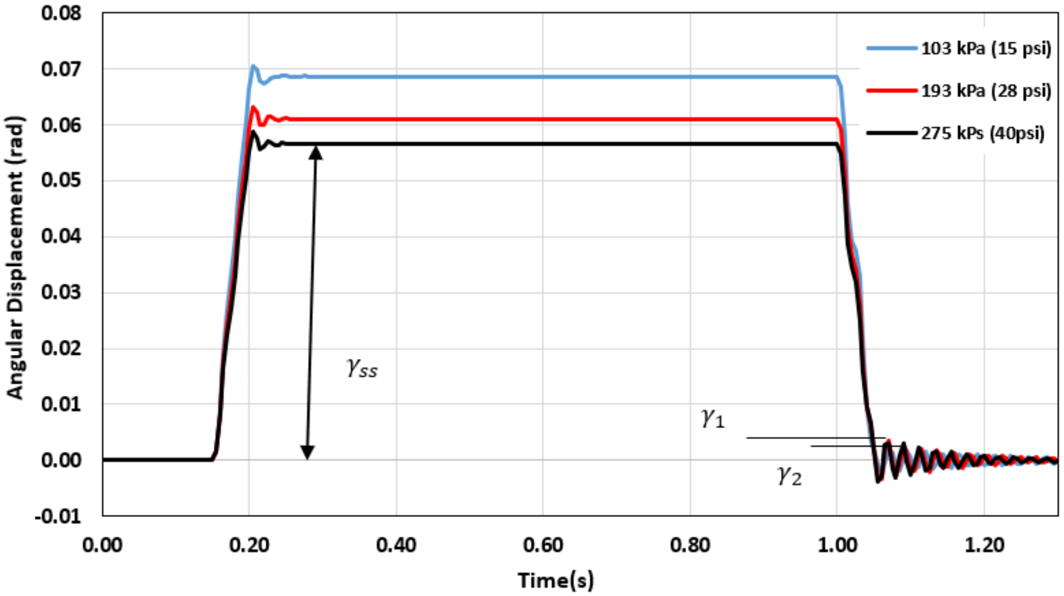

Figure 6-12: HLFS out-of-plane rotational stiffness test using rotational load of 15 kN.

The rotational stiffness is calculated using the applied rotational moment and dividing by its respective angular displacement as shown in Equation 6-28.

$$k_{b\gamma} = \frac{Applied\ Moment}{Angular\ Displacement}\ kN \cdot m/rad \qquad 6\text{-}28$$

Similar to earlier procedures, the release of the lateral load will cause oscillations about the longitudinal axis. The first and second oscillation's peaks, their period are used to calculate the logarithmic decrement, damping ratio, un-damped rotational frequency, and the translational damping constant for the sidewall; as shown in the following Equations. The data needed for these calculations are shown in Figure 6-12.

Logarithmic Decrement:

$$\delta = \ln\left(\frac{\gamma_1}{\gamma_2}\right) \qquad 6\text{-}29$$

Damping Ratio:

$$\xi = \frac{\delta}{\sqrt{4\pi^2+\delta^2}} \qquad 6\text{-}30$$

Damped Period of Vibration:

$$\tau_d = t_2 - t_1 \qquad 6\text{-}31$$

Un-Damped Rotational Frequency:

$$\omega_n = \frac{2\pi}{\tau_d\sqrt{1-\xi^2}} \qquad 6\text{-}32$$

Damped Rotational Frequency:

$$\omega_d = \frac{2\pi}{\tau_d} \qquad 6\text{-}33$$

Critical Damping Constant:

$$C_c = 2 \cdot I_{bx} \cdot \omega_n \qquad 6\text{-}34$$

Where $I_{bx}$is the mass moment of inertia of the tire belt; 5.586 kg·m^2

Rotational Damping Constant:

$$C_{b\gamma} = \xi \cdot C_c \qquad 6\text{-}35$$

The results for the rotational stiffness and damping constant parameters can be seen in Table 6-11.

Table 6-11: HLFS rotational stiffness and damping constant parameters.

	Inflation Pressure (kPa)		
Parameter	103	193	275
Steady State Displacement - γ_{ss} (rad)	0.068	0.061	0.056
Rotational Stiffness - $k_{b\gamma}$ (kN·m/rad)	185.294	206.557	222.615
Logarithmic Decrement – δ	0.032	0.261	0.095
Damping Ratio – ξ	0.005	0.042	0.015
Damped Period of Vibration - τ_d (s)	0.020	0.020	0.020
Un-Damped Natural Frequency - ω_d (rad/s)	314.159	314.159	314.159
Critical Damping Constant - c_c (kN·s/m)	3.509	3.513	3.510
Rotational Damping Constant - c_{by} (kN·s/m)	0.018	0.148	0.053

Similar to previous trends, the rotational stiffness is increased as the inflation pressure increases. As the inflation pressure is increased from 103 kPa to 193 kPa a 11.4% increase in rotational stiffness is obtained. As the pressure is increased from 193 kPa to 275 kPa a 7.7% increase if shown. In this case, the rotational oscillations are damped to stability in a very quick manner for all three inflation pressures. The difference in the angular displacement peaks do not contribute to changing the un-damped natural frequency for all three inflation pressures. However, it can be seen that the highest value for the rotational damping constant is for the nominal inflation pressure of 193 kPa (28 psi). The lowest rotational damping constant was obtained for an inflation pressure of 103 kPa.

6.3.3 Lateral Tire Stiffness and Damping Constant, k_l, and c_l

The lateral tire stiffness, k_l, and damping constant, k_l, are obtained by conducting the lateral stiffness test as shown in Figure 6-13. The stiffness and damping constants will be obtained for inflation pressures of 103 kP, 193 kPa and 275 kPa; and vertical loads of 3000 N, 6000 N and 9000 N. The test involves inflating the tire to the desired inflation pressure and resting the tire onto a rigid surface. A lateral load of 1.5 kN is applied to the tire's spindle which will produce a plot of lateral displacement over the period of time allocated to the simulation. The lateral load is held until a steady state lateral displacement is achieved. Next, the lateral load is released quickly and the tire is allowed to oscillate about its initial equilibrium position in the lateral direction. The dissipating of energy from the applied load and the first and second subsequent peak values of lateral deformation allows for the calculation of the logarithmic decrement and finally the lateral damping constant; similar to earlier sections.

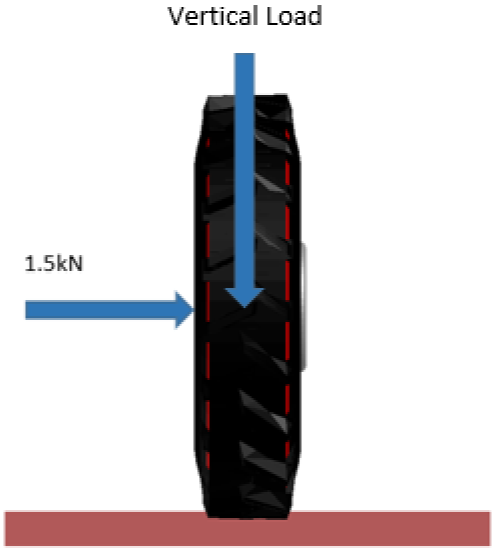

Figure 6-13: Lateral stiffness test with a 1.5 kN lateral load on a rigid surface.

The plot for the lateral displacement as a function of time is displayed in Figure 6-14.

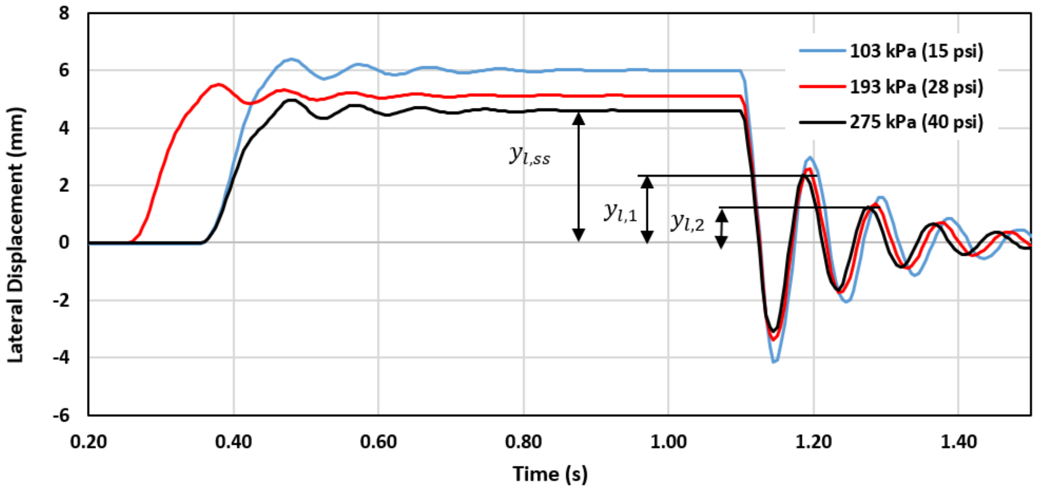

Figure 6-14: HLFS Lateral stiffness test using a vertical load of 9000 N and lateral load of 1500 N.

Using the plots generated for each inflation pressure and vertical load, the maximum steady state lateral displacement and the first and second peak of oscillation is recorded. Equations 6-36 to 6-43 are used to find the lateral stiffness and necessary parameters to needed to calculate the lateral damping constant.

$$k_l = \frac{Lateral\ Force}{Lateral\ Displacement}\ kN/m \tag{6-35}$$

Logarithmic Decrement:

$$\delta = \ln\left(\frac{y_{l,1}}{y_{l,2}}\right) \tag{6-37}$$

Damping Ratio:

$$\xi = \frac{\delta}{\sqrt{4\pi^2+\delta^2}} \tag{6-38}$$

Damped Period of Vibration:

$$\tau_d = t_2 - t_1 \tag{6-39}$$

Un-Damped Lateral Frequency:

$$\omega_n = \frac{2\pi}{\tau_d\sqrt{1-\xi^2}} \qquad 6\text{-}40$$

Damped Lateral Frequency:

$$\omega_d = \frac{2\pi}{\tau_d} \qquad 6\text{-}41$$

Critical Damping Constant:

$$C_c = 2 \cdot m_{wheel} \cdot \omega_n \qquad 6\text{-}42$$

Where m_{wheel} is the mass of the wheel; 67.2 kg.

Lateral Damping Constant:

$$c_l = \xi \cdot C_c \qquad 6\text{-}43$$

Using the above equations, the lateral stiffness, damping and associative parameters are calculated and their data are listed in Table 6-12. Note the steady state lateral displacement is shown in millimeters as to contain as much detail as possible. The lateral stiffness is calculated using displacement in meters.

From Table 6-12, it can be seen that the lateral stiffness is directly proportional to the inflation pressure and the vertical load applied. As the inflation pressure or vertical load increases, the lateral stiffness also increases. For a 3000 N vertical load, as the inflation pressure increases to 193 kPa and 275 kPa, a respective 2.33% and 14.15% increase in lateral stiffness is shown. However, for a 9000 N vertical load, as the inflation pressure is increased to 193 kPa and 275 kPa, the lateral stiffness increases by 17.26% and 11.64% respectively. As inflation pressure is 103 kPa, increasing the vertical load from 3000 N to 6000 N shows an increase of 6.5% in lateral stiffness. Further increase of vertical load to 9000 N shows an increase of 9.2% in lateral stiffness. It also shows that the lateral load does not change the lateral stiffness, since both at both 400 N lateral load (used to validate the tire in Chapter 3) and 1,500 N lateral load, the stiffness is 288 kN/m. The lateral damping constant is has generally increased as the inflation pressure increased and generally decreased as the vertical load was increased. However, the change in the lateral damping constant is not significantly large from the operating conditions.

Table 6-12: Lateral stiffness and damping parameters using a lateral load of 1,500 N.

Parameter	Load (N)	Inflation Pressure (kPa)		
		103	193	275
Steady State Lateral Displacement -$y_{l,ss}$- (mm)	3000	6.980	6.840	5.990
	6000	6.567	5.210	5.175
	9000	6.010	5.122	4.588
Lateral Stiffness - k_l (kN/m)	3000	214.899	219.298	250.417
	6000	228.415	287.913	289.855
	9000	249.584	292.854	326.940
Logarithmic Decrement – δ	3000	0.808	0.819	1.014
	6000	0.771	0.646	0.641
	9000	0.621	0.712	0.644
Damping Ratio – ξ	3000	0.127	0.129	0.159
	6000	0.122	0.102	0.101
	9000	0.098	0.113	0.102
Damped Period of Vibration - τ_d (s)	3000	0.100	0.090	0.100
	6000	0.100	0.090	0.100
	9000	0.090	0.080	0.090
Un-Damped Natural Frequency - ω_d (rad/s)	3000	62.832	69.813	62.832
	6000	62.832	69.813	62.832
	9000	69.813	78.540	69.813
Critical Damping Constant - C_c (kN·s/m)	3000	8.512	9.461	8.553
	6000	8.508	9.432	8.487
	9000	9.428	10.623	9.430
Lateral Damping Constant - c_l (kN·s/m)	3000	1.081	1.220	1.360
	6000	1.038	0.962	0.857
	9000	0.924	1.066	0.962

6.3.4 Lateral Tire Stiffness and Damping Constant in Soil, $k_{l,soil}$ and $c_{l,soil}$

The lateral tire stiffness in soil, $k_{l,soil}$, is calculated by simulating a lateral stiffness test within the Clayey Loam soil. This test procedure is exactly the same as the lateral stiffness test on a rigid surface, except the rigid surface is replaced with the Clayey Loam soil particles. The tire is inflated to the desired inflation pressure and allowed to settle onto the Clayey Loam soil particles using a desired vertical load. Next, a lateral load of 1.5 kN is applied to the spindle of the tire until a steady state lateral displacement is achieved. The lateral force is then released allowing the tire to oscillate about its initial equilibrium position. The lateral stiffness test on Clayey Loam soil may be seen in Figure 6-15.

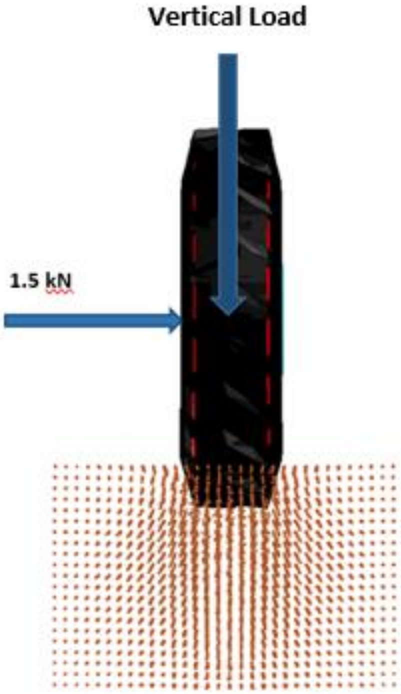

Figure 6-15: Lateral stiffness test on Clayey Loam soil using a lateral force of 1.5 kN.

Similar to previous sections, the plot for the lateral displacement as a function of time is obtained from the simulation results as shown in Figure 6-16. The steady state lateral displacement, first and second peak lateral displacement values are extracted for the variation of inflation pressure and vertical loads. Using these values, the total lateral slip stiffness of the HLFS tire in soil, $k_{l,tot,soil}$, and hence the lateral stiffness of tire on Clayey Loam, $k_{l,,soil}$, may be determined. The first and second subsequent peaks of oscillation in the lateral displacement is used in the lateral damping constants as shown in Figure 6-16.

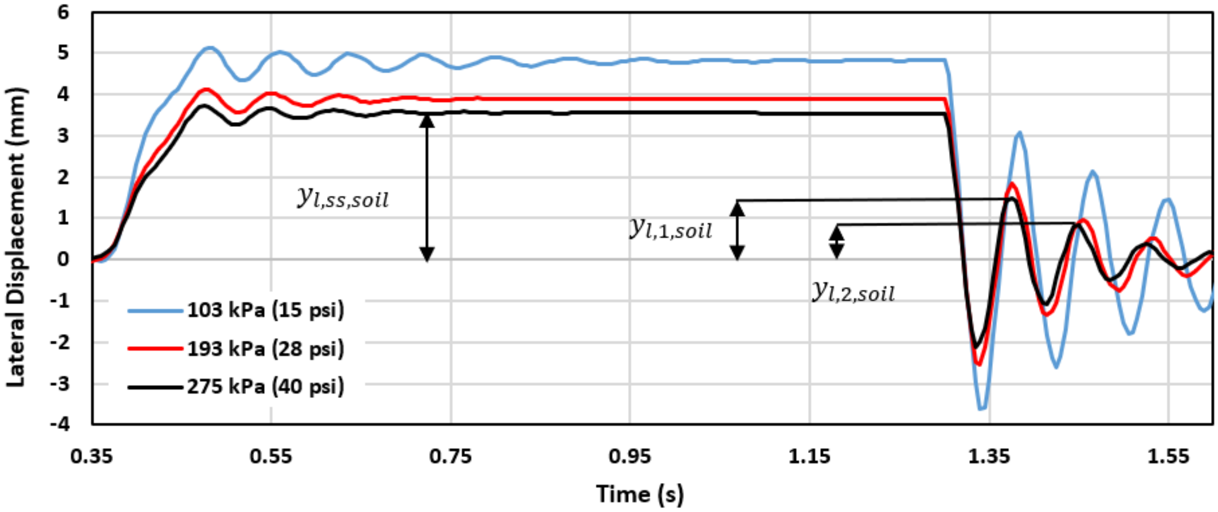

Figure 6-16: HLFS lateral stiffness test using a lateral force of 3000 N.

The total lateral slip stiffness of the HLFS tire on a Clayey Loam soil, lateral stiffness of the HLFS tire on Clayey Loam, and the lateral damping constant on Clayey Loam soil are calculated using Equations 6-44 to 6-51.

The first step in calculations is to determine the total equivalent lateral slip stiffness of the HLFS tire on a Clayey Loam surface. This is done by obtaining the steady state lateral displacement from Figure 6-16 and for each corresponding inflation pressure and vertical load.

$$\frac{1}{k_{l,soil}} = \frac{1}{k_{l,tot,soil}} - \frac{1}{k_l} \qquad \text{6-44}$$

In Equation 6-44, the following variables are used;

$k_{l,tot,soil}$;	Total equivalent lateral slip stiffness of HLFS tire on Clayey Loam soil
k_l;	Lateral tire stiffness on a rigid road
$k_{l,soil}$;	Lateral stiffness on Clayey Loam soil

In order to get the lateral damping constants Equations 6-45 to 6-51 are used as following

Logarithmic Decrement:

$$\delta = \ln\left(\frac{y_{l,1,}}{y_{l,2,}}\right) \qquad \text{6-45}$$

Damping Ratio:

$$\xi = \frac{\delta}{\sqrt{4\pi^2+\delta^2}} \tag{6-46}$$

Damped Period of Vibration:

$$\tau_d = t_2 - t_1 \tag{6-47}$$

Un-Damped Lateral Frequency:

$$\omega_n = \frac{2\pi}{\tau_d\sqrt{1-\xi^2}} \tag{6-48}$$

Damped Lateral Frequency:

$$\omega_d = \frac{2\pi}{\tau_d} \tag{6-49}$$

Critical Damping Constant:

$$C_c = 2 \cdot m_{wheel} \cdot \omega_n \tag{6-50}$$

Where m_{wheel} is the mass of the wheel; 67.2 kg.

Lateral Damping Constant:

$$c_{l,soil} = \xi \cdot C_c \tag{6-51}$$

Table 6-13:Lateral tire stiffness, and damping constant parameters.

Parameter	Load (N)	Inflation Pressure (kPa)		
		103	193	275
Steady State Lateral Displacement -$y_{l,ss}$ (mm)	3000	4.81	3.88	3.54
	6000	4.60	3.57	3.22
	9000	4.46	3.28	2.76
Lateral Slip Stiffness - $k_{l,tot,soil}$ (kN/m)	3000	311.850	386.598	423.729
	6000	326.087	420.168	465.839
	9000	336.322	457.317	543.478
Equivalent Lateral Stiffness, Soil - $k_{l,soil}$ (kN/m)	3000	691.238	506.755	612.242
	6000	762.584	914.686	767.262
	9000	967.784	814.330	820.570
Logarithmic Decrement – δ	3000	0.362	0.720	0.587
	6000	0.379	0.551	0.626
	9000	0.294	0.486	0.597
Damping Ratio – ξ	3000	0.058	0.113	0.093
	6000	0.060	0.087	0.099
	9000	0.047	0.077	0.094
Damped Period of Vibration - τ_d (s)	3000	0.080	0.080	0.080
	6000	0.070	0.070	0.080
	9000	0.080	0.070	0.080
Un-Damped Natural Frequency - ω_n (rad/s)	3000	80.921	83.392	82.486
	6000	92.580	93.940	82.742
	9000	80.453	93.429	82.514
Critical Damping Constant - C_c (kN·s/m)	3000	10.875	11.207	11.087
	6000	12.424	12.625	11.120
	9000	10.812	12.556	11.089
Out of Plane Slip Damping Constant - $c_{l,soil}$ (kN·s/m)	3000	0.631	1.266	1.031
	6000	0.745	1.098	1.101
	9000	0.508	0.967	1.042

It can be seen from table 6-13, that the lateral slip stiffness increased as the inflation pressure and vertical load were increased. For a vertical load of 3000N, as the inflation pressure was increased from 103 kPa to 193 kPa, the lateral slip stiffness increased by 24.11%. As the inflation pressure was further increased to 275 kPa, the lateral slip stiffness increased 9.59%. As the vertical load was increased, a slight increase in lateral slip stiffness was observed for all three inflation pressures. For an inflation pressure of 103 kPa, as the vertical load increased from 3000 N to 6000 N, the lateral slip stiffness increased by 4.8%. Similarly, as the vertical load was increased to 9000 N, the lateral slip stiffness increased by 3.06%. This shows a larger significance the inflation pressure has on the lateral slip stiffness when compared to the vertical load.

The equivalent lateral tire stiffnesses are higher in value than the lateral tire stiffnesses in all the operating conditions. Similarly, in most cases, as the vertical load is increased, the equivalent lateral stiffness increases. However, the inflation pressure does not influence the equivalent lateral stiffness as much. The lateral damping constant has shown a general increase as the inflation pressure increases. For a vertical load of 3000 N, as the inflation pressure increases from 103 kPa to 193 kPa, the lateral slip damping constant increases from 0.631 kNs/m to 1.266 kNs/m. However, as the inflation pressure is increased to 275 kPa, the damping constant decreases from 1.266 kNs/m to 1.031 kPa. This trend is only true for the 3000 N load. For 6000 N and 9000 N vertical loads, the damping constant increased as the inflation pressure increased.

6.3.5 Steering Characteristics on Clayey Loam Soil, $k_{f,soil}$

In order to study the steering characteristics of the HLFS agricultural tire on a Clayey Loam soil, a steady state steering procedure is conducted. The cornering stiffness is calculated from this procedure shown in Figure 6-17. The tire is inflated to inflation pressures of 103 kPa (15 psi), 193 kPa (28 psi) and 275 kPa (40 psi); vertical loads of 3 kN, 6 kN, and 9 kN. The tire is then steered to angles of 0, 1, 2, 4, 6, 8, 10 and 12 degrees from the longitudinal axis in several simulations. The tire is then given a linear tire velocity of 10 km/h in the longitudinal axis, while the tire is constrained to roll in the longitudinal axis. This allows for having a slip angle during the whole simulation. The lateral and longitudinal force at the tire-soil contact are obtained from the simulation results. The slope of the cornering force as a function of slip angle curve is considered to be the steering stiffness on Clayey Loam soil.

The plot for the cornering force as a function of slip angle is shown in Figure 6-18. The slope of the curve is determined for slip angles of 0-12 degrees and is described in Equation 6-52. The slip angle is the angle between the direction of wheel travel and the longitudinal axis of the tire as shown in Figure 6-17.

$$k_{f,soil} = \frac{\partial F_{y,soil}}{\partial \alpha_{soil}} |_{a=0} \qquad 6\text{-}52$$

Where $F_{y,soil}$, is the lateral force felt at the tire spindle;

α_{soil}, is the slip angle in radians

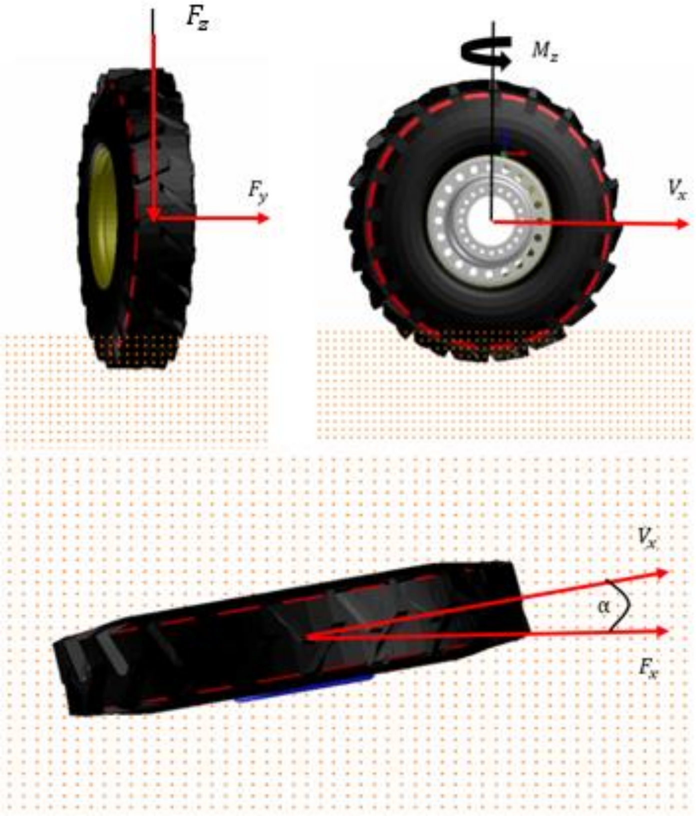

Figure 6-17: HLFS tire cornering stiffness test on Clayey Loam SPH soil

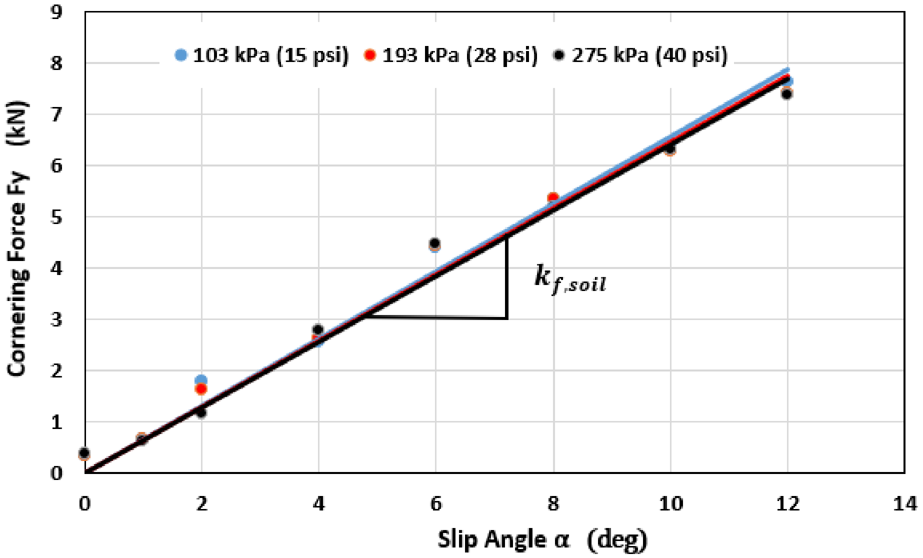

Figure 6-18: Cornering force as a function of slip angle at 9 kN vertical load.

Table 6-14 consists of the cornering stiffness values for the three inflation pressures and three vertical loads the simulation was conducted for. It can be seen that as the inflation pressure increased, there is not much correlation to the vertical stiffness. A slight decrease in cornering stiffness is seen with the increase of inflation pressure. However, as the vertical load is increased, the cornering stiffness increases considerably. Increasing the vertical load from 3000N to 6000 N shows an increase of 53% in cornering stiffness. Furthermore, increasing the vertical load from 6000 N to 9000 N, showed an increase of 42.19% in cornering stiffness. The effect of changing the inflation pressure on the cornering stiffness is minimal for all three vertical loads.

Table 6-14: Cornering stiffness on Clayey Loam.

		Inflation Pressure (kPa)		
Parameter	Load (N)	103	193	275
Cornering Stiffness $k_{f,soil}$ (kN/rad)	3000	17.690	16.660	16.100
	6000	26.482	27.043	28.494
	9000	37.655	37.047	36.824

6.3.6 Self-Aligning Moment Stiffness on Clayey Loam, $k_{M,soil}$

The self-aligning moment stiffness, $k_{M,soil}$, is described as the slope of the aligning moment $M_{z,soil}$ as a function of slip angle plot as shown in Figure 6-19 and Figure 6-17. The procedure for obtaining the self aligning moment is the same as the steering characteristics described in the previous section. The aligning moment about the z-axis is obtained from the simulation results for each corresponding slip angle, inflation pressure and vertical load. The self-aligning moment stiffness formula is shown in Equation 6-53.

$$k_{M,soil} = \frac{\partial\, M_{z,soil}}{\partial \alpha_{soil}}|_{\alpha=0} \qquad 6\text{-}53$$

Where, $M_{z,soil}$, is the aligning moment obtained from simulations in kN·m

α_{soil}, is the slip angle in radians.

A plot for the self-aligning moment as a function of slip angle for inflation pressures of 103 kPa, 193 kPa and 275 kPa, and a vertical load of 9 kN is shown in Figure 6-20. A table with the self-aligning stiffness values for the three inflation pressures and three vertical loads are shown in Table 6-15

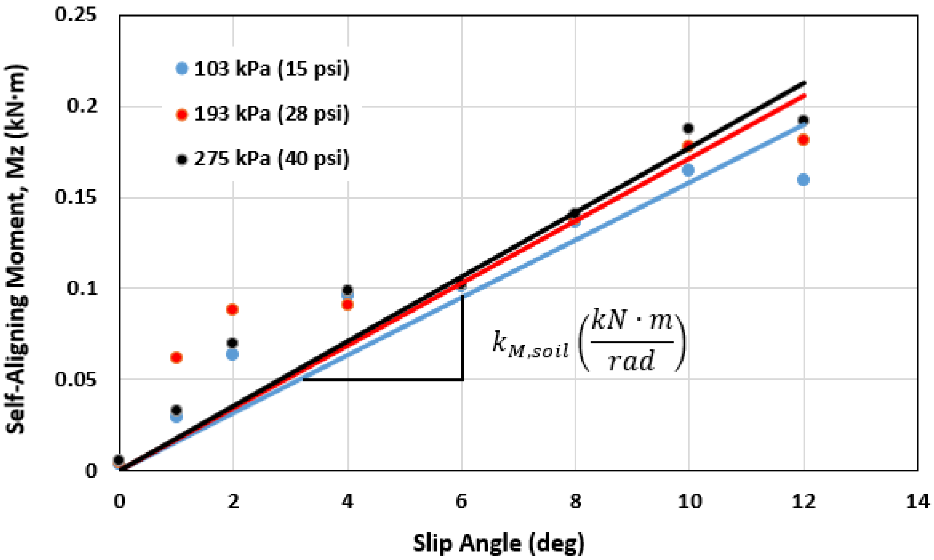

Figure 6-19: HLFS self-aligning moment as a function of slip angle using a 9 kN vertical load.

Table 6-15: HLFS self-aligning moment stiffness on Clayey Loam soil.

		Inflation Pressure (kPa)		
Parameter	Load (N)	103	193	275
Self-Aligning Moment Stiffness - $k_{M,soil}$ (kN·m/rad)	3000	0.556	0.590	0.595
	6000	0.756	0.733	0.785
	9000	0.911	0.985	1.020

From Table 6-15, it can be seen that as the inflation pressure increases, the self-aligning moment stiffness also increases a very small amount and for most vertical loads. As the vertical load is increased, the self-aligning moment stiffness is increased considerably. This makes sense as the tire is facing more longitudinal and lateral force with higher vertical loads. As a result, the self-aligning moment increases which ultimately increases the self-aligning moment stiffness. It can also be seen from Figure 6-19, as the slip angle is increased, the self-aligning moment produced about the z-axis increases.

6.3.7 Relaxation Length on Clayey Loam, σ_{soil}

This section outlines the relaxation length of the tire when undergoing cornering. The relaxation length describes the translational length the HLFS tire travels in order to overcome the resistive forces that is applied to the tire before it has reached steady state cornering in soil. The relaxation length, σ_{soil}, is the ratio between the cornering stiffness, $k_{f,soil}$, and the total equivalent lateral stiffness, $k_{l,tot,soil}$ as seen in Equation 6-54. The details behind the methods and results for $k_{f,soil}$ and $k_{l,tot,soil}$ may be found in sections 6.3.5 and 6.3.4.

$$\sigma_{soil} = \frac{k_{f,soil}}{k_{l,tot,soil}}\ m \qquad \text{6-54}$$

Table 6-16: HLFS tire's relaxation length on Clayey Loam soil.

		Inflation Pressure (kPa)		
Parameter	Load (N)	103	193	275
Relaxation Length – σ_{soil} (m)	3000	0.057	0.043	0.038
	6000	0.081	0.064	0.061
	9000	0.112	0.081	0.068

Table 6-16 shows the relaxation length on Clayey Loam soil for three inflation pressure and three vertical loads. It shows that the length the tire needs to travel before it reaches steady state cornering forces increases as the vertical load increases. The increase seems to have a very linear trend for inflation pressures of 103 kPa and 193 kPa. As the inflation pressure increases, the relaxation length decreases.

6.3.8 Rolling Resistance Coefficient on Clayey Loam soil, RRC_{soil}

This section covers the prediction of the rolling resistance coefficient (RRC) of the HLFS tire on a Clayey Loam soil. The section has the RRC on Clayey Loam for inflation pressures of 103 kPa (15 psi), 193 kPa (28 psi), 275 kPa (40 psi) for vertical loads of 2 kN, 3 kN and 4 kN. In addition, the tire pass over the soil three times in order to obtain the results for multi pass rolling resistance coefficient. The reason for predicting the RRC for lower loads is because of available experimental data for vertical loads of 2 kN, 3 kN and 4 kN, the earlier stated inflation pressures and three passes of tire on the Clayey Loam soil. In addition, the original loads of 3 kN, 6 kN and 9 kN will also be used to predict the RRC for a single pass of tire on the SPH soil.

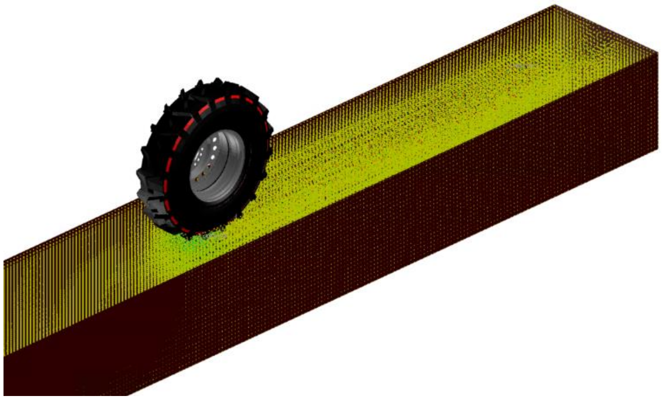

Figure 6-20: Rolling resistance test on Clayey Loam soil for a single inflation pressure and vertical load.

The rolling resistance test shown in Figure 6-20 is conducted by allowing the HLFS tire to free roll on the Clayey Loam soil at a speed of 1 m/s. The tire is inflated to the desired inflation pressure then the desired vertical load is applied. Next, a given constant velocity in the longitudinal axis (x-axis) is applied to the center of the tire. The force resisting the tire's motion, F_x, and the vertical load on the tire, F_z at the contact patch are obtained from the simulation output. The rolling resistance coefficient is calculated using the steady state average of the resistive and vertical forces as shown in Equation 6-55.

$$RRC_{soil} = \frac{F_x}{F_z} \qquad 6\text{-}55$$

The results for the rolling resistance coefficient on Clayey Loam for a single tire pass, vertical load of 103 kPa, 193 kPa, 275 kPa and vertical loads of 3 kN, 6 kN and 9 kN are presented in Table 6-17 and Figure 6-21.

Table 6-17: Rolling resistance coefficient for a single HLFS tire on Clayey Loam soil.

		Inflation Pressure (kPa)		
Parameter	Load (N)	103	193	275
Rolling Resistance Coefficient RRC_{soil}	3000	0.199	0.196	0.190
	6000	0.244	0.238	0.226
	9000	0.310	0.266	0.271

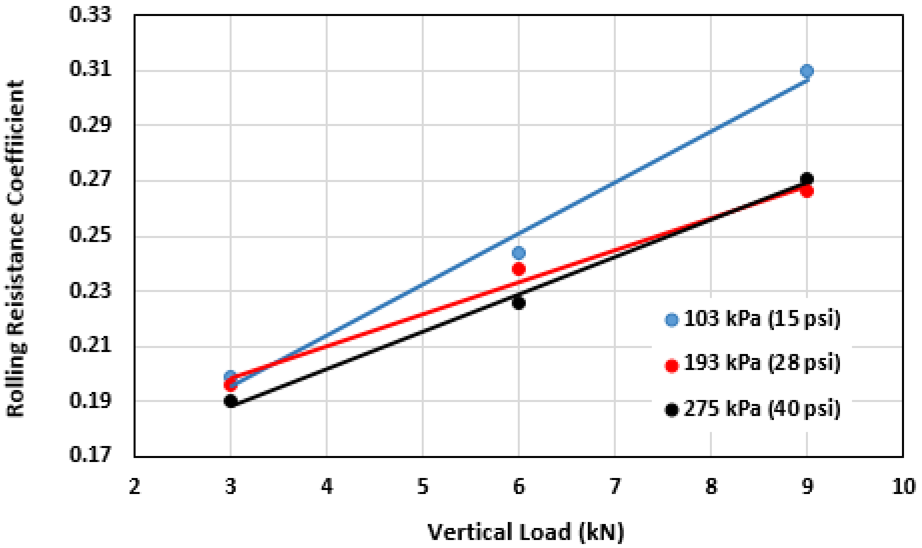

Figure 6-21: Rolling resistance coefficient for a single tire pass.

The results show that the rolling resistance increases as the vertical load is increasing. A larger increase is seen in low inflation pressures. This is because the tire is under inflated and more resistance is present during free rolling. As the inflation pressure increases, the rolling resistance coefficient decreases. The decreases in RRC is really shown in higher vertical loads, as the inflation pressure is increased from under inflation (103 kPa or 15psi) to over inflation (275 kPa or 40 psi).

Next the effect of multi pass of the HLFS tire on the Clayey Loam soil using a nominal inflation pressure of 193 kPa (28 psi) and vertical loads of 2 kN, 3 kN and 4 kN are investigated and summarized in Table 6-18.

Table 6-18: Rolling resistance coefficient for three passes of HLFS tire on Clayey Loam soil.

	Pass 1 RRC		Pass 2 RRC		Pass 3 RRC	
Load (N)	Simulated	Measured	Simulated	Measured	Simulated	Measured
2000	0.177	0.181	0.131	0.170	0.130	0.155
3000	0.190	0.140	0.129	0.136	0.093	0.126
4000	0.208	0.195	0.127	0.175	0.098	0.110

The first pass shows that as the vertical load is increased, the rolling resistance increases for both measured and simulated data. This is because the soil is fresh and untouched and will cause higher longitudinal resistance at higher loads. During the second pass, the soil has gone some compaction and as a result, both the measured and simulated data do not show much increase in RRC as the vertical load has increased. In the third pass, the soil has been really compacted and show harder soil characteristics. As the vertical load is increased, the rolling resistance has decreased. This is due to the compaction of the soil at higher loads and less resistance for the tire to roll freely.

The results for the out-of-plane off-road rigid ring parameters are found in Table 6-19 to Table 6-21 for vertical loads of 3000 N, 6000 N, and 9000 N respectively.

Table 6-19: Out-of-plane off-road rigid ring parameters for a vertical load of 3000 N.

Out-of-plane Off-road Rigid Ring Parameters for 3000 N Load	**103 kpa**	**193 kPa**	**275 kPa**
Translational Stiffness k_{by} (kN/m)	937.500	1,250.000	1,666.666
Translational Damping Constant c_{by} (kN.s/m)	1.120	1.437	0.788
Rotational Stiffness $k_{b\gamma}$ (kN.m/rad)	185.294	206.557	222.615
Rotational Damping Constant $c_{b\gamma}$ (kN.m.s/rad)	0.018	0.148	0.053
Lateral Tire Stiffness k_l (kN/m)	214.899	219.298	250.417
Lateral Damping Constant c_l (kN.s/m)	1.081	1.220	1.360
Total Lateral Slip Stiffness, Soil $k_{l,tot,\text{soil}}$ (kN/m)	311.850	386.598	423.729
Lateral Slip Stiffness, Dry Sand $k_{l,\text{soil}}$ (kN/m)	691.238	506.755	612.242
Lateral Damping Constant, Soil $c_{l,\text{soil}}$ - (kN.s/m)	0.631	1.266	1.031
Cornering Stiffness, Soil $k_{f,\text{soil}}$ (kN/rad)	17.690	16.660	16.100
Self-Aligning Torque Stiffness, Soil $k_{M,Dry\ Sand}$ – (kN.m/rad)	0.556	0.590	0.595
Relaxation Length, Dry Sand - $\sigma_{,\text{soil}}$ (m)	0.057	0.043	0.038
Rolling Resistance Coefficient, Soil	0.199	0.196	0.190

Table 6-20: Out-of-plane off-road rigid ring parameters for a vertical load of 6000 N.

Out-of-plane Off-road Rigid Ring Parameters for 6000 N Load	**103 kpa**	**193 kPa**	**275 kPa**
Translational Stiffness k_{by} (kN/m)	937.500	1,250.000	1,666.666
Translational Damping Constant c_{by} (kN.s/m)	1.120	1.437	0.788
Rotational Stiffness $k_{b\gamma}$ (kN.m/rad)	185.294	206.557	222.615
Rotational Damping Constant $c_{b\gamma}$ (kN.m.s/rad)	0.018	0.148	0.053
Lateral Tire Stiffness k_l (kN/m)	228.415	287.913	289.855
Lateral Damping Constant c_l (kN.s/m)	1.038	0.962	0.857
Total Lateral Slip Stiffness, Soil $k_{l,tot,\text{soil}}$ (kN/m)	326.087	420.168	465.839
Lateral Slip Stiffness, Dry Sand $k_{l,\text{soil}}$ (kN/m)	762.584	914.686	767.262
Lateral Damping Constant, Soil $c_{l,\text{soil}}$ - (kN.s/m)	0.745	1.098	1.101
Cornering Stiffness, Soil $k_{f,\text{soil}}$ (kN/rad)	26.482	27.043	28.494
Self-Aligning Torque Stiffness, Soil $k_{M,Dry\ Sand}$ – (kN.m/rad)	0.756	0.733	0.785
Relaxation Length, Dry Sand - $\sigma_{,\text{soil}}$ (m)	0.081	0.064	0.061
Rolling Resistance Coefficient, Soil	0.244	0.238	0.226

Table 6-21: Out-of-plane off-road rigid ring parameters for a vertical load of 9000 N.

Out-of-plane Off-road Rigid Ring Parameters for 9000 N Load	**103 kpa**	**193 kPa**	**275 kPa**
Translational Stiffness k_{by} (kN/m)	937.500	1,250.000	1,666.666
Translational Damping Constant c_{by} (kN.s/m)	1.120	1.437	0.788
Rotational Stiffness $k_{b\gamma}$ (kN.m/rad)	185.294	206.557	222.615
Rotational Damping Constant $c_{b\gamma}$ (kN.m.s/rad)	0.018	0.148	0.053
Lateral Tire Stiffness k_l (kN/m)	249.584	292.854	326.940
Lateral Damping Constant c_l (kN.s/m)	0.924	1.066	0.962
Total Lateral Slip Stiffness, Soil $k_{l,tot,\text{soil}}$ (kN/m)	336.322	457.317	543.478
Lateral Slip Stiffness, Dry Sand $k_{l,\text{soil}}$ (kN/m)	967.784	814.330	820.570
Lateral Damping Constant, Soil $c_{l,\text{soil}}$ - (kN.s/m)	0.508	0.967	1.042
Cornering Stiffness, Soil $k_{f,\text{soil}}$ (kN/rad)	37.655	37.047	36.824
Self-Aligning Torque Stiffness, Soil $k_{M,Dry\ Sand}$ – (kN.m/rad)	0.911	0.985	1.020
Relaxation Length, Dry Sand - $\sigma_{,\text{soil}}$ (m)	0.112	0.081	0.068
Rolling Resistance Coefficient, Soil	0.310	0.266	0.271

6.4 Chapter Summary

This chapter includes the determination of the in-plane and out-of-plane off-road rigid ring model's parameters for the HLFS agricultural tire and clayey-loam soil interaction model. The parameters are calculated for several different operation conditions. The conditions include three vertical loads of 3000N , 6000 N and 9000 N; and inflation pressures of 103 kPa, 193 kPa and 275 kPa. These conditions are chosen based on nominal inflation pressures (193 kPa), under inflation (103 kPa) and over inflation (275 kPa).

The in-plane rigid ring parameters include the vertical stiffness, k_{bz}, residual vertical stiffness, k_{vr}, vertical sidewall damping constant, c_{bz}, residual damping constant, c_{vr}. In this study, the first mode frequency for the three loads and inflation pressures are calculated. It is found that the first mode of vibration frequency increases as the inflation pressure is increased. The effect of increasing the vertical load has minimal effect on the first mode of vibration frequency. The sidewall vertical stiffness is proportional to the inflation pressure. As the inflation pressure increased, the sidewall vertical stiffness also increased. The residual vertical stiffness shows an increase as the inflation pressure is increased from 193 kPa to 275 kPa. On the other hand, as the inflation pressure in increased from 103 kPa to 193 kPa, there is a decrease in the residual vertical stiffness. In terms of damping constants, the vertical sidewall damping constant increased as both the inflation pressure and the vertical load increased. The residual damping constant shows a general decrease as the inflation pressure increases. Lastly, the total tire damping constant shows an increase as the inflation pressure and the vertical load is increased.

To further investigate the in plane rigid ring parameters, the rotational tire stiffness and damping constant were found. This studies the stiffness and damping of the tire about the lateral axis when a rotational force is applied. The rotational stiffness and damping constant were obtained for inflation pressure of 103 kPa, 193 kPa and 275 kPa. The results show that the rotational ' are very large as the tire rubber material is very stiff. As the inflation pressure increased, there is a slight increase in rotational stiffness and damping constant. The change in the stiffness and damping constant for rotational motion does not change significantly with increase of inflation pressure.

To further add to the rigid ring model, the total equivalent vertical stiffness with the effect of the soil is also investigated. The total vertical stiffness includes the soil as a series spring in addition to the previously found vertical stiffness on a rigid surface. First, the vertical stiffness of the soil is obtained. The soil stiffness increases proportionally to the vertical load. It was found that the inflation pressure does not cause any significant change in the soil's vertical stiffness.

The last parameters needed to complete the off-road in-plane rigid ring parameters is the longitudinal tire stiffness and damping. This acts as a spring positioned between the tire and a surface. It models the forces felt while the tire is undergoing braking or acceleration. The tire is given 100% slip conditions on the Clayey Loam soil and rolled until there is complete traction between the tire and soil. From this procedure, the longitudinal tire stiffness and the longitudinal tread stiffness are calculated. It was found that for both the stiffness', as the inflation pressure and the vertical load increases, the stiffness' also increase. Although a higher increase in stiffness is found as the vertical load is increased. In terms of damping, as the vertical load is increased the damping is also increased. The effect of inflation pressure has minimum effect on the damping constant.

Now that the in-plane rigid ring parameters are fully obtained, the out-of-plane rigid ring parameters are to be found, as shown in section 6.3. This ensures we know the tire's response to stimuli from an outer plane. Once again, the same operating conditions are used as the in-plane simulations.

The first out-of-plane rigid ring parameters obtained are the translational stiffness and damping constants. This simulation studies the tire's resistivity to a lateral load applied to the tire's top and bottom portion of the tread. The HLFS tire is constrained to move only in the lateral direction as a 15,000 N load is applied to the top and bottom nodes on the tread. Once the load is released, the steady state displacement, translational sidewall stiffness and the translational damping constant is calculated. As expected, the translational sidewall stiffness increases as the inflation pressure is increased from 103 kPa to 275 kPa. The translational damping constant shows an increase as the inflation pressure is increased from 103 kPa to 193 kPa. However, this constant shows a decrease, as the inflation pressure is increased from 193 kPa to 275 kPa.

Next, the rotational stiffness and damping constant for the out-of-plane rigid ring model is studied. The rotational motion of the tire about the longitudinal axis is expressed as rotational spring and damper system as seen in section 6.3.2. The rotational stiffness shows increases as the inflation pressure increases. The damping constant however increases as the inflation pressure is increased from 103 kPa to 193 kPa; and decreases as the inflation pressure is increased from 193 kPa to 275 kPa.

Another out-of-plane rigid ring parameter is the lateral tire stiffness and damping constant. This simulation procedure is conducted by applying a lateral force to the tire's spindle while the tire is placed on a rigid surface. The stiffness and damping parameter is obtained for the three inflation pressures and three vertical loads. The results show that as the inflation pressure is increasing, the lateral stiffness also increases. Similarly, as the vertical load on the tire is increased, the lateral stiffness also increases. The damping constant generally shows an increase as the inflation pressure is increased. The damping constant shows a decrease as the vertical load is increased.

The out-of-plane rigid ring parameters found are the lateral tire stiffness and damping constant in the Clayey Loam soil. This procedure is similar to the lateral tire stiffness and damping constant shown earlier, with an exception of changing the rigid road surface to the Clayey Loam soil. The lateral slip stiffness of the tire within the soil particles show an increase as the inflation pressure and the vertical load increases. The lateral stiffness of the soil by itself shows an increase as the vertical load is increased. The inflation pressure also has a direct effect on the lateral damping constant. As the inflation pressure increases, the lateral damping constant also increases. In terms of increasing vertical load, the lateral damping constant generally decreases.

That concludes the out-of-plane off-road rigid ring model parameters for the HLFS tire on a Clayey Loam soil. With both the in-plane and out-of-plane off-road rigid ring parameters, the tire's response to many driving conditions are successfully predicted.

The steering characteristics of the HLFS tire on Clayey Loam soil is conducted next. The tire's changing operating conditions include the inflation pressure and vertical load as shown earlier. The HLFS tire is steered at angles ranging from 0 – 12 degrees from the longitudinal axis and given a linear tire velocity of 10 km/h. The tire's constraint to roll in the longitudinal axis depicts having a constant slip angle during the whole simulation. Using a vertical force of 9 kN, the cornering force is shown to increase linearly with the slip angle. The change in cornering force is not significant with change of inflation pressure. The cornering stiffness has increased as the vertical load increases. However, as the inflation pressure increases, the cornering stiffness does not change as much. The self-aligning moment shows an increase as the vertical load is increased. Increasing inflation pressure has minimal effect on the self-aligning moment.

The relaxation length, or the translational length the HLFS tire travels in order to overcome resistive forces is also found using the steering procedure mentioned earlier. The relaxation length decreases as the inflation pressure increases. It increases as the vertical load is increased.

The last part of this chapter studies the rolling resistance coefficient of the HLFS tire on the Clayey Loam soil. For this section, there were also experimental results obtained from Azar from Urmia University in Iran. This simulation was conducted for inflation pressures of 103kPa, 193 kPa and 275 kPa, and vertical loads of 2 kN, 3 kN, and 4 kN. To study compaction, the tire is also allowed for multi-pass on the Clayey Loam soil. The results show that as the vertical load is increased, the rolling resistance coefficient also increases. This is expected as the tire sinks deeper into the soil and therefore causing a higher resistive force in the rolling motion. On the contrary, as the inflation pressure is increased, the rolling resistance decreases. This is also expected from previous studies as inflating the tire more gives a stiffer tire and easier to roll over the Clayey Loam soil. The results in Figure 6-22 show that the fit between the measured and simulated RRC show good agreement. The first pass shows that as the vertical load is increased, the rolling resistance increases for both measured and simulated data. This is because the soil is fresh and untouched and will cause higher longitudinal resistance at higher loads. During the second pass, the soil has gone some compaction and as a result, both the measured and simulated data do not show much increase in RRC as the vertical load has increased. In the third pass, the soil has been really compacted and show harder soil characteristics. As the vertical load is increased, the rolling resistance has decreased. This is due to the compaction of the soil at higher loads and less resistance for the tire to roll freely.

In conclusion, the prediction of the off-road rigid ring parameters for the HLFS tire on a rigid surface and a Clayey Loam soil has been successful. The available experimental data have been very accurate with similar trends as validated in the simulations. The rigid ring parameters, steering characteristics, rolling resistance, self-aligning moment have been accurately represented by virtual simulations.

CHAPTER 7 - CONCLUSION AND FUTURE WORK

7.1 Conclusions

This thesis utilizes Finite Element Analysis method to model and validate the High Lug Farm Service (HLFS) agricultural tire sized 220/70B16 from Barez Tire. The tire is modelled and validated using ESI Visual Environment's PAM-Crash software. This software allows for simulations within a time domain and can output the tire's response to various loading in static and dynamic simulations. Once the tire is validated against limited experimental results obtained from Urmia University in Iran, it may be analyzed on rigid surfaces and terrains such as soil and sand found in agricultural and off-road applications. As a result, two terrains (Clayey Loam and LETE Sand) have been modelled using Smoothed-Particle Hydrodynamic technique. This technique has been recently used in many off-road tire-terrain applications for non agricultural applications. The modelled soil is calibrated against experimental data and theoretical values obtained from published data. The study of using an agricultural tire along with SPH tire is a new field that has not been explored extensively.

Upon validating the tire and two terrain models, static and dynamic tests are conducted in order to study the HLFS's response to loading and driving conditions. The analysis of soil dynamics and stress distribution within different soil depths are studied for varying operating conditions. Lastly, the in-plane and out-of-plane off-road rigid ring model will be used to model the tire as translational and rotational spring and damper systems. This model has many parameters that describe the physical response from the tire under various loading. The use of simulations and loading through FEA and the tire's output are used to obtain and predict these parameters.

The major work and findings of the thesis research are as follows:

1. The HLFS tire model has been created with accurate resemblance and dimensions of the actual tire created by Barez Tire. The agricultural tire is modelled using a combination of Mooney-Rivlin solid elements for the tread, under tread, shoulder and sidewall of the tire. Membrane elements are used for sidewall and plies within the tire. The beads running through the tire are modelled using beam elements. Lastly, a rim is created using shell elements. A section cut consisting the HLFS tire's parts and geometry may be found in Chapter 3. The tire model is validated against the tire

characteristics provided by the manufacturer. Theses tests include a vertical stiffness, lateral stiffness and longitudinal stiffness of the tire. The experimental and simulated vertical stiffness were found to be 250 N/mm, and 422 N/mm respectively. The experimental lateral stiffness was 305 N/mm while the simulated lateral stiffness was 288 N/mm. Lastly, the measured longitudinal stiffness was found to be 302 N/mm and the simulated longitudinal stiffness was 300 N/mm. Next a drum-cleat test was performed where the tire is placed down on a rolling-drum-cleat. Using the vertical forces obtained from the output file and employing the fast fourier transform; vertical force as a function of frequency was obtained. This gave us the second peak of vertical forces corresponding to the first mode of vibration (82 Hz). This frequency shows good agreement for first mode of vibrations found for larger tires in trucks and other agricultural machinery. Based on this frequency, the sidewall damping coefficient of 51.5 was calculated. A sensitivity analysis for the damping coefficients obtained from the drum-cleat test was also performed. The operating conditions were varied by changing the cleat's rotational speed from 5.55 rad/s to 11.11 rad/s; and using inflation pressures of 103 kPa, 193 kPa and 275 kPa. The result show that using a rotational speed of 11.1 rad/s showed minimal change in damping coefficient (around 52) as the inflation pressures were changed. However, using a rotational speed of 5.55 rad/s resulted in a smaller damping coefficient (28) for 103 kPa inflation pressure.

2. A Clayey Loam soil and LETE sand material is also modelled and calibrated using PAM-Crash software. The soil particles are modelled using the Smoothed-Particle Hydrodynamics technique instead of FEA mesh elements. Two tests as described by Wong [72] as the pressure sinkage and shear strength test are conducted. The simulations results are compared to experimental published data available for the two terrains. A plate's sinkage and shearing in the soil outputs the plate displacement and shear strength as a function of inflation pressures of (0 kpa,10 kPa,50 kPa,100 kPa,150 kPa and 200 kPa). Varying the soil's material properties, the soil and sand model are calibrated to match those found in literature. Next, the SPH soil's sensitivity analysis is conducted for LETE sand. Lastly, study includes changing the part card parameters and mesh size for the LETE sand models and its effect on the plate displacement, cohesion and angle of internal shearing resistance. The parameters changed include the particle "Smoothing Length to Radius" ratio, maximum smoothing length, Alphamg (first parameter for the artificial viscosity, and ETA (anti-crossing force parameter).

3. This thesis also studies the soil stress distribution for a Clayey Loam soil and LETE sand terrain found in many off-road applications. The previously modelled HLFS tire and two terrains are used in PAM-Crash's simulations. The tire with an inflation pressure of 193 kPa is rolled over a box of SPH particles with a vertical load of 2 kN. Experimental stress results for this procedure were available for a soil depth of 200 mm. It was found that for this soil depth the forces found in the soil showed great accuracy between the experimental and simulated data. The maximum stress at a 200 mm depth for experimental and simulations were 16.592 and 16.477 respectively; with a percent error of 0.69%. The simulation was repeated for soil depths of 100mm, 200 mm, 300 mm and 400 mm. The simulated results show that as the soil depth increase, there is less force and therefore less stress transferred to lower depths. This is found for both the Clayey Loam and LETE sand terrain. It is also found that the forces transferred to the LETE sand particles are much higher at all the depths when compare to Clayey Loam. The effect of changing tire velocity in the simulations was also conducted. It showed that increasing tire velocity has a significant impact on the stress distribution at a soil depth of 200 mm. The greater difference in stress distribution is found between a tire velocity of 1 m/s and 1.5 m/s.

4. Determination of the in-plane and out-of-plane off-road rigid ring model's parameters for the HLFS agricultural tire and clayey-loam soil interaction model. The parameters are calculated for several different operation conditions. These include three vertical loads of 3000N, 6000 N and 9000 N; and inflation pressures of 103 kPa, 193 kPa and 275 kPa. These conditions are chosen based on nominal inflation pressures, (193 kPa), under inflation (103 kPa) and over inflation (275 kPa).
    - The first mode frequency for the three loads and inflation pressures are calculated. It is found that the first mode of vibration frequency increases as the inflation pressure is increased. The effect of increasing the vertical load has minimal effect on the first mode of vibration frequency.
    - The in-plane off-road rigid ring parameters were obtained. The sidewall vertical stiffness is proportional to the inflation pressure. As the inflation pressure increased, the sidewall vertical stiffness also increased. In terms of damping constants, the vertical sidewall damping constant increased as both the inflation pressure and the vertical load increased. The residual damping constant shows a general decrease as the inflation pressure increases. The total tire damping constant shows an increase as the inflation pressure and the vertical load is increased. As the inflation pressure increased, there is a slight increase in rotational

stiffness and damping constant. The change in the stiffness and damping constant for rotational motion does not change significantly with increase of inflation pressure.

- The soil stiffness increases proportionally to the vertical load. It was found that the inflation pressure does not cause any significant change in the soil's vertical stiffness.

5. The out-of-plane rigid ring parameters are to be found, as shown in section 6.3. Once again, the same operating conditions are used as the in-plane simulations.

    - The translational sidewall stiffness increases as the inflation pressure is increased from 103 kPa to 275 kPa. The translational damping constant shows an increase as the inflation pressure is increased from 103 kPa to 193 kPa. However, this constant shows a decrease, as the inflation pressure is increased from 193 kPa to 275 kPa.
    - The rotational stiffness shows increase as the inflation pressure increases. The damping constant however increases as the inflation pressure is increased from 103 kPa to 193 kPa; and decreases as the inflation pressure is increased from 193 kPa to 275 kPa.
    - The results show that as the inflation pressure is increasing, the lateral stiffness also increases. Similarly, as the vertical load on the tire is increased, the lateral stiffness also increases. The damping constant generally shows an increase as the inflation pressure is increased. The damping constant shows a decrease as the vertical load is increased.
    - The lateral slip stiffness of the tire within the soil particles show an increase as the inflation pressure and the vertical load increases. The lateral stiffness of the soil by itself shows an increase as the vertical load is increased. The inflation pressure also has a direct effect on the lateral damping constant. As the inflation pressure increases, the lateral damping constant also increases. In terms of increasing vertical load, the lateral damping constant generally decreases.

6. The steering characteristics of the HLFS tire on Clayey Loam soil is conducted. The tire's changing operating conditions include the inflation pressure and vertical load as shown earlier. Using a vertical force of 9 kN, the cornering force is shown to increase linearly with the slip angle. The change in cornering force is not significant with change of inflation pressure. The cornering stiffness has increased as the vertical load increases. However, as the inflation pressure increases, the cornering stiffness does not change as much. The self-aligning moment shows an increase as the vertical load is increased. Increasing inflation pressure has minimal effect on the self-aligning

moment. The relaxation length, or the translational length the HLFS tire travels in order to overcome resistive forces is also found using the steering procedure mentioned earlier. The relaxation length decreases as the inflation pressure increases. It increases as the vertical load is increased.

7. The rolling resistance coefficient of the HLFS tire on the Clayey Loam soil was obtained. For this section, there were also experimental results obtained from Azar from Urmia University in Iran. This simulation was conducted for inflation pressures of 103kPa, 193 kPa and 275 kPa, and vertical loads of 2 kN, 3 kN, and 4 kN. To study compaction, the tire is also allowed for multi-pass on the Clayey Loam soil. The results show that as the vertical load is increased, the rolling resistance coefficient also increases. On the contrary, as the inflation pressure is increased, the rolling resistance decreases. The results show that the fit between the measured and simulated RRC show good agreement. The first pass shows that as the vertical load is increased, the rolling resistance increases for both measured and simulated data. This is because the soil is fresh and untouched and will cause higher longitudinal resistance at higher loads. During the second pass, the soil has gone some compaction and as a result, both the measured and simulated data do not show much increase in RRC as the vertical load has increased. In the third pass, the soil has been really compacted and show harder soil characteristics. As the vertical load is increased, the rolling resistance has decreased. This is due to the compaction of the soil at higher loads and less resistance for the tire to roll freely.

7.2 Future Work and Recommendations

There are many future research studies that may be carried out on the current HLFS tire and Clayey Loam soil model. The study of tire and soil dynamics is a vast topic that may be studied in order to reduce cost and learn vehicle dynamics.

The work done currently may be conducted on different terrains including snow and clay. New terrains may be calibrated and validated against experimental data. These new models may be used in conjunction with the HLFS tire to study soil and tire dynamics. In addition, the current terrain models may be used for other tire models used in off-road operations. The moisture content may be increased as the current research is conducted for dry terrains. The effect of hydroplaning and the agricultural tire running on flooded surfaces can also be researched. The change of vertical force, lateral force, multi-pass and steering characteristics may also be further researched in order to get more accurate results. Experimental procedures analogous to the simulations conducted within this thesis may be done in order to validate the simulation accuracy.

The off-road rigid ring parameters may be used in full vehicle agricultural vehicle models for further implementation and research.

7.3 Publications

The following is the list of publications during the course of MASc studies:

1. Sharifi, M., El-Sayegh, Z., and El-Gindy, M., "Sensitivity Analysis of Tire-Soil Interaction Using Finite Element Analysis and Smoothed-Particle Hydrodynamics Techniques," SAE Technical Paper 2019-01-0174, 2019
2. Gheshlaghi, F., El-Sayegh, Z., Sharifi, M., et al. Prediction and validation of terramechanics models for estimation of tyre rolling resistance coefficient. *International Journal of Vehicle Systems Modelling and Testing(IJVSMT), Vol.14, No,1. Pages 71-82 (2020)*
3. El-Sayegh, Z., Sharifi, M., Gheshlaghi, F. *et al*. Development of an HLFS agricultural tire model using FEA technique. *SN Appl. Sci.* **1,** 1454 (2019). https://doi.org/10.1007/s42452-019-1524-y
4. El-Sayegh, Z., Gheshlaghi F., Sharifi M.,El-Gindy, M. "Prediction and Validation of an Agricultural Tire-Soil Interaction Using Advanced Modelling Techniques". Tire Science and Technology, TST-19-212, 2019.

References

[1] F. Gheshlaghi and A. Mardani, "Prediction of Soil Vertical Stress Under the Off-road Tire using Smoothed-Particle Hydrodynamics," *Journal of Terramechanics,* pp. 1-8, 2020.

[2] S. Chae, "Nonlinear Finite Element Modeling and Analysis of a Truck Tire," The Pennsylvania State University, 2006.

[3] Encyclopaedia Britannica, "Britannica," Encyclopaedia Britannica, inc, 22 April 2016. [Online]. Available: https://www.britannica.com/technology/tire. [Accessed 10 04 2020].

[4] A. B. D. W. K. M/ Captain, "Analytical Tire Models for Dynamic Vehicle SImulation," *Vehicle System Dynamics,* vol. 8, no. 1, pp. 1-32, 1979.

[5] M. Loo, "A Model Analysis of Tire Behaviour Under Vertical Loading and Straight-Line Free Rolling," *Tire Sciece and Technology,* vol. 13, no. 2, pp. 67-90, 1985.

[6] R. V. Dukkipati, J. Pang, M. S. Qatu, Z. Shuguang and G. Sheng, Road Vehicle Dynamics, Warrendale: SAE International, 2008.

[7] M. Takayama and K. Yamagishi, "Simulation Model of Tire Vibration," *Tire Science and Technology,* vol. 1, no. 1, pp. 38-49, 1984.

[8] k. Guo, "Tire Roller Contact Model for Simulation of Vehicle Vibration Input," *SAE Technical Paper,* p. 9, 1993.

[9] D. C. Davis, "A Radial-Spring Terrain-Enveloping Tire Model," *Vehicle System Dynamics,* vol. 4, no. 1, pp. 55-69, 1975.

[10] A. Dhir and S. Sankar, "Analytical Wheel Models for Ride Dynamic Simulation of Off-road Tracked Vehicles," *Vehicle System Dynamics,* vol. 27, no. 1, pp. 37-63, 1997.

[11] S.-J. Kim and A. R. Savkoor, "The Contact Problem of In-Plane Rolling of Tires on a Flat Road," *Vehicle Systems Dynamics,* vol. 27, no. 1, pp. 189-206, 1997.

[12] P. W. Zegelaar and H. B. Pacejka, "Dynamic Tyre Responses to Brake Torque Variations," *Vehicl System Dynamics,* vol. 27, no. Sup001, pp. 65-79, 1997.

[13] J. Sui and J. Hirshey, "Evaluation on Analytical Tire Models for Vehicle Vertical Vibration Simulations Using Virtual Tire Testing Method," *SAE Technical Paper,* p. 8, 1999.

[14] S.-W. Kim, I. Cho, J.-H. Lee, J. Park, D.-H. Yi and D. D. Cho, "A New Method for Accurately Estimating the Weight of Movhing Vehicles Using Piezoelectric Sensors and Adaptive-footprint Tire Model," *Vehicle Systems Dynamics,* vol. 39, no. 2, pp. 135-148, 2003.

[15] S. Chae, "Nonlinear Finite Element Modeling and Analysis of a Truck Tire," The Pennsylvannia State University, Pennsilvania, 2006.

[16] S. Kim, P. E. Nikravesh and G. Gim, "A two-dimensional tire model on uneven roads for vehicle dynamic simulation," *Vechicle System Dynamics,* pp. 913-930, 14 August 2008.

[17] J. Svendenius and M. Gafvert, "A semi-emperical dynamic tire model for combined-slip forces," *Vehicle System Dynamics,* vol. 44, no. 2, pp. 189-208, 2007.

[18] J. L. Slade, "Electronic Thesis and Dissertations for Graduate School," 24 July 2009. [Online]. Available: https://etda.libraries.psu.edu/catalog/10075. [Accessed 15 April 2020].

[19] F. Wakui and Y. Terumichi, "Numerical Simulation of Tire Behavour on Soft Ground," *Journal of System Design and Dynamics,* vol. 5, no. 3, pp. 486-489, 2011.

[20] J. Madsen, A. Seidl, D. Negrut, P. Ayers, G. Bozdech, J. Freeman, J. O'Kins and A. Reid, "A Physics-Based Vehicle/Terrain Interaction Model for Soft Soil Off-Road Vehicle Simulations," *SAE Internationl,* 2012.

[21] C. F. Zorowski, "Mathematical Prediction of Dynamic Tire Behaviour," *Tire Science and Technology,* pp. 99-117, February 1973.

[22] R. A. Ridha, "Analysis for Tire Mold Design," *Tire Science and Technology,* pp. 195-210, August 1974.

[23] R. N. Yong, E. A. Fattah and P. Boonsinsuk, "Analysis and Prediction of Tyre-Soil Interaction and Performance using Finite Elements," *Journal of Terramechanics,* vol. 15, no. 1, pp. 43-63, 1978.

[24] J. T. Tielking, "A Finite Element Tire Model," *Tire Science and Technology,* vol. 11, no. 1, pp. 50-63, 1983.

[25] Y. K. Hu and P. F. J. Abeels, "Agricultural Tire Deformation in the 2D Case by Finite Element Methods," *Journal of Terramechanics,* vol. 31, no. 6, pp. 353-370, 1994.

[26] Z. Shida, M. Koishi, T. Kogure and K. Kabe, "A Rolling Resistance Simulation of Tires using Static Finite Element Analysis," *Tire Science and Technology,* vol. 27, no. 2, pp. 84-105, 1999.

[27] S. Shoop, K. Kestler and R. Haehnel, "Finite Element Modeling of Tires on Snow," *Tire Science and Technology,* vol. 34, no. 1, pp. 2-37, 2006 .

[28] N. Korunovic, M. Stojkovic and M. Trajanovic, "FEA of Tyres Subjected to Static Loading," *Journal of the Serbian Society for Computational Mechanics,* vol. 1, no. 1, pp. 87-98, 2007.

[29] K. Kabe and M. Koishi, "Tire Cornering Simulation Using Finite Element Analysis," *Computational Mechanics Lab, Research and Development Center,* 02 May 2000.

[30] Y. Zhang, T. Palmer and A. Farahani, "A Finite Element Tire Model and Vibration Analysis: A New Approach," *Tire Science and Technology,* vol. 26, no. 3, pp. 149-172, 1998.

[31] J. Allen, M. El-Gindy and K. Koudela, "Development of a Rigid Ring Quarter-Vehicle Model with an Advanced Road Profile Algorithm for Durability and Ride Comfort Predictions," in *Proceedings of ASME 2009 International Design Engineering Techinical Concerences*, Brooklyn, 2008.

[32] "Development of Truck Tire-Soil Interaction Model using FEA and SPH," *SAE International,* 2009.

[33] A. Mohsenimanesh, S. M. Ward, P. O. Owende and A. Javadi, "Modelling of Pneumatic Tractor Tyre Interaction with multi-layered soil," *ELSEVIER,* pp. 191-198, 2009.

[34] H. Ragheb, M. El-Gindy and H. Kishawy, "Development of a Combat Vehicle FEA Tire Model for Off-Road Applications," *SAE International,* 09 April 2013.

[35] A. C. Reid, "Development and Optimization of a Wide Base FEA Truck Tire Model for Prediction of Tire-Road Interactions," University of Ontario Institue of Technology, Oshawa, 2015.

[36] M. Marjani, "Development of FEA Wide-Base Truck Tire and Soil Interaction Models," University of Ontario Institute of Technology, Oshawa, 2016.

[37] A. W. Marr and J. T. Christian, "Finite Element Analysis of Elasto-plastic soils," National Aeronatics and Space Administration, Houston, 1972.

[38] L. Chi and R. L. Kushwaha, "A Non-Linear 3-D FInite Element Analysis of Soil Failure with Tillage Tools," *Journal of Terramechanics,* vol. 27, no. 4, pp. 343-366, 1990.

[39] T. K. David and R. R. Krishnamoorthy, "Finite Element Modelling of Soil-Structure Interaction," *Jurnal Teknology,* vol. 76, no. 8, 2015.

[40] N. Ungureanu, V. Vladut and S. St Biris, "FEM Modelling of Soil Behaviour under Compressive Loads," in *International Conference on Applied Sciences*, 2017.

[41] Z. El-Sayegh, M. El-Gindy, I. Johansson and F. Oijer, "Truck Tyre-Terrain Interaction Modelling and Testing: Literature Survey," *International Journal of Vehicle Systems Modelling and Testing,* vol. 12, no. 3-4, pp. 163-216, 2017.

[42] M. B. Liu and G. R. Liu, "Smoothed Particle Hydrodynamics (SPH): an overview and recent developments," *Archives of Computational Methods in Engineering,* vol. 17, no. 1, pp. 25-76, 2010.

[43] Z. El-Sayegh and M. El-Gindy, "Cornering characteristics of a truck tire on wet surface using fiite element analysis and smoothed-particle hydrodynamics," *International Journal of Dynamics and Control,* pp. 1-10, 2018.

[44] J. Pelfrene, "Study of the SPH method for simulation of regular breaking waves," Universiteit Gent, Gent, 2011.

[45] J. J. Monaghan, "Smoothed Particle Hydrodynamics," *Annual Review of Astronomy and Astrophysics,* vol. 30, no. 1, pp. 543-574, 1992.

[46] M. Nejad-Asghar, A. R. Khesali and J. Soltani, "Artificial Viscosity in Simulation of Shock Waves by Smoothed Particle Hydrodynamics," *Astrophysics and Space Science* , vol. 313, no. 4, pp. 425-430, 2008.

[47] Z. El-Sayegh, M. El-Gindy, I. Johansson and F. Oijer, "Off-Road Soft Terrain Modeling using Smoothed Particle Hydrodynamics Technique.," in *ASME 2018 International Design Engineering Technical Conferences and Computers Information in Engineering Conference*, 2018.

[48] P. Internation, Pam-Crash user Manual, ESI Group, 2014.

[49] H. H. Bui, K. Sako and R. Fukagawa, "Numerical Simulation of Soil-water interaction using smoothed particle hydrodynamics (SPH) method," *Journal of Terramechanics*, vol. 44, pp. 339-346, 2007.

[50] R. Lescoe, M. El-Gindy, K. Koudela, F. Oijer, M. Trivedi and I. Johansson, "Tire-Soil Modeling using Finite Element Analysis and Smooth Particle Hydrodynamics Techniques," in *ASME2010 International Design Engineering Technical Conferences & Computers and Information in Engineering Conference*, Montreal, 2010.

[51] T. Blanc and M. Pastor, "A Stabilized Smoothed Particle Hydrodynamics, Taylor-Galerkin Algorithm for Soil Dynamics Problems," *International Journal for Numerical and Analytical Methods in Geomechanics*, 2011.

[52] Y. Huang, W. Zhang, W. Mao and C. Jin, "Flow analysis of liquified soils based on smoothed particle hydrodynamics," Springer Science+ Business edia, 2011.

[53] R. Dhillon, R. Ali, M. El-Gindy, D. Philipps, F. Oijer and I. Johansson, "Development of Truck Tire-Soil Interaction Model using FEA and SPH," SAE International, 2013.

[54] R. Dhillon, M. El-Gindy, R. Ali, D. Philipps, F. Oijer and I. Johansson, "Sensitivity Analysis of Smoothed Particle Hydrodynamics in PAM-Crash for Modeling of Soft Soils".

[55] J. Grabe and B. Stefanova, "Numerical Modeling of Saturated Soils, Based on Smoothed Particle Hydrodynamics (SPH)," *Geotechnik*, vol. 37, no. 3, pp. 191-197, 2014.

[56] J. Grabe and B. Stefanova, "Numerical Modeling of Saturated Soils based on Smoothed Particle Hydrodynamics (SPH)," *Geotechnik*, vol. 38, no. 3, pp. 218-229, 2015.

[57] Z. Mao and G. R. Liu, "A Smoothed Particle Hydrodynamics Model for Electrostatic Transport of Charged Lunar Dust on the Moon Surface," *Springer Computational Particle Mechanics*, pp. 539-551, 2018.

[58] R. N. Yong and E. A. Fattah, "Analysis and Prediction of Tyre-Soil Interaction and Performance using Finite Elements," *Journal of Terramechanics*, vol. 15, no. 1, pp. 43-63, 1978.

[59] T. Hiroma, S. Wanjii, T. Kataoka and Y. Ota, "Stress Analysis using FEM on Stress Distribution under a Wheel Considering Friction with Adhesion Between a Wheel and Soil," *Journal of Terramechanics*, vol. 34, no. 4, pp. 225-233, 1997.

[60] C. H. Liu, J. Y. Wong and H. A. Mang, "Large Strain Finite Element Analysis of Sand: Model, Algorithm and Application to numerical simulation of Tire-Sand Interaction," Elsevier, Ottawa, 2000.

[61] Shoop, "Finite Element Modeling of Tire-Terrain Interaction," US Army Corps of Engineers, Arlington, 2001.

[62] F. Han and Z. G. Haosu Zhang, "FEA of Tire-Soil Model for Off-road vehicle," School of Mechanical Engineering Tongji University, Shanghai, 2010.

[63] K. Xia, "Finite Element Modeling of Tire/Terrain Interaction: Application of Predicting Soil Compaction and Tire Mobility," *Elsevier,* pp. 113-123, 2011.

[64] N. Nankali, M. Namjoo and M. R. Maleki, "Stress Analysis of Tractor Tire Interacting with Soil using 2D Finite Element Method," *International Journal of Advanced Design and Manufacturing Technology,* vol. 5, no. 3, pp. 107-111, 2012.

[65] H. Li and C. Schindler, "Analysis of Soil Compaction and Tire Mobility with Finite Element Method," *Journal of Multi-Body Dynamics,* pp. 275-291, 2013.

[66] K. L. Lardner, "Prediction of the Off-Road Rigid-Ring Model Parameters for Truck Tire and Soft Soil Interaction," University of Ontario Institute of Technology, Oshawa, 2017.

[67] Z. El-Sayegh and M. El-Gindy, "Modellng and Prediction of Tyre-snow Interaction using Finite Element Analysis-Smoothed Particle Hydrodynamics Technique," *Journal of Automobile Engineering,* pp. 1-10, 2018.

[68] H. Ragheb, M. El-Gindy and H. Kishawy, "Development of a Combat Vehicle FEA Tire Model for off-road applications," SAE Technical Paper, 2013.

[69] H.-H. Dai, "Model equations for nonlinear dispersive waves in a compressible mooney-rivlin rod," *Acta Mechanica,* vol. 127, no. 1-4, pp. 193-207, 1998.

[70] "Barez Tires," 05 March 2019. [Online]. Available: http://www.barez.com/trs-tire/24849-8.25-16.html.. [Accessed 5 March 2019].

[71] F. Gheshlaghi, A. Mardani, A. Mohebi and H. Taghavifar, "Developing an Analytical Model for Prediction of Tire Rolling Resistsance on Moist Soils," *Int. Journal of Heavy Vehicle Systems,* pp. 1-18, 2020.

[72] Y. Y. Wong, Theory of Ground Vehicles, John Wiley & Sons, 2008.

[73] F. Gheshlaghi, A. Mardani and A. Mohebi, "Investigating the effects of off-road vehicles on soil compaction using FEA-SPH simulation," *Int. Journal of Heavy Vehicle Systems,* pp. 1-10, 2020.

[74] F. Gheshlaghi and A. Mardani, "Prediction of Soil Vertical Stress Under the Off-road Tire using Smoothed-Particle Hydrodynamics," *Journal of Terramechanics,* pp. 1-8, 2020.

[75] K. Lardner, "Prediction of the Off-Road Rigid Ring Model Parameters for Truck Tire and Soft Soil Interactions," University of Ontario Institute of Technology, Oshawa, 2017.

[76] J. Monaghan, "Simulating free surface flows with SPH," *Journal of Computational Physics,* pp. 399-406, 1994.